To the Graduate Council:

I am submitting herewith a dissertation written by Ho-Pen Chang entitled "Investigation of the Dynamic Response of Aircraft to Microburst (JAWS) Wind Shear." I have examined the final copy of this dissertation for form and content and recommend that it be accepted in partial fulfillment of the requirements for the degree of Doctor of Philosophy, with a major in Aerospace Engineering.

Walter Frost

Dr. Walter Frost, Major Professor

We have read this dissertation and recommend its acceptance:

Frank G. Collins

John E. Caruthers

Kenneth R. Kimble

M. Milligan

Accepted for the Council:

[signature]

Vice Provost
and Dean of The Graduate School

INVESTIGATION OF THE DYNAMIC RESPONSE OF AIRCRAFT TO MICROBURST (JAWS) WIND SHEAR

A Dissertation

Presented for the

Doctor of Philosophy

Degree

The University of Tennessee, Knoxville

Ho-Pen Chang

June 1985

ACKNOWLEDGMENTS

The work reported herein was partially supported by the National Center for Atmospheric Research, Boulder, Colorado, under Subcontract S3011. The author wishes to express his appreciation to all the members of The University of Tennessee Space Institute who have assisted during completing this study.

Special thanks should go to Dr. Walter Frost, the project supervisor, for his helpful guidance in the course of this dissertation research. The author would like to thank his committee, Dr. Kenneth Kimble, Dr. Frank Collins, Dr. John Caruthers, and Dr. Mancil W. Milligan. With thier consultation, criticism, and encouragement the author was able to achieve results otherwise impossible.

Furthermore, the author wishes to extend appreciation to his family, his wife Shi-Min Sau, his father Rung-Guay Chang, and his mother Jung-Man Chang, for their constant encouragement.

Finally, the author would like to thank Mrs. Barbara Smith for typing this dissertation and Mr. Robert "Mutt" Suttles for preparing the illustrations presented in this study.

ABSTRACT

A derivation of the governing equations of aircraft motion in variable wind field results in additional wind shear terms appearing in the force equations. Computer simulations of B727 type aircraft flying (landing and taking off) through the microburst (JAWS) wind shear data have been carried out and are in good agreement with those of the NASA/Ames B727 piloted simulator.

The critical penetration heights through the center of the microburst are determined by computing the aircraft trajectory deviations from the intended flight path at the ILS Category II decision height window. It is found that the higher the magnitude of the wind gradient terms, the more influence they have on the aircraft performance, especially on sideslip angle, angle of attack, and rolling moment. However, the maximum magnitude of the wind gradients in JAWS August 5, 1982, microburst data is about 0.03 s^{-1}. The wind shear effects on three generic types of aircraft, a three-engine passenger airliner (PA), a twin-engine STOL (STOL), and an executive jet (EJ), are also investigated in this study. In the simulation of the aircraft flying through a microburst center along the intended path $\overline{AB}$ at a height of 820 feet, the maximum trajectory deviations from the glide slope are 350 feet, 200 feet, and 100 feet for the PA, EJ, and STOL type airplanes, respectively. Large jet aircraft experience greater difficulty in flight through a microburst wind shear field than smaller aircraft.

It is recommended that a turbulence model to supplement the JAWS wind field be developed, and the flight simulator computer programs be

updated to incorporate the additional wind shear terms into the equations of vehicle motion. Finally, the influence of time variations of the JAWS wind shear on the aircraft performance is investigated.

TABLE OF CONTENTS

LIST OF TABLES

LIST OF FIGURES

FIGURE PAGE

FIGURE PAGE

FIGURE PAGE

LIST OF SYMBOLS

$\overline{AB},\overline{CD},\overline{YZ},\overline{GH},\overline{IJ},\overline{KL}$	Intended flight paths in JAWS August 5, 1982, microburst
b	Wing span of vehicle
C_D,C_Y,C_L	Aerodynamic force coefficients corresponding to D, C, and L, respectively
C_ℓ,C_m,C_n	Aerodynamic moment coefficients corresponding to ℓ, m, and n, respectively
$\bar{c}$	Mean aerodynamic chord
D,C,L	Aerodynamic forces in stability axes
FAA	Federal Aviation Administration
F_B	Vehicle fixed axes
F_E	Earth fixed axes
F_S	Stability axes
F_T	Thrust force of vehicle
$\dot{F}_T$	Rate change of thrust force
F_W	Wind axes
g	Gravitational acceleration
h	Height of the ILS CAT II decision height window
ICAO	International Civil Aviation Organization
ILS	Instrumented Landing System
I_X,I_Y,I_Z	Moment of inertia of vehicle relative to the body axes
I_{ZX}	Product of inertia of vehicle relative to OXZ plane
JAWS	Joint Airport Weather Studies
L,M,N	Total rolling, pitching, and yawing moments about the body axes OX, OY, and OZ, respectively

W_{XE}, W_{YE}, W_{ZE}	Wind speed components in the earth frame of reference
$\dot{W}_{XE}, \dot{W}_{YE}, \dot{W}_{ZE}$	Total derivatives of the wind vector components in inertial reference frame
X,Y,Z	Total forces in body axis OX, OY, and OZ, respectively
$\dot{X}_E, \dot{Y}_E, \dot{Z}_E$	Inertial velocity components of vehicle
$\dot{X}_N$	Trim ground speed of vehicle
x,y,z	Coordinate system of the measurement of JAWS microburst; origin is located at CP-2 (Figure 3.2, page 24)
x_0, y_0, z_0	Coordinate system defined in Figures 5.1 and 5.4, pages 56 and 61

Greek Symbols

α	Angle of attack
$\dot{\alpha}$	Time derivative of angle of attack
β	Sideslip angle
$\dot{\beta}$	Time derivative of sideslip angle
$\Delta t_1, \Delta t_2, \ldots.$	Time intervals of the serial measurement of a time-dependent microburst
$\delta_E, \delta_R, \delta_A$	Elevator, rudder, and aileron deflections
$\delta_{EN}, \delta_{RN}, \delta_{AN}, \delta_{TN}$	Trim values (zeros in trim straight flight) for elevator, rudder, aileron, and thrust setting, respectively
δ_T	Rate of change of thrust setting
ρ	Air density
θ	Angle of the runway relative to positive x direction
ϕ, θ, ψ	Euler angles for body axes
$\dot{\phi}, \dot{\theta}, \dot{\psi}$	Total derivative of roll, pitch, and yaw angles

$\vec{\omega}$	Inertial rotation velocity of vehicle
$\vec{\omega}_W$	Inertial rotation velocity of atmosphere
∂	Partial derivative
$\frac{\partial \delta_E}{\partial \dot{Z}}, \frac{\partial \delta_E}{\partial \theta}, \frac{\partial \delta_R}{\partial \dot{Y}}, \frac{\partial \delta_R}{\partial \psi}, \frac{\partial \delta_A}{\partial \dot{Y}}, \frac{\partial \delta_A}{\partial \phi}, \frac{\partial \delta_T}{\partial \dot{X}}$	Gain factors of control laws

CHAPTER I

INTRODUCTION

Investigations of at least 30 commercial airplane accidents and incidents (National Research Council, 1983; Aviation Week and Space Technology, 1983 and 1984) during 1964 to 1984 have clearly proven that wind shear, resulting from a sudden change in either the speed or direction of the wind, can produce dynamic effects on aircraft and cause aircraft to deviate significantly from the pilot's intended flight path. Both the International Civil Aviation Organization (ICAO) and the Federal Aviation Administration (FAA) also recognize wind shear as a potential hazard to aircraft landing and takeoff. Although the wind shear can result from a number of basically different meteorological conditions, it has been recognized that small short-lived downdrafts, called microbursts, are serious hazards to aircraft during landings and takeoffs. Analyses of the dynamic performance of airplanes through three-dimensional low-altitude microbursts are carried out in the present study.

Microbursts are small downdrafts, less than 2.5 miles (4 km) in outflow size, with the peak winds lasting only 2 to 5 minutes as shown in Figure 1.1. The JAWS* microburst occurrence frequency as a function of the maximum difference of the wind speed near the surface is shown

---

*JAWS (Joint Airport Weather Studies) was conducted near Stapleton International Airport, Denver, Colorado, between May 15 and August 13, 1982. The program was managed by NCAR (National Center for Atmospheric Research) in Boulder, Colorado, and by the University of Chicago.

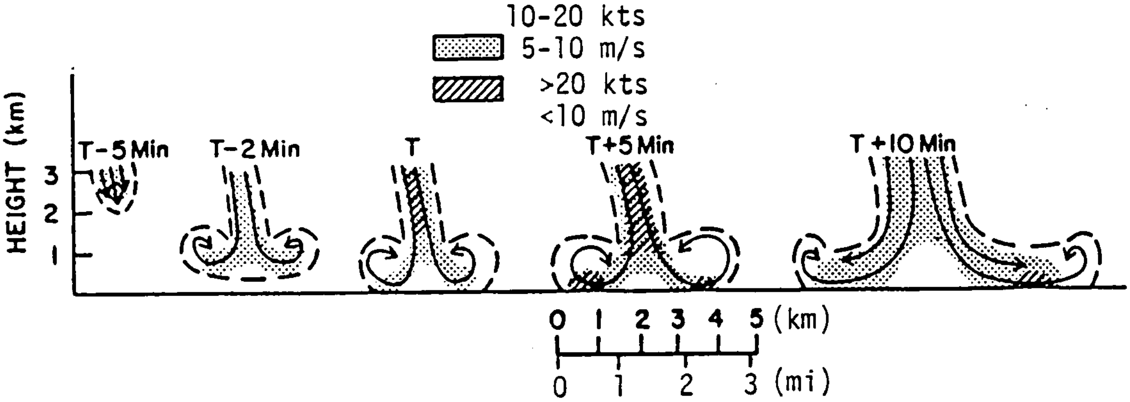

Figure 1.1. Vertical cross section of the evolution of the microburst wind field, based on a summary of examining 50 microbursts with Doppler radar. T is the time of initial divergence reaching the surface. Notice that it takes about 5 minutes after T for the microburst to reach maximum intensity. In addition, the divergence is observed above the surface several minutes before impact with the surface (Frost et al., 1985).

in Figure 1.2. In this illustration, the maxium headwind-to-tailwind velocity difference is shown ranging from 20 to 100 knots (10 to 50 m/s). The microburst velocity differential that brought down Pan Am Flight 759 on July 9, 1982, was only 45 knots, or approximately the median value of radar-observed JAWS microbursts (McCarthy, 1983). The JAWS data is introduced in more detail in Chapter III.

A dangerous sequence of events (headwind then downdraft then tailwind) occurs when an aircraft penetrates a microburst at low levels as shown in Figure 1.3. This figure illustrates that as the aircraft approaches a microburst cell, it encounters a steadily increasing headwind, which increases lift and forces the aircraft to climb above its glide slope. However, increase in drag results in reduced ground speed, which for most aircraft is not monitored; in fact, most pilots are

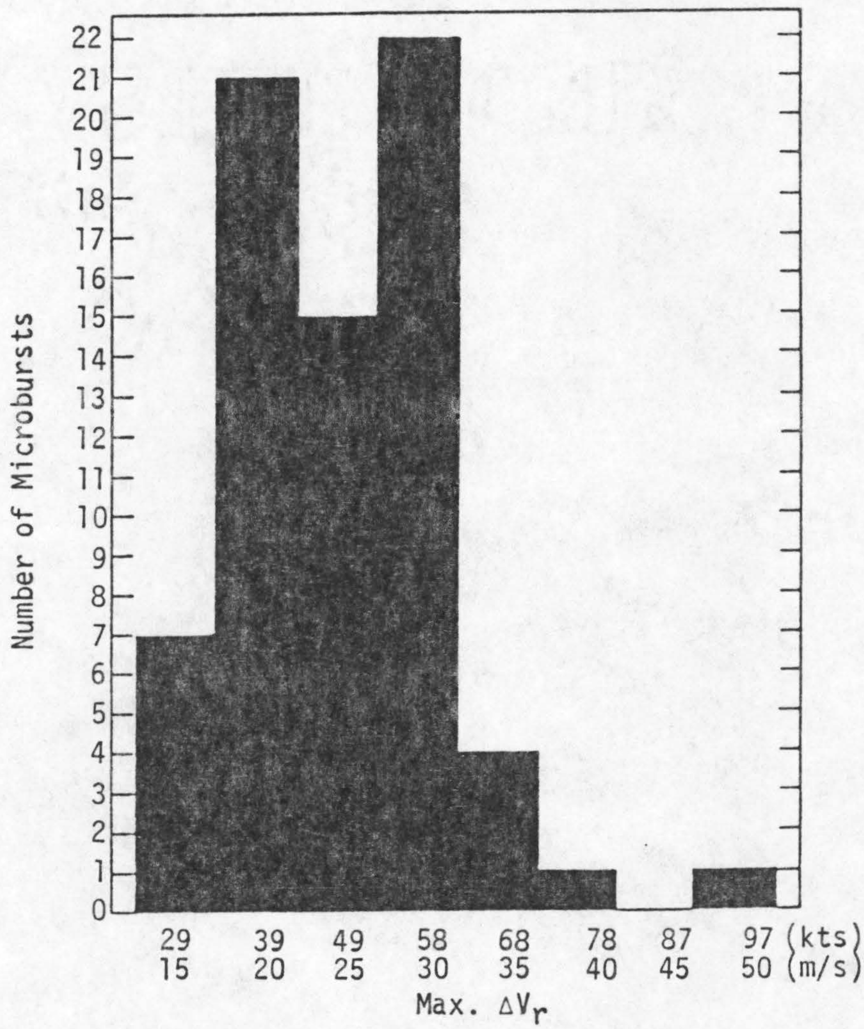

Figure 1.2. Number of JAWS microbursts as a function of maximum differential velocity measured near the surface by Doppler radar. The figure shows the approximate maximum headwind to tailwind shear that an aircraft would encounter when penetrating the microburst (Frost et al., 1985).

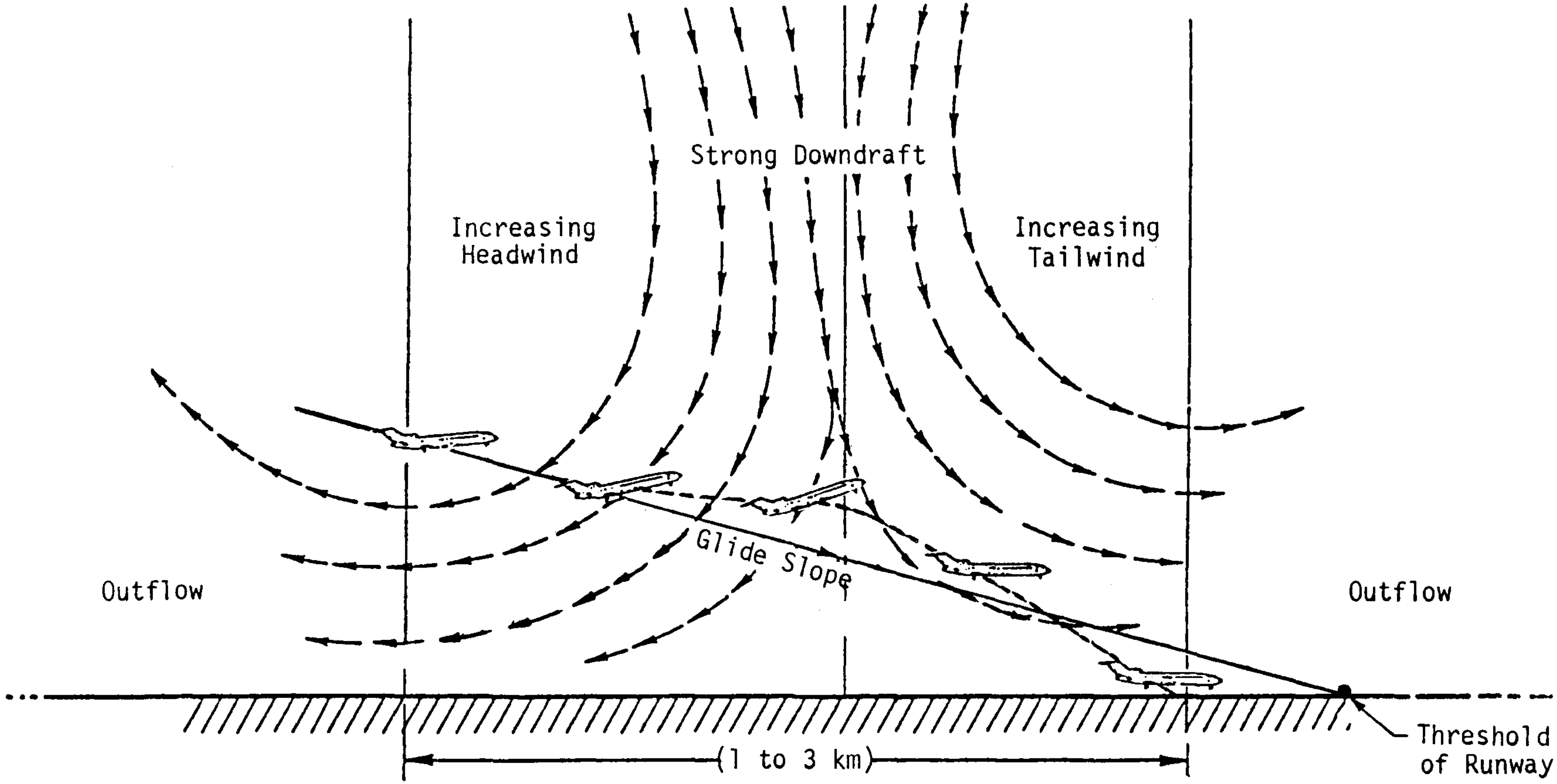

Figure 1.3. Schematic illustration of an aircraft penetration of a microburst. The airplane first encounters a headwind and experiences increasing performance. This is followed in short succession by a downdraft and a strong tailwind, both causing serious performance loss, possibly resulting in a crash.

unaware when ground speed, or inertial velocity, is dropping off. At the center of the microburst, the airspeed of the aircraft diminishes and the aircraft encounters a strong downdraft. The downdraft velocities are much smaller near the ground than those at higher altitudes because the descending air must turn and flow out horizontally because of the ground proximity. The downdraft causes a decrease in angle of attack and results in a simultaneous loss of aircraft lift. In other words, the aircraft being engulfed in the sinking air mass is carried downward. The combination of reduced lift and downdraft causes a rapid loss in altitude. If the aircraft does not impact the ground and manages to penetrate the downdraft zone, it encounters a severely increasing tailwind. The increasing tailwind causes a significant loss of airspeed with a corresponding deterioration of aerodynamic lift. Unless the pilot takes corrective action immediately, the aircraft will impact the ground. Likewise, the same sequence of events can occur during takeoff, resulting in a performance loss that may be severe enough to cause ground impact.

Although numerous studies relating to the influence of individual gusts or random turbulence on flight performance of aircraft (for example, see Houbolt et al., 1964; Peloubet and Haller, 1966; Wang and Frost, 1980; AGARD Conference Proceedings, 1973; Reeves et al., 1976) have been conducted, these are generally associated with the high-frequency atmospheric turbulence fluctuations. Thus, only aircraft performance relative to the changes in wind on time and spatial scales which are small in comparison with the scales associated with severe wind shear (Frost et al., 1979; Goff, 1980) have been studied. In this study, the dynamic response of an aircraft to the severe wind shear microburst is investigated.

In Chapter II, the general equations of unsteady motion of an aircraft flying through a variable wind field instead of constant or zero wind as conventionally done in textbooks are derived. Wind shear terms, derivatives of wind speed components, associated with a three-dimensional unsteady wind field are defined. The effects of the wind shear terms on the aerodynamic coefficients are also discussed in Chapter II. Sources of wind shear data are interpreted in Chapter III. Prior to JAWS, there was not sufficient meteorological data available to construct three-component, three-dimensional spatial, and time-dependent models of wind shear for aircraft simulation studies, design, and operational procedure development. The multi-Doppler radar measurements from JAWS have provided the three-dimensional wind fields used in this study.

In Chapter IV the numerical algorithm to calculate the aircraft's dynamic performance with three-dimensional wind shear data is described. In turn, the three-dimensional interpolating technique to obtain the wind components and wind shear terms at the position of the aircraft from the grid stored data set is presented. The trim conditions for three types of aircraft are determined in the same chapter. Also, the automatic control laws, which control the elevator/rudder/aileron deflections and thrust force to correct the aircraft deviations from the intended flight path, are described. Finally, the numerical method in this study is evaluated by comparing the results of the numerical algorithm with those of manned simulator flights.

General results of wind shear effects, which are composed of the influences of wind speed components and its derivatives (wind gradient terms), on aircraft performance are discussed in the first section of Chapter V. The effects of the wind shear on aircraft dynamics are then analyzed quantitatively and statistically by reference to an ILS (Instrumented Landing System) Category II decision height window, which is defined in Chapter V. The influence of the wind shear terms on aircraft dynamics are also analyzed by calculating the standard deviations (SD) of attitudes of the aircraft and the SD's of the predominant wind shear terms within a microburst cell defined in Chapter V, Section 2. Meanwhile, the wind shear effects on different generic types of aircraft--a three-engine passenger airliner (PA), a twin-engine STOL (STOL), and an executive jet (EJ)--are shown in Chapter V. A time-dependent wind shear model is also presented in this same chapter. Finally, conclusions from the study are presented in Chapter VI.

CHAPTER II

INCORPORATING WIND SHEAR TERMS INTO THE GOVERNING EQUATIONS OF AIRCRAFT MOTION

1. GOVERNING EQUATIONS OF AIRCRAFT MOTION

Generally speaking, both the development of the governing equations and the analyses of aircraft motion assume that aircraft fly in constant or zero wind fields. Almost all textbooks (Etkin, 1972; Perkins and Hage, 1963; Houghton and Brock, 1972; Babister, 1980; Roskam, 1973) on aircraft flight dynamics place little, if any, emphasis on variable winds. In studying aircraft dynamic responses to the scales of severe wind shear associated with thunderstorms, microbursts, or gust fronts, the aircraft equations of motion should incorporate wind shear terms (Frost and Bowles, 1984). In the derivation of the equations used in this study, the earth is assumed to be a stationary plane in inertial space. This assumption is well justified for takeoff and landing problems, which are the main considerations in wind-shear-caused accidents.

Figure 2.1 shows the earth-fixed axes, vehicle-fixed axes, air-trajectory-fixed axes, and stability axes used as reference frames (Etkin, 1972; Roskam, 1973) in most aircraft dynamics analyses. Based on the assumption that the earth is a stationary plane in inertial space, earth-fixed axes can be considered as the inertial frame of reference, designated as F_E. The vehicle-fixed axes, called body-axis reference frame, F_B, has the origin at the mass center of gravity.

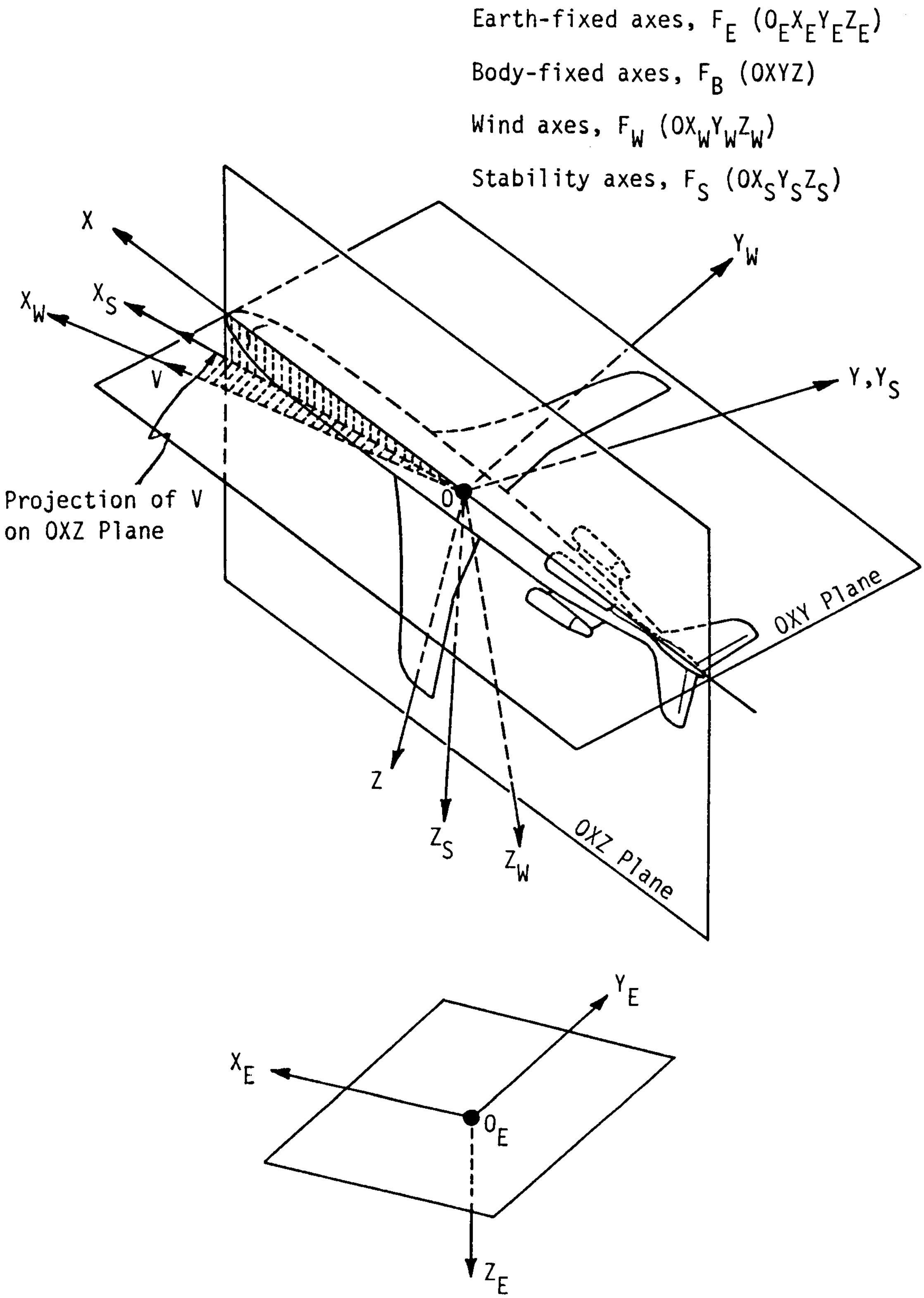

Figure 2.1. Coordinate systems for flight over a flat earth.

The plane of symmetry of the vehicle is generally taken as OXZ where OZ is directed downward. The air-trajectory-fixed axes, called the wind-axis reference frame, F_W (by Etkin, 1972), has the origin fixed to the vehicle, usually at the mass center, and the X_W-axis is directed along the relative velocity vector of the vehicle to the atmosphere, $\vec{V}$. The stability axes system, F_S, has the origin at the mass center of gravity, OX_S is chosen to lie on the projection of V in the plane of symmetry, with OZ_S also in the plane of symmetry.

In terms of the inertial velocity of the vehicle, $\vec{V}_E$, and the inertial velocity of the atmosphere, $\vec{W}$, the velocity of the vehicle relative to the atmosphere, $\vec{V}$, is

$$\vec{V} = \vec{V}_E - \vec{W} \quad \text{or} \quad \vec{V}_E = \vec{V} + \vec{W} \tag{2.1}$$

Also, the components of angular velocity of the body-axis frame of reference, F_B, relative to F_E are designated as p, q, and r.

<u>Force Equations in Body Axes, F_B</u>

By applying Newton's second law, the governing force equations for six-degrees-of-freedom motion in body axes, F_B, become

$$X - mg \sin\theta = m(\dot{u} + \dot{W}_X) + m[q(w + W_Z) - r(v + W_Y)]$$

$$Y + mg \cos\theta \sin\phi = m(\dot{v} + \dot{W}_Y) + m[r(u + W_X) - p(w + W_Z)] \tag{2.2}$$

$$Z + mg \cos\theta \cos\phi = m(\dot{w} + \dot{W}_Z) + m[p(v + W_Y) - q(u + W_X)]$$

where X, Y, and Z are total forces, which include aerodynamic forces and thrust, in the OX, OY, and OZ directions, respectively; m is the mass of the vehicle; g is the acceleration of gravity; and θ, ϕ, and ψ

are Euler angles for body axes. The Euler angles are defined as those angles which rotate the earth's fixed reference frame into coincidence with the relevant axis system (for example, F_B or F_W) (Etkin, 1972). W_X, W_Y, and W_Z are variable wind speed components along body axes OX, OY, and OZ, respectively. u, v, and w are the velocity components of the vehicle relative to atmosphere in body axes. Finally, $\dot{W}_X$, $\dot{W}_Y$, and $\dot{W}_Z$ are the total derivatives of wind vector components in body-axis reference frame.

Usually, the components of the wind velocity are given as W_{XE}, W_{YE}, and W_{ZE} in the earth frame of reference. W_X, W_Y, and W_Z in body axes can be calculated as follows:

$$\begin{Bmatrix} W_X \\ W_Y \\ W_Z \end{Bmatrix} = L_{BE} \begin{Bmatrix} W_{XE} \\ W_{YE} \\ W_{ZE} \end{Bmatrix} \tag{2.3}$$

where L_{BE} is the matrix to transform the vector components in the inertial reference frame $(O_E X_E Y_E Z_E)$ into the components in the body-axis reference frame (OXYZ) has the form in terms of the Euler angles for the body axes:

$$L_{BE} = \begin{bmatrix} \cos\theta \cos\psi & \cos\theta \sin\psi & -\sin\theta \\ \sin\phi \sin\theta \cos\psi - \cos\phi \sin\psi & \sin\phi \sin\theta \sin\psi + \cos\phi \cos\psi & \sin\phi \cos\theta \\ \cos\phi \sin\theta \cos\psi + \sin\phi \sin\psi & \cos\phi \sin\theta \sin\psi - \sin\psi \cos\psi & \cos\phi \cos\theta \end{bmatrix} \tag{2.4}$$

Now, the derivatives of the wind components in body axes are determined by taking time derivatives of Equation 2.3:

$$\begin{Bmatrix} \dot{W}_X \\ \dot{W}_Y \\ \dot{W}_Z \end{Bmatrix} = L_{BE} \begin{Bmatrix} \dot{W}_{XE} \\ \dot{W}_{YE} \\ \dot{W}_{ZE} \end{Bmatrix} + \dot{L}_{BE} \begin{Bmatrix} W_{XE} \\ W_{YE} \\ W_{ZE} \end{Bmatrix} \tag{2.5}$$

where $\dot{W}_{XE}$, $\dot{W}_{YE}$, and $\dot{W}_{ZE}$, the derivatives of the wind vector components in inertial reference frame, are

$$\begin{aligned} \dot{W}_{XE} &= \frac{\partial W_{XE}}{\partial t} + \frac{\partial W_{XE}}{\partial X_E} \dot{X}_E + \frac{\partial W_{XE}}{\partial Y_E} \dot{Y}_E + \frac{\partial W_{XE}}{\partial Z_E} \dot{Z}_E \\ \dot{W}_{YE} &= \frac{\partial W_{YE}}{\partial t} + \frac{\partial W_{YE}}{\partial X_E} \dot{X}_E + \frac{\partial W_{YE}}{\partial Y_E} \dot{Y}_E + \frac{\partial W_{YE}}{\partial Z_E} \dot{Z}_E \\ \dot{W}_{ZE} &= \frac{\partial W_{ZE}}{\partial t} + \frac{\partial W_{ZE}}{\partial X_E} \dot{X}_E + \frac{\partial W_{ZE}}{\partial Y_E} \dot{Y}_E + \frac{\partial W_{ZE}}{\partial Z_E} \dot{Z}_E \end{aligned} \tag{2.6}$$

Here, $\dot{X}_E$, $\dot{Y}_E$, and $\dot{Z}_E$ are the inertial velocity components of the vehicle, and the nine spatial derivative terms associated with three time derivative terms are called the wind gradient terms.

$\dot{L}_{BE}$, the time derivative of the transformation matrix, is derived as:

$$\dot{L}_{BE} = \begin{bmatrix} \ell_{11} & \ell_{12} & \ell_{13} \\ \ell_{21} & \ell_{22} & \ell_{23} \\ \ell_{31} & \ell_{32} & \ell_{33} \end{bmatrix} \tag{2.7}$$

where

$$\ell_{11} = -(\sin\theta \cos\psi)\dot{\theta} - (\cos\theta \sin\psi)\dot{\psi}$$

$$\ell_{12} = -(\sin\theta \sin\psi)\dot{\theta} + (\cos\theta \cos\psi)\dot{\psi}$$

$$\ell_{13} = -(\cos\theta)\dot{\theta}$$

$$\ell_{21} = (\cos\phi \sin\theta \cos\psi + \sin\phi \sin\psi)\dot{\phi} + (\sin\phi \cos\theta \cos\psi)\dot{\theta} - (\sin\phi \sin\theta \sin\psi + \cos\phi \cos\psi)\dot{\psi}$$

$$\ell_{22} = (\cos\phi \sin\theta \sin\psi - \sin\theta \cos\psi)\dot{\phi} + (\sin\phi \cos\theta \sin\psi)\dot{\theta} + (\sin\phi \sin\theta \cos\psi - \cos\phi \sin\psi)\dot{\psi}$$

$$\ell_{23} = (\cos\phi \cos\theta)\dot{\phi} - (\sin\phi \sin\theta)\dot{\theta}$$

$$\ell_{31} = (\cos\phi \sin\psi - \sin\phi \sin\theta \cos\psi)\dot{\phi} + (\cos\phi \cos\theta \cos\psi)\dot{\theta} + (\sin\phi \cos\psi - \cos\phi \sin\theta \sin\psi)\dot{\psi}$$

$$\ell_{32} = -(\sin\phi \sin\theta \sin\psi + \cos\phi \cos\psi)\dot{\phi} + (\cos\phi \cos\theta \sin\psi)\dot{\theta} + (\cos\phi \cos\theta \cos\psi + \sin\phi \sin\psi)\dot{\psi}$$

$$\ell_{33} = -(\sin\phi \cos\theta)\dot{\phi} - (\cos\phi \sin\theta)\dot{\theta}$$

Euler angles for the body axes, ϕ, θ, ψ, are computed from the following kinematic relationships, implicit ordinary differential equations.

$$\dot{\phi} = p + q \sin\phi \tan\theta + r \cos\phi \tan\theta$$

$$\dot{\theta} = q \cos\phi - r \sin\phi \qquad (2.8)$$

$$\dot{\psi} = (q \sin\phi + r \cos\phi) \sec\theta$$

Finally, the position of the aircraft relative to inertial space is computed by integrating the inertial velocity equations as follows:

$$\begin{pmatrix} \dot{X}_E \\ \dot{Y}_E \\ \dot{Z}_E \end{pmatrix} = L_{EB} \begin{pmatrix} u \\ v \\ w \end{pmatrix} + \begin{pmatrix} W_{XE} \\ W_{YE} \\ W_{ZE} \end{pmatrix} \qquad (2.9a)$$

$$\begin{Bmatrix} \dot{X}_E \\ \\ \dot{Y}_E \\ \\ \dot{Z}_E \end{Bmatrix} = \begin{Bmatrix} u \cos\theta \cos\psi + v(\sin\phi \sin\theta \cos\psi - \cos\phi \sin\psi) \\ \quad + w(\cos\phi \sin\theta \cos\psi + \sin\phi \sin\psi) + W_{XE} \\ u \cos\theta \sin\psi + v(\sin\phi \sin\theta \sin\psi + \cos\phi \cos\psi) \\ \quad + w(\cos\phi \sin\theta \sin\psi - \sin\phi \cos\psi) + W_{YE} \\ -u \sin\theta + v \sin\psi \cos\theta + w \cos\psi \cos\theta + W_{ZE} \end{Bmatrix} \tag{2.9b}$$

Moment Equations in Body Axes, F_B

The rate of angular rotation, p, q, and r, are generally computed in the body coordinate system, regardless of the coordinate system in which the force equations are expressed. The reason for this is that the moments and products of inertia are relatively constant in the body axis. Based on the assumption of a rigid aircraft with symmetry in the OXZ plane, the moment equations are:

$$\begin{aligned} L &= I_X\dot{p} - I_{ZX}(\dot{r} + pq) - (I_Y - I_Z)qr \\ M &= I_Y\dot{q} - I_{ZX}(r^2 - p^2) - (I_Z - I_X)rp \\ N &= I_Z\dot{r} - I_{ZX}(\dot{p} - qr) - (I_X - I_Y)pq \end{aligned} \tag{2.10}$$

where L, M, and N are rolling, pitching, and yawing moments (due to both thrust and aerodynamic forces) about the body axes OX, OY, and OZ, respectively. I_X, I_Y, and I_Z are the moment of inertia of the vehicle relative to the body axes. I_{ZX} is the product of inertia of the vehicle relative to the OXZ plane. Also, p, q, and r are the components of the inertial angular velocity of the vehicle.

As long as the forces (X, Y, and Z) and moments (L, M, and N) acting on the vehicle are known, the dynamic performance of an aircraft can be evaluated by solving the 12 simultaneous implicit differential equations, Equations 2.2, 2.8, 2.9, and 2.10.

2. INFLUENCE OF WIND SHEAR TERMS ON AERODYNAMIC FORCES AND MOMENTS

The aerodynamic forces (D, C, and L) and moments (ℓ, m, and n) are functions of dynamic pressure and aerodynamic coefficients. In general, the aerodynamic forces and moments are expressed in the stability axes by the relationships:

$$D = C_D \rho V^2 S/2; \quad C = C_Y \rho V^2 S/2; \quad L = C_L \rho V^2 S/2 \tag{2.11a}$$

and

$$\ell = C_\ell \rho V^2 Sb/2; \quad m = C_m \rho V^2 S\bar{c}/2; \quad n = C_n \rho V^2 Sb/2 \tag{2.11b}$$

where V is the magnitude of the velocity of the vehicle relative to atmosphere, ρ is air density, S is the wing area of the aircraft, b is the wing span of the aircraft, and $\bar{c}$ is the mean wing chord length of the aircraft. The assumption is made that the existing aircraft stability derivatives (see the Appendix) can be employed with the wind gradient terms to compute aerodynamic coefficients.

However, the aerodynamic coefficients (C_D, C_Y, C_L, C_ℓ, C_m, and C_n) are dependent on the Reynolds and Mach numbers (Re and M), angle of attack and sideslip angle (α and β), the time derivatives of angle of attack and sideslip angle ($\dot{\alpha}$ and $\dot{\beta}$), linear and angular relative velocities. When dealing with spatially and temporally varying winds, the influence of the wind shear terms (derived in Section 1) on the aerodynamic forces and moments, which act on the vehicle, are discussed in the following.

Consider first $\dot{\alpha}$ and $\dot{\beta}$. By definition, the angle of attack and sideslip angle are:

$$\alpha = \tan^{-1} \frac{w}{u} \tag{2.12a}$$

and

$$\beta = \sin^{-1} \frac{v}{V} \tag{2.12b}$$

Differentiating α and β with respect to time and carrying out the algebra gives:

$$\begin{aligned} \dot{\alpha} &= \frac{u\dot{w} - w\dot{u}}{u^2 + w^2} \\ \dot{\beta} &= \frac{\dot{v}(u^2 + w^2) - v(u\dot{u} + w\dot{w})}{V^2\sqrt{u^2 + w^2}} \end{aligned} \tag{2.13}$$

Thus, the wind gradient terms enter $\dot{\alpha}$ and $\dot{\beta}$ through $\dot{u}$, $\dot{v}$, and $\dot{w}$, which are given by (see Equation 2.2):

$$\begin{aligned} \dot{u} &= \frac{X}{m} - g \sin \theta - \dot{W}_X - [q(w + W_Z) - r(v + W_Y)] \\ \dot{v} &= \frac{Y}{m} + g \cos \theta \sin \phi - \dot{W}_Y - [r(u + W_X) - p(w + W_Z)] \\ \dot{w} &= \frac{Z}{m} + mg \cos \theta \cos \phi - \dot{W}_Z - [p(v + W_Y) - q(u + W_X)] \end{aligned} \tag{2.14}$$

Also, expressions for the aerodynamic coefficients generally contain a linear relationship in terms of the angular rotations p, q, and r. Equation 2.10 is normally used to solve the dynamic equation of motion for p, q, and r. The values obtained are thus inertial values. However, the stability derivatives multiplied by p, q, and r in the linear expansion of the aerodyanmic coefficients are based on values of angular rotation relative to the atmosphere, $\vec{\omega} - \vec{\omega}_W$. The vector $\vec{\omega}_W$ is the rotation of the wind field relative to the inertial frame of reference. Figure 2.2 illustrates the concept for a two-dimensional configuration. The tensor gradient of a vector field can be split into a symmetric and an antisymmetric part (Karamcheti, 1966). The symmetric part measures the instantaneous rate of strain while the antisymmetric part measures the instantaneous rate of rotation at the point considered. Physically, this rotation can be considered as if the air mass is a rigid solid and is brought about by fluid stresses whose curl does not vanish. Figure 2.3 presents a wind vector field in a severe microburst of the JAWS network. The rotation of the wind field is obviously a phenomenon observed and documented in the real world.

Thus, $\vec{\omega}_W$ can be expressed as:

$$\vec{\omega}_W = \frac{1}{2}\vec{\nabla} \times \vec{W} \qquad (2.15)$$

In inertial coordinates:

$$\vec{\omega}_W = \frac{1}{2}\left(\frac{\partial W_Z}{\partial Y} - \frac{\partial W_Y}{\partial Z}\right)_E \vec{i} + \frac{1}{2}\left(\frac{\partial W_X}{\partial Z} - \frac{\partial W_Z}{\partial X}\right)_E \vec{j} + \frac{1}{2}\left(\frac{\partial W_Y}{\partial X} - \frac{\partial W_X}{\partial Y}\right)_E \vec{k} \qquad (2.16)$$

For body coordinates, $\vec{\omega}_W$ must be transformed with L_{BE}; hence,

$$\begin{pmatrix} p_{rel} \\ q_{rel} \\ r_{rel} \end{pmatrix} = \begin{pmatrix} p \\ q \\ r \end{pmatrix} - L_{BE}\begin{pmatrix} \frac{1}{2}\left(\frac{\partial W_Z}{\partial Y} - \frac{\partial W_Y}{\partial Z}\right)_E \\ \frac{1}{2}\left(\frac{\partial W_X}{\partial Z} - \frac{\partial W_Z}{\partial X}\right)_E \\ \frac{1}{2}\left(\frac{\partial W_Y}{\partial X} - \frac{\partial W_X}{\partial Y}\right)_E \end{pmatrix} \qquad (2.17)$$

Thus the aerodynamic roll, pitch, and yaw rates are strongly dependent on the spatial derivatives of wind speed components, which are wind gradient terms.

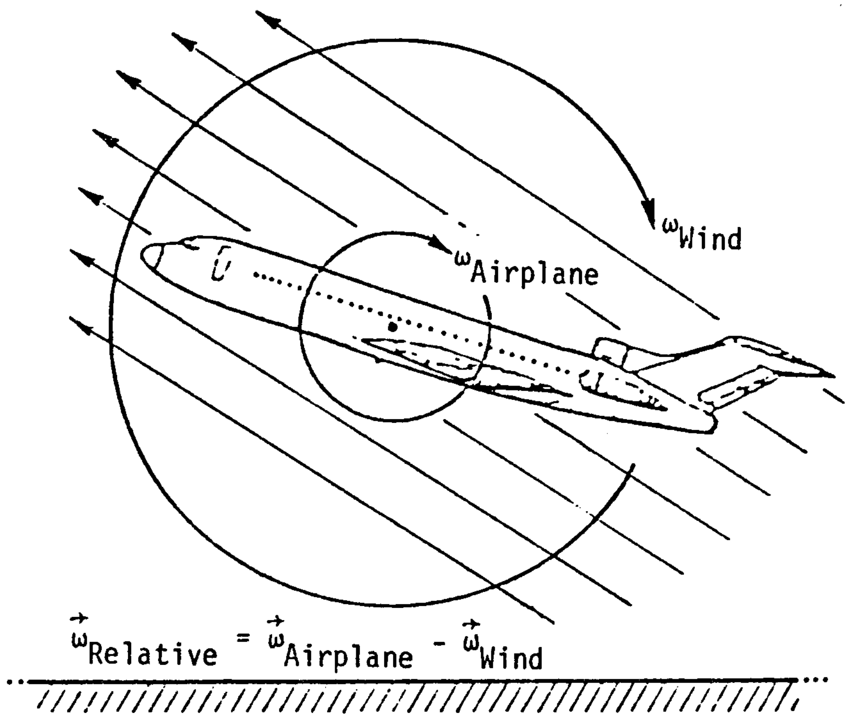

Figure 2.2. Schematic illustration of wind field rotation.

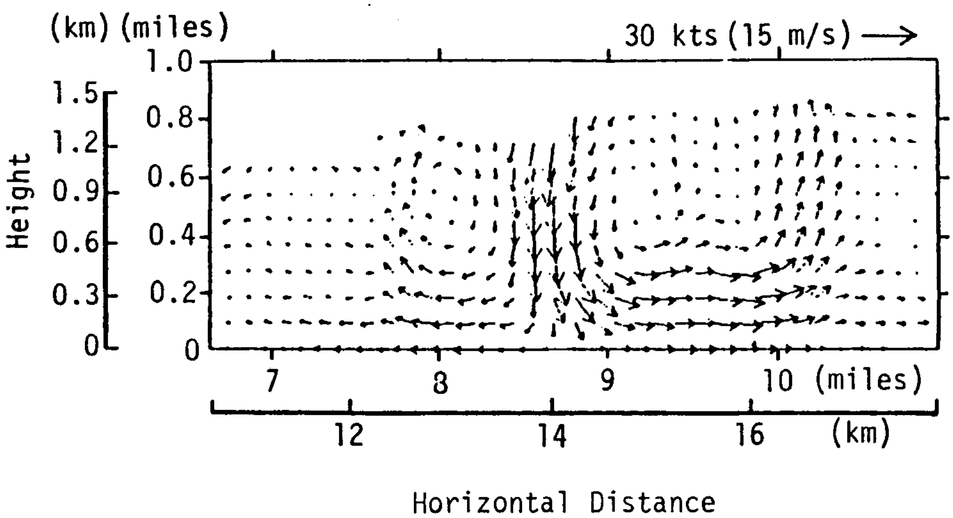

Figure 2.3. Vertical wind field in a severe microburst, seen over the JAWS network on July 14, 1982.

The physical parameters and stability derivatives of three different types of aircraft used in this study are listed in the appendix. The calculation of aircraft performance is carried out by solving the governing equations derived in Section 1 and by incorporating the wind shear effects discussed in Section 2. Numerical calculations to assess the influence of wind shear on aircraft dynamics are introduced in detail in Chapter IV.

CHAPTER III

SOURCES OF WIND SHEAR DATA

Prior to the development of JAWS, essentially all of the convective storm wind velocity data used to develop manned-flight and computer simulated model profiles were derived from two sources, flight data recorders (FDR), and tower data.

1. FLIGHT DATA RECORDERS

One principal source was the reconstruction of wind profiles derived from flight data recorders. These coarse profiles were obtained by making a number of assumptions which led to some data inaccuracies. Consequently, physically unrealistic flows were often obtained, particularly in the case of vertical velocity. Moreover, with the flight data recorder reconstructions, the resulting wind field is one dimensional. That is, since the data are obtained only along the flight track, the reconstruction presents only the derived flow "precisely" along the track. Thus, the two or three dimensionality of the real atmospheric wind variability is neglected or subjectively described in the model.

2. TOWER MEASUREMENTS

A second major source of convective storm wind field simulator data is the tall instrumented tower at Oklahoma City operated by the National Severe Storms Laboratory. Most of these tower data have been collected at seven levels--from the surface to approximately 1500 feet (450 m)--

during thunderstorm situations. Most of the cases used in the simulator work have involved gust front phenomena. The principal limitation of these data again relates to the spatial dimensionality problem. Since the tower is fixed geographically, the passage of the weather event is measured in the two-dimensional plane of the tower location. As in the FDR situation, this again constrains the realism of the spatial variation of the data set for simulation. Another problem relates to the rather long averaging time of the initial data set collected at the tower. In most of the derived models, the averaging period typically is around one minute. Consequently, many small-scale events are filtered from the data. Finally, none of these tower wind field models included a microburst profile.

3. JAWS DATA

Convective storm data from the above two sources were used by SRI International, Inc. to arrive at wind shear models for use in pilot training and in the testing of airborne wind shear detection and warning devices (Foy, 1979). However, because of the limitations of these current wind models, the JAWS project formulated a plan to collect and make substantially better wind shear profiles available. The JAWS project, conceived in 1980, conducted a major field investigation during the summer of 1982 (May 15 to August 13) in and around Denver, Colorado (Figure 3.1). The principal objective of JAWS was to examine convectively-driven downdrafts and resulting outflows near the earth's surface. Microburst, a term coined by Professor T. Fujita of the University of Chicago (Fujita, 1982), can be lethal for jet aircraft on

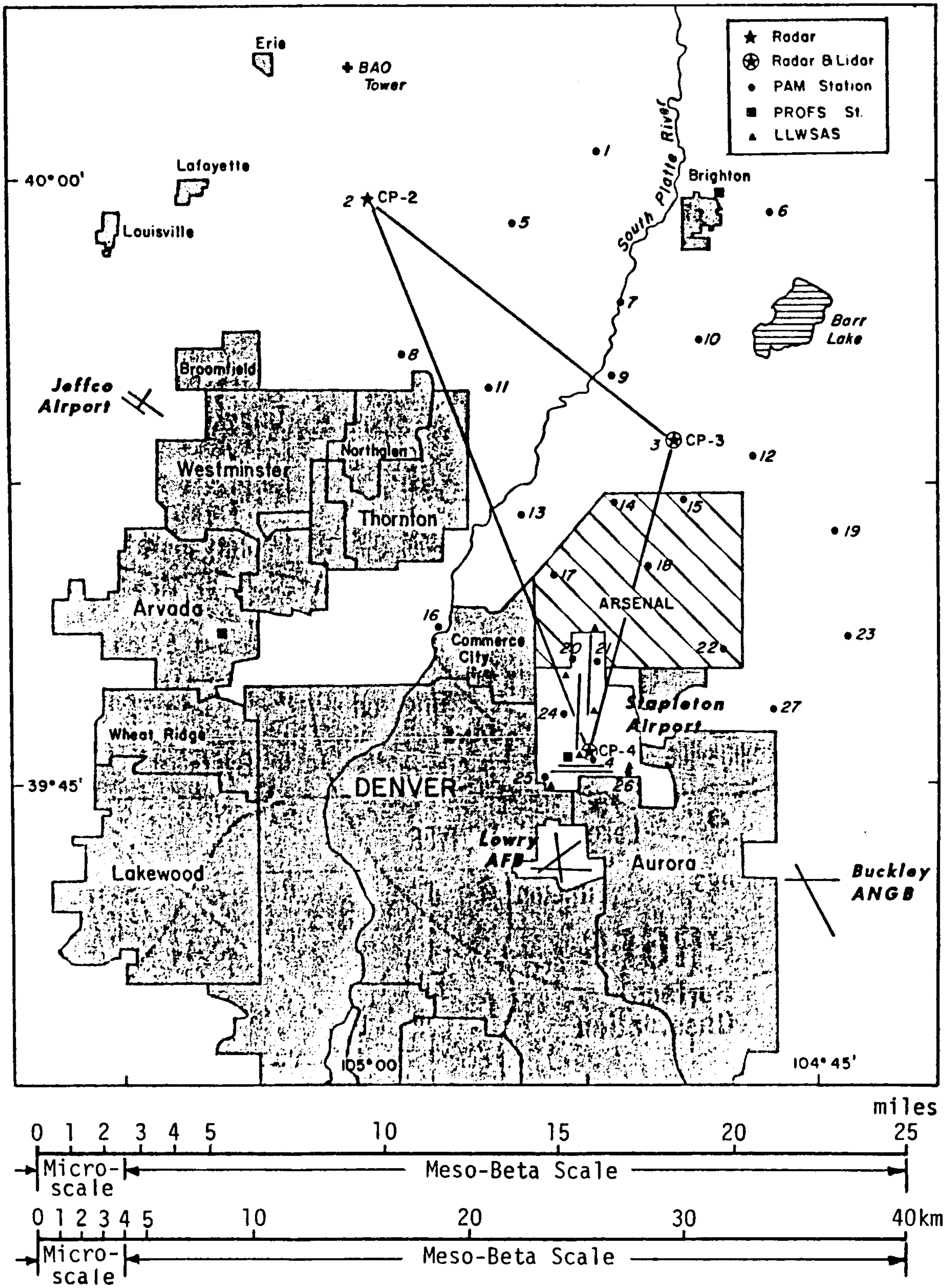

Figure 3.1. JAWS network fixed sites (Frost et al., 1985).

takeoff or on landing because of the extreme magnitude of the flows. The JAWS field experiment provided three-dimensional and time-dependent velocity fields of microbursts and other convective events such as gust fronts.

Three different microbursts which are composed of eight time-dependent measurements have been suggested for analysis by Frost et al. (1985). The coordinates of these three microbursts relative to the origin located at CP-2 are shown in Figure 3.2. To the east, x is positive and y is positive to the north. The JAWS August 5, 1982, microburst data set has been chosen for the wind shear input in this study. Table 3.1 lists the three-dimensional coordinates for data obtained at times of 1845, 1847, 1850, and 1852 MDT, respectively. The nomenclature to be used hereafter in this dissertation to identify the individual data sets is in the format DMMTTTT (day, month, time), e.g., 5AU1845. Each rectangular sampling volume contained 81 x 81 x 9 grid points with grid spacing, 492 x 492 x 820 feet (150 x 150 x 250 m). The total volume covered 7.46 x 7.46 x 1.24 miles (12 x 12 x 2 km). At each grid point the JAWS microburst data set provided radar reflectivity and wind vector components which were given in the rectangular coordinate system shown in Figure 3.2.

Figure 3.3 shows a partial plot of the ground plane horizontal wind vectors for the 5AU1847 microburst and the projection on the ground plane of the intended flight paths which are investigated in this study. The diverging outflow of the microburst is easily discernable, with the center located approximately at (-1.12 miles, -14.85 miles), (-1.8 km, -23.9 km). Paths were selected relative to the center of the microburst

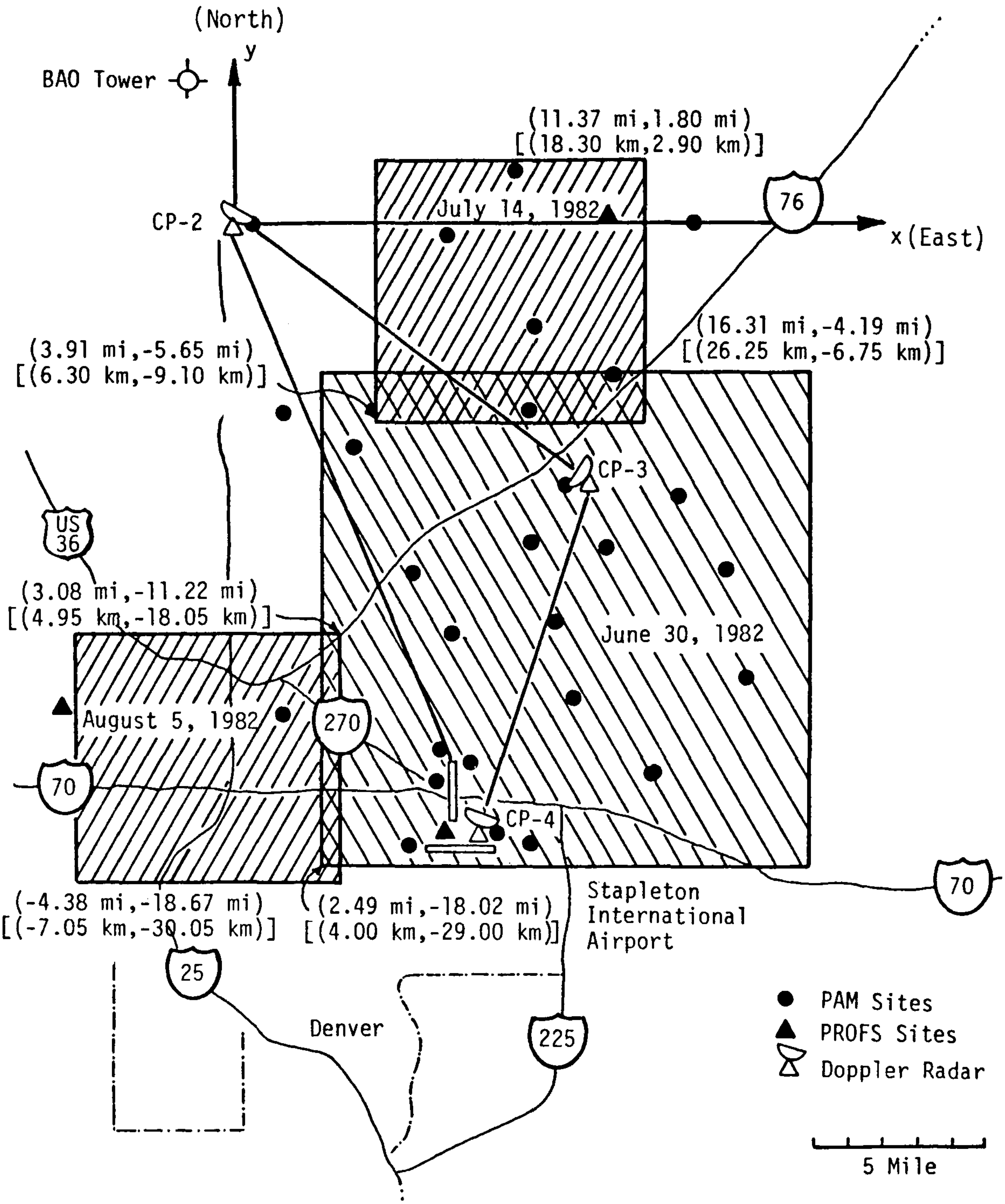

Figure 3.2. Location of JAWS data sets.

TABLE 3.1. Microburst Data Set Parameters.

			Location Relative to CP-2				
Date	Time (MDT)	Nomenclature	SW Corner Mile [Km]	NE Corner Mile [Km]	Vertical Height Mile [Km]	Grid Spacing Feet [Meter]	Number of Grids
5 August 1982	1845	5AU1845	(-4.38,-18.67) [(-7.05,-30.05)]	(3.08,-11.22) [(4.95,-18.05)]	1.24 [2]	492x492x820 [150x150x250]	81x81x9
"	1847	5AU1847	"	"	"	"	"
"	1850	5AU1850	"	"	"	"	"
"	1852	5AU1852	"	"	"	"	"

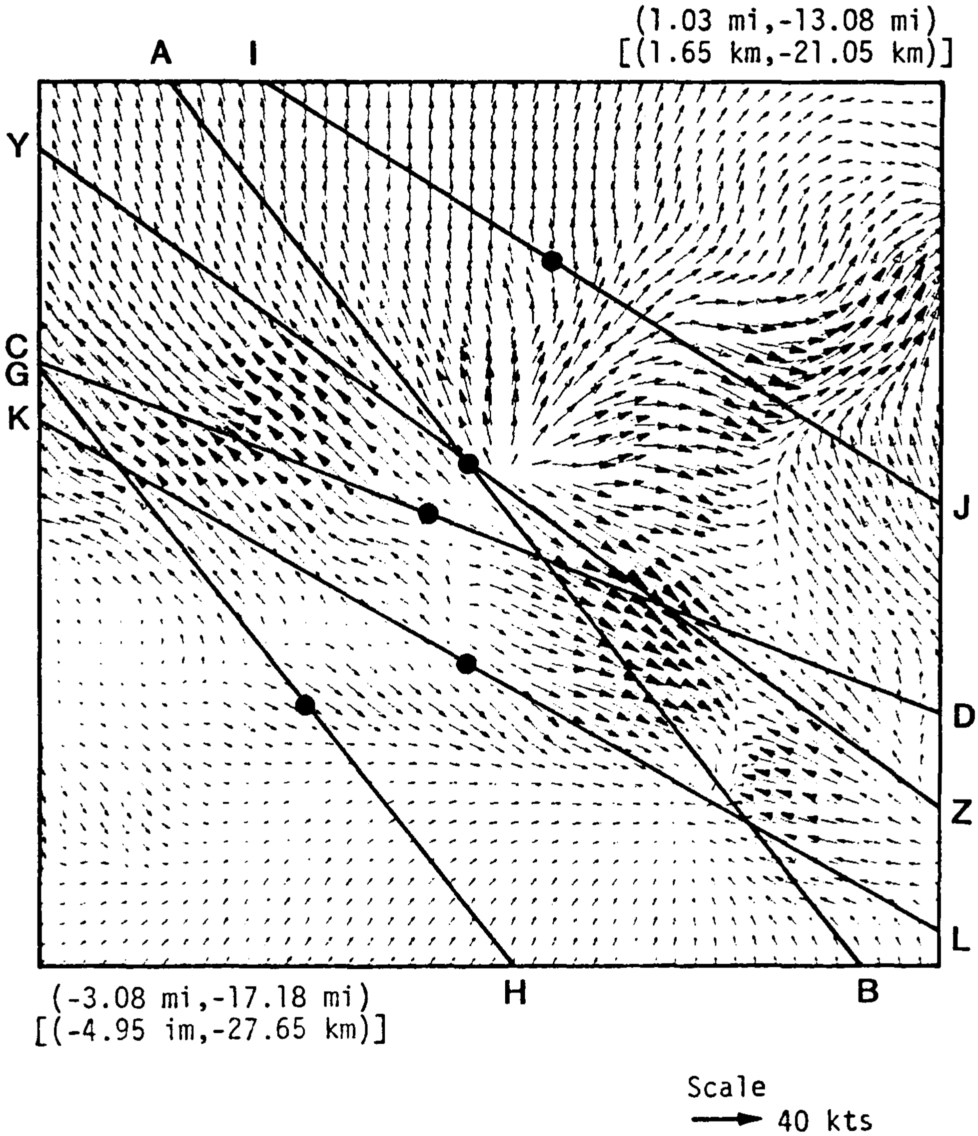

Figure 3.3. Flight paths chosen for wind shear simulations overlaid on ground level horizontal wind speed vectors, August 5, 1982, 1847 MDT.

with the objective of finding the maximum headwind-to-tailwind change in wind speed and/or unusual crosswind variations. Paths $\overline{AB}$, $\overline{YZ}$, and $\overline{CD}$ have approximately the maximum change in head-to-tailwind speed for either direction of flight. Flight path $\overline{IJ}$ was visually selected to give a crosswind shear. Flight paths $\overline{KL}$ and $\overline{GH}$ were selected to provide a measure of light but challenging wind shear. Finally, the solid circle shown on each path designates an effective center of the microburst for that particular intended flight path.

CHAPTER IV

NUMERICAL ALGORITHM

The governing equations, Equations 2.2, 2.8, 2.9, and 2.10, given in Chapter II, Section 1, are solved utilizing a fourth-order Runge-Kutta numerical scheme. An outline of the computational procedures is listed in Section 1. Section 2 introduces the techniques to interpolate the wind components and nine wind gradient terms for the point at which the aircraft is located within the grid system. Also, the flights with trim conditions of landing and takeoff for different types of aircraft are obtained in Section 3. Following this, the control laws used in this study are interpreted and tested. Finally, the numerical results in this study are evaluated by comparing these results with the outputs of the NASA Ames Research Center (NASA/Ames) simulator.

1. COMPUTATIONAL PROCEDURE

The computational procedure for calculating the aircraft dynamic performance is shown in Figure 4.1. The equations of motion associated with kinematic relations are solved in the body coordinate system. Twelve unknowns--u, v, w, p, q, r, ϕ, θ, ψ, X_E, Y_E, and Z_E--are obtained by solving the simultaneous differential equations shown in Figure 4.2. Thrust forces are also obtained by solving the differential equation defined by the thrust control logic introduced in Section 4 of this chapter. An accuracy criterion is input to adjust the marching time-step of the fourth-order Runge-Kutta scheme for each dependent

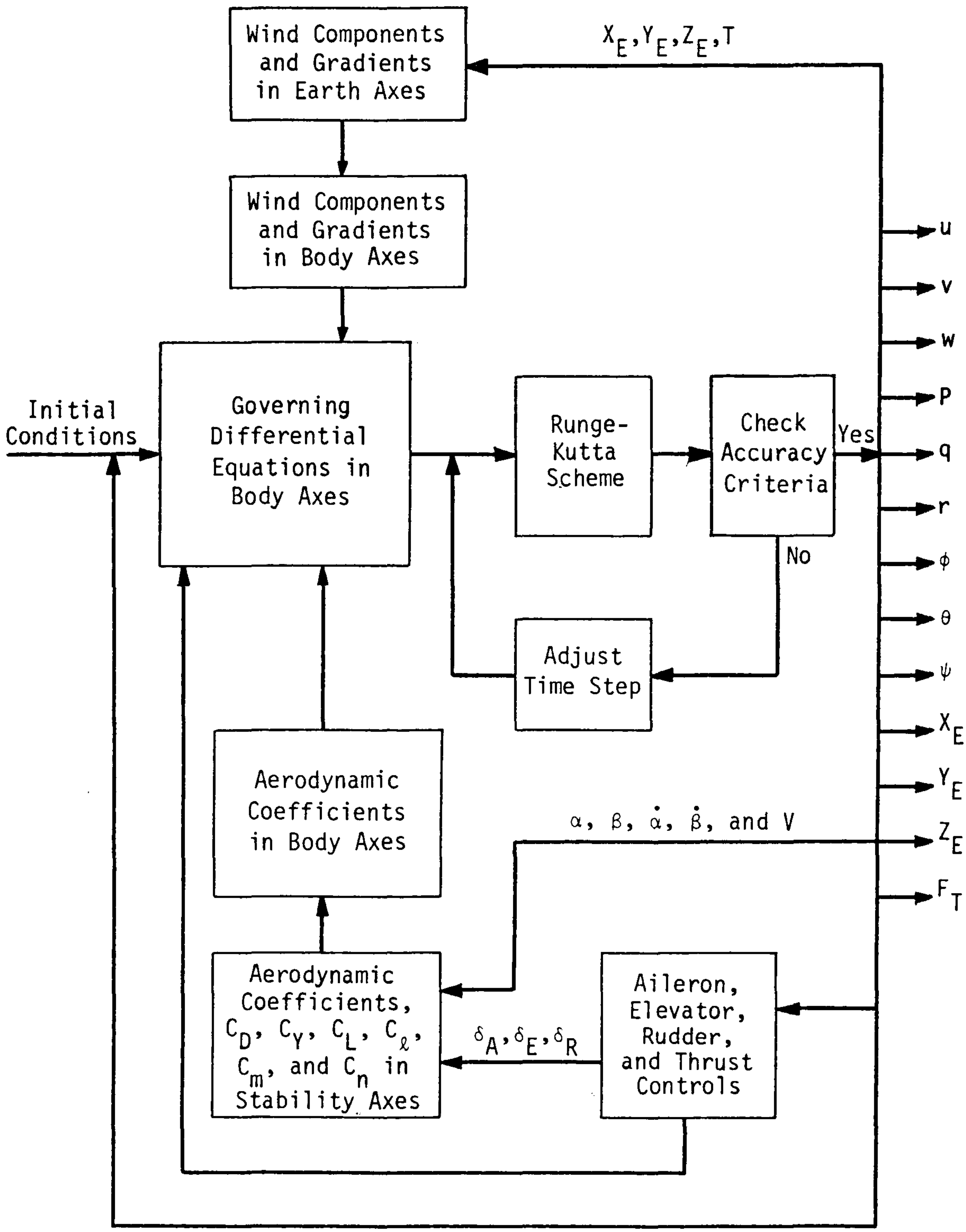

Figure 4.1. Block diagram of computational procedures.

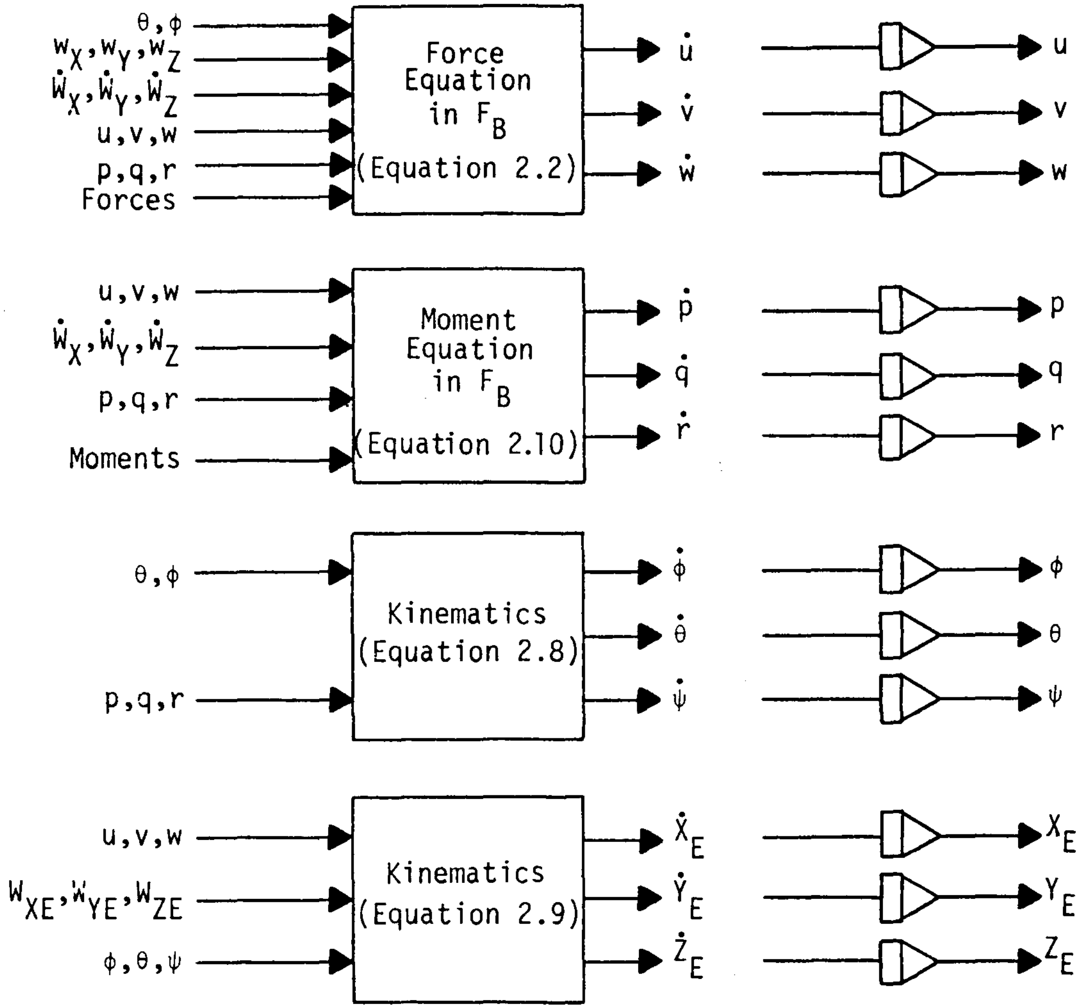

Figure 4.2. Block diagram of solution procedures in body coordinates.

variable. The accuracy criteria used in this study are less than 1 percent of the dependent variables at trimmed flight; the time-steps of the initial condition calculations technique are within 0.2 to 1.0 seconds.

2. INTERPOLATION TECHNIQUE

To carry out analysis of aircraft performance with the JAWS wind field data sets, the three wind speed velocity components along with their nine spatial and three temporal derivatives must be put into the aircraft governing equations of motion. Therefore, in order to utilize the spatially three-dimensional wind fields, it is necessary to three-dimensionally calculate the wind speed values at the aircraft's position.

Wind Speed Components

A volume-weighted interpolation scheme has been utilized to calculate the spatial wind speed components in this study. As mentioned earlier, the JAWS microburst data set provided the three wind speed components--longitudinal, latitudinal, and vertical--at each grid point. A rectangular sampling volume, wind speed data base, which consists of $M_X \times M_Y \times M_Z$ grid points is plotted in Figure 4.3. Figure 4.3 also illustrates the interpolation scheme. A sub-volume element of the grid is assumed to have velocity W_1, W_2, ... W_8 at each respective corner or grid point of the element. This volume element is then divided into eight further sub-volume elements through the aircraft position at point P. The sub-volume elements diagonal to the respective grid points are

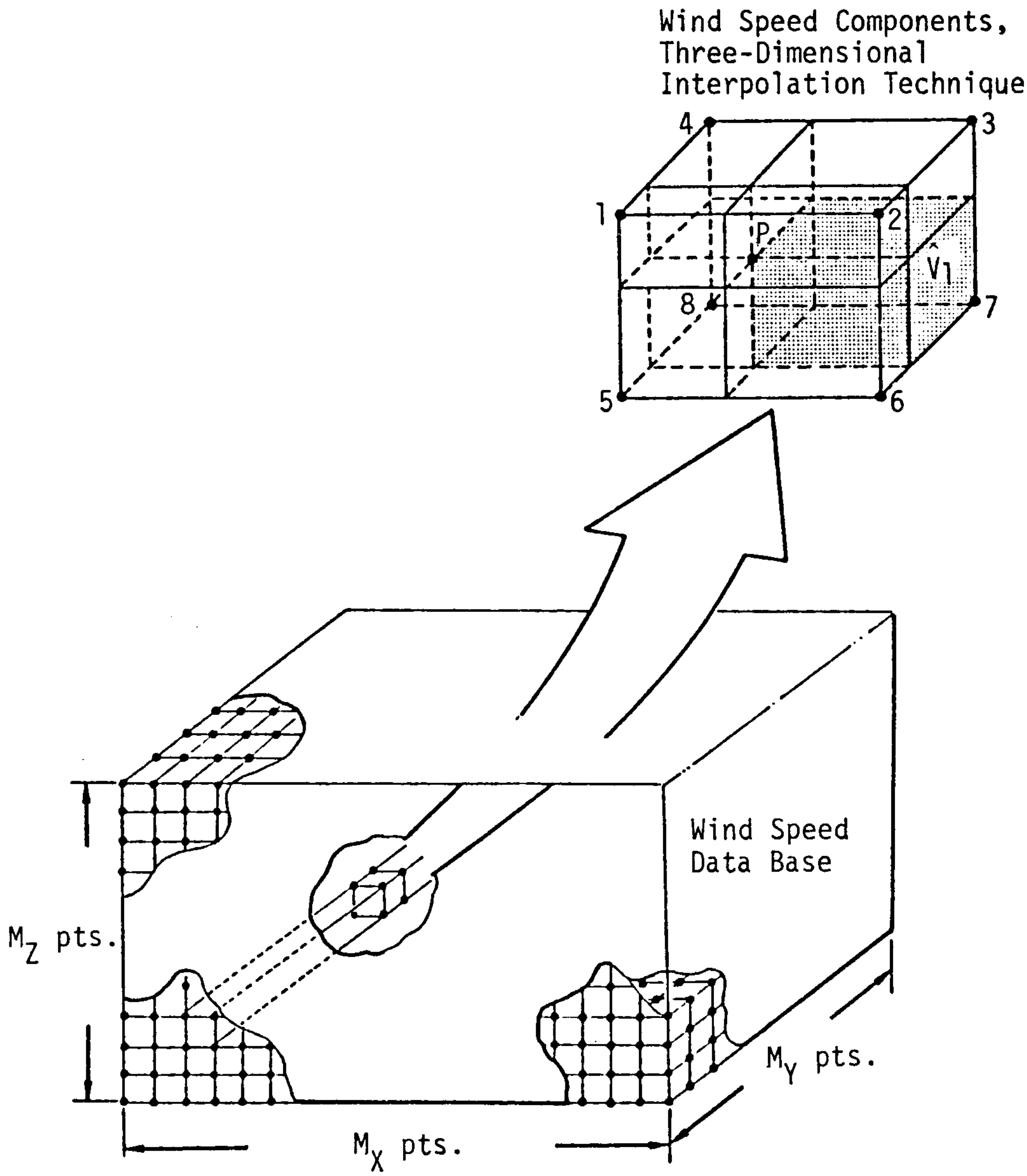

Figure 4.3. Schematic illustration of 3-D interpolation technique.

the weighting elements for averaging. Thus, the value of the wind speed at point P is given by:

$$W_P = \frac{\sum_{i=1}^{8} W_i \hat{V}_i}{\sum_{i=1}^{8} \hat{V}_i} \qquad (4.1)$$

where W_i $(i = 1, 2, \ldots 8)$ are the wind speeds at eight corners or grid points of the sub-volume element at which the aircraft is located, and $\hat{V}_i$ $(i = 1, 2, \ldots 8)$ are the volumes of the eight further sub-elements which are diagonal to the respective corner of the sub-volume element. For example, the shaded area in Figure 4.3 is $\hat{V}_1$.

In Figure 4.4 the longitudinal wind speed component W_{LONG} is plotted at ground level z = 0 feet, at an interpolated level z = 410 feet, and at the first grid level z = 820 feet of 5AU1847 microburst. The three-dimensional form of Figure 4.4 clearly illustrates the high variability of the wind and the general agreement of the interpolated results shown in Figure 4.4b.

Wind Gradient Terms

The form of the spatial derivative interpolation scheme is an area-weighted interpolation, as illustrated in Figure 4.5. P_{x1}, P_{x2}, P_{y1}, P_{y2}, P_{z1}, and P_{z2} are the projected points of the aircraft position, P, on each of the six planes of the sub-volume element, respectively. The value of wind speed at position P_{y1}, for example, is given by:

$$W_{P_{y1}} = \frac{W_1 \times A1 + W_2 \times A2 + W_5 \times A5 + W_6 \times A6}{A1 + A2 + A5 + A6} \qquad (4.2)$$

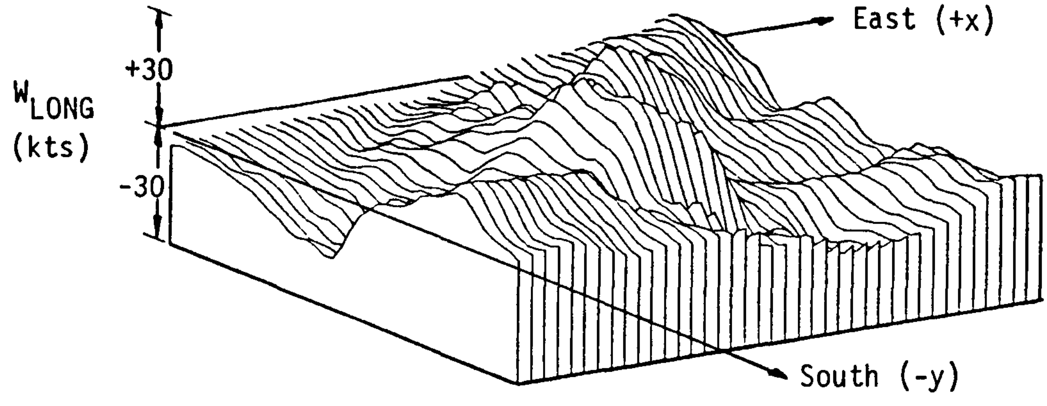

(a) W_{LONG} at the 820 ft (250 m) level

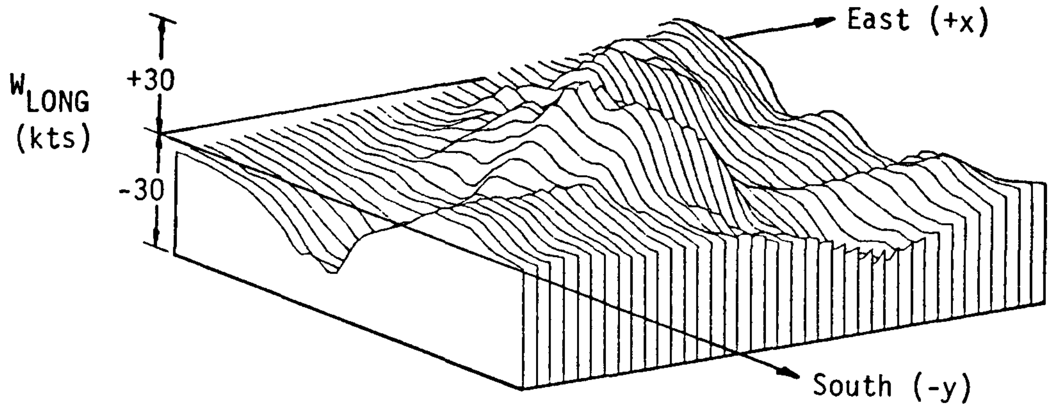

(b) W_{LONG} at the 410 ft (125 m) level (interpolated)

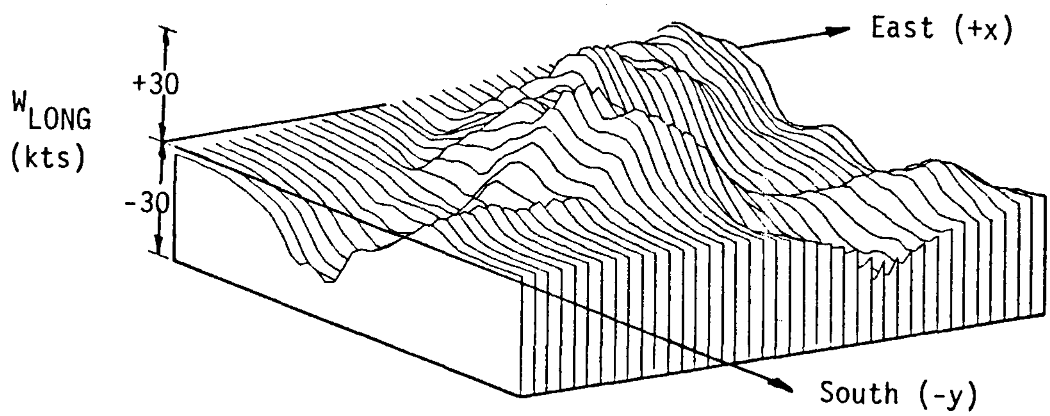

(c) W_{LONG} at ground level

Figure 4.4. Longitudinal wind speed component, W_{LONG}, at different vertical levels.

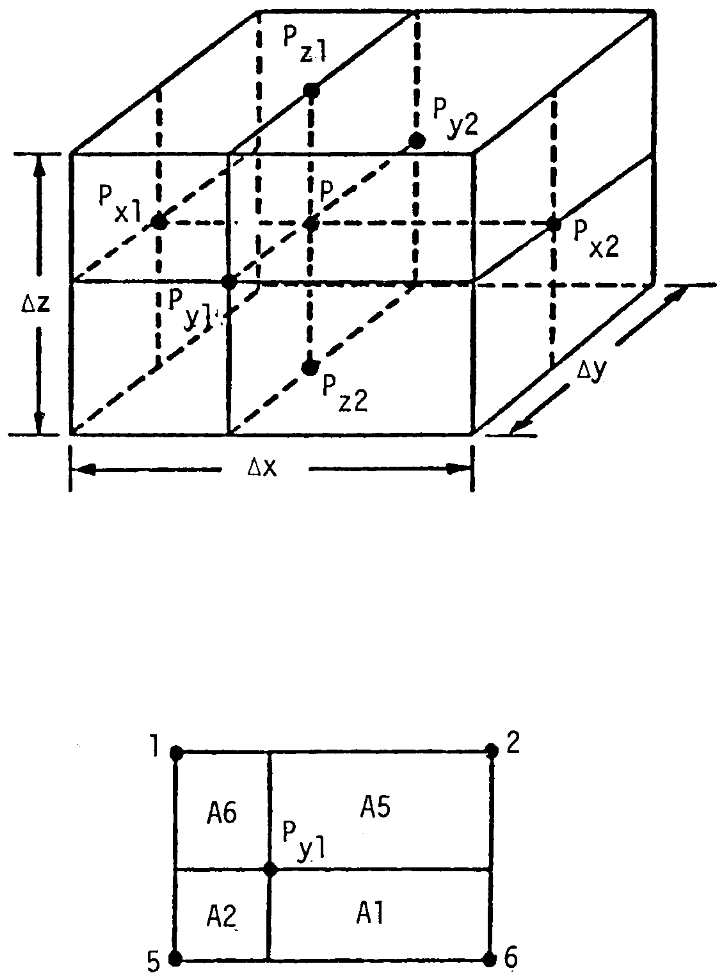

Figure 4.5. Illustration of wind speed spatial derivative interpolation scheme.

Similarly, the values of wind speed at the other projected points are obtained as $W_{P_{y2}}$, $W_{P_{x1}}$, $W_{P_{x2}}$, $W_{P_{z1}}$, and $W_{P_{z2}}$. The wind gradient term in each direction is then obtained from:

$$\left.\frac{\partial W}{\partial x}\right|_P = \frac{W_{P_{x2}} - W_{P_{x1}}}{\Delta x}\ , \quad \left.\frac{\partial W}{\partial y}\right|_P = \frac{W_{P_{y2}} - W_{P_{y1}}}{\Delta y}\ , \text{ and } \left.\frac{\partial W}{\partial z}\right|_P = \frac{W_{P_{z2}} - W_{P_{z1}}}{\Delta z} \tag{4.3}$$

Equation 4.3 is valid for W_x, W_y, and W_z. A plot of $\partial W_{LONG}/\partial x$ interpolated to the z = 410-foot level is shown in Figure 4.6.

Interpolation in Time Domain

The JAWS data sets also provide the possibility of four-dimensional wind shear models, the fourth dimension being time. Data sets separated in time by 2-minute periods are available for most of the microbursts measured during JAWS. An interpolation scheme between time fields has been developed.

The different measurements of a time-dependent microburst can be plotted on a time axis. 0, A, B, and C represent different data sets. Δt_1, Δt_2, and Δt_3 are the time intervals of the serial measurements. s is the starting time for the flight of interest. T_i can be adjusted for different starting time of a specific flight. The time-dependent wind components of an aircraft at s' can be evaluated as follows.

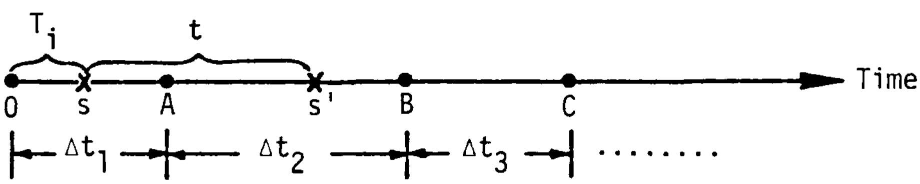

By using the three-dimensional (3-D) spatial interpolation technique described earlier, the wind speed corresponding to the aircraft's

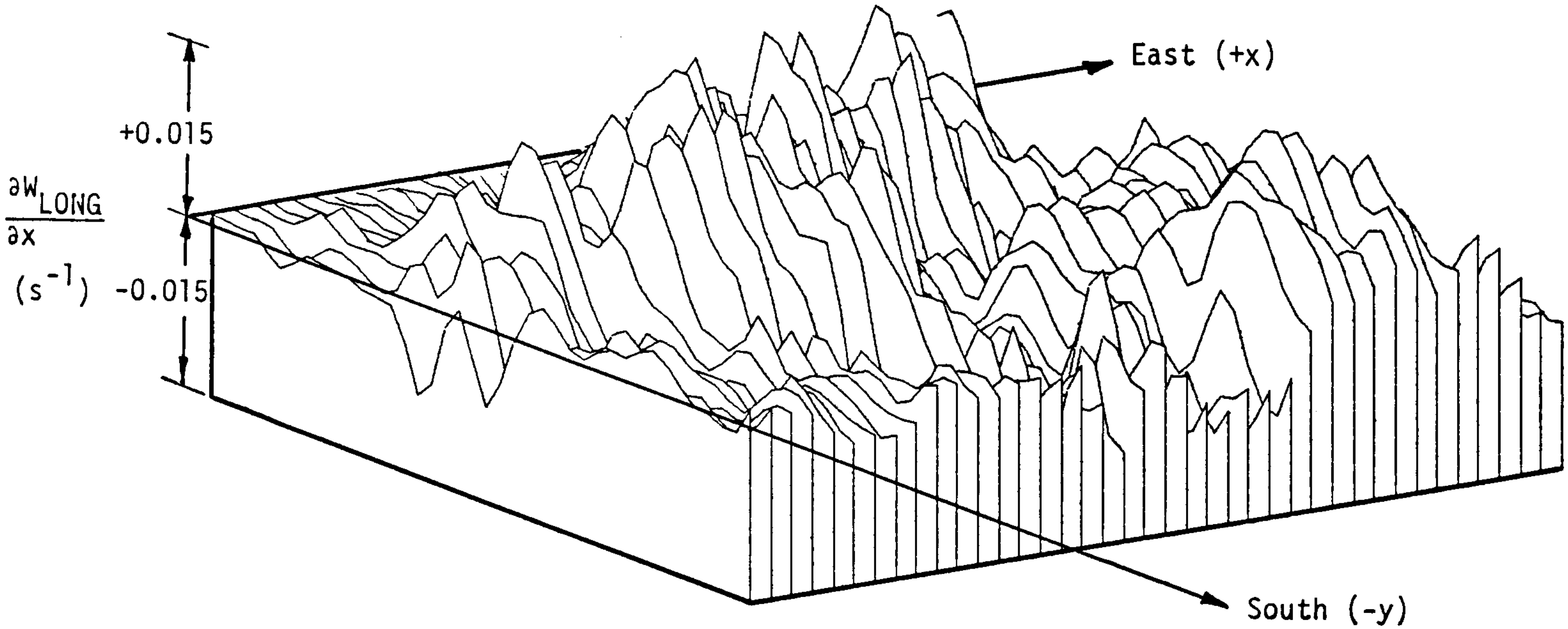

Figure 4.6. Interpolated spatial derivative of W_{LONG} in the x-direction (i.e., $\partial W_{LONG}/\partial x$) at 410 feet (125 m).

current position in adjacent volume measurements, B and A, can be evaluated as W_{PB} and W_{PA}, respectively. The time-dependent wind speeds of the aircraft are then obtained by a second interpolation in the time domain.

$$W_P = \frac{[(T_i + t) - \Delta t_1]}{\Delta t_2} \times (W_{PB} - W_{PA}) + W_{PA} \tag{4.4}$$

Also, the time derivative terms, $\partial W_P/\partial t$, can be approximated as:

$$\frac{\partial W_P}{\partial t} \simeq \frac{W_{PB} - W_{PA}}{\Delta t_2} \tag{4.5}$$

The techniques have been used to interpolate the wind shear data to investigate the influence of time variation on the aircraft performance in this study (see Section 4 of Chapter V).

3. TRIMMED FLIGHT

Prior to investigating the dynamic performance of an aircraft flying through the microburst region, the trim conditions of an aircraft landing or taking off in a zero or constant wind area should be calculated as a reference state. Three generic types of aircraft--a three-engine passenger airliner (PA), a twin-engine STOL (STOL), and an executive jet (EJ)--are chosen for the calculations.

Consider first the case of landing. The trim conditions are obtained by trial and error for the PA (B727-200) type airplane and by solving force and moment equations for the EJ and the STOL type airplanes. Figure 4.7 shows the trajectory projections on x-z and x-y planes for a B727-200 type airplane, which is making a trimmed approach with zero wind. The flight path angle, γ, is three degrees. The

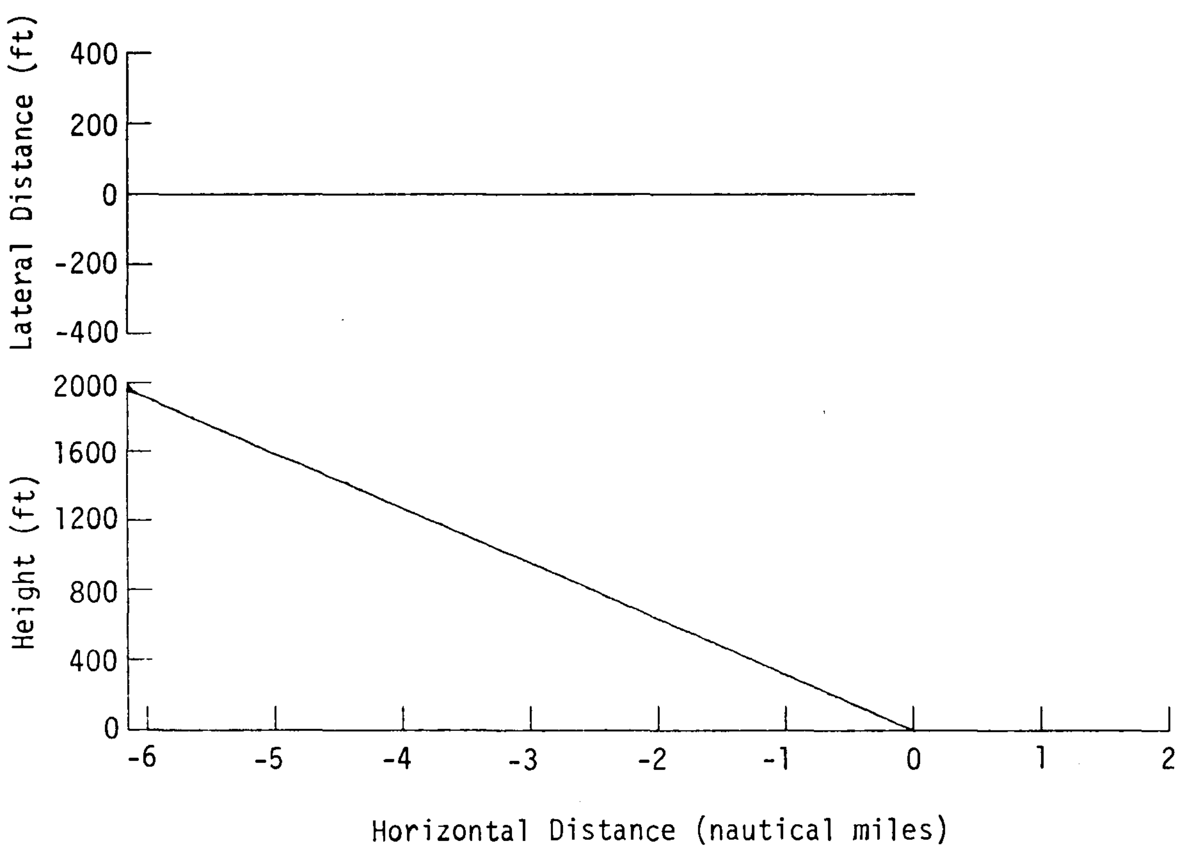

Figure 4.7. Trimmed flight of a B727-200 type airplane in landing.

aerodynamic parameters required for trimmed landing conditions for the PA, STOL, and EJ type airplanes are listed in Table 4.1.

The reference state for takeoff was determined as follows: the aircraft thrust is increased through the thrust control law, which is presented in the next section, until the aircraft accelerates to 65 knots of airspeed. The thrust, which is about 75 percent of maximum thrust, is then held constant as the aircraft reaches takeoff speed.

At takeoff speed, a 10° pitch angle is commanded. The rate of pitch angle increase is controlled at 3° per second until a 10° pitch attitude is established. The aircraft then climbs along an approximate 6.4° takeoff path. With a zero wind condition, the B727-200 type aircraft requires approximately 5000 feet of runway before liftoff

TABLE 4.1. Trim Landing Conditions.

	Airplane Types		
Condition	PA	STOL	EJ
Glide slope angle (degrees)	3.00	3.00	2.96
Airspeed (knots)	136.00	70.00	147.00
Flap angle (degrees)	30.00	40.00	50.00
Angle of Attack (degrees)	7.20	5.61	8.28
Stabilizer incidence (degrees)	-5.62	---	-6.20
Elevator deflection angle (degrees)	---	-5.49	---
Thrust (lbf)	13762	2343	5147

occurs. Figure 4.8 shows the trajectory and dynamic performance of a B727 type aircraft on takeoff in still air. The liftoff point of the aircraft is at approximately 5000 feet from the beginning of the runway. During the climbout, pitch angle, climb rate, and airspeed of the aircraft are converging to approximately 10 degrees, 1800 fpm, and 160 knots, respectively. The B727 type aircraft is the only airplane for which takeoff simulations were studied.

4. CONTROL LAWS

A simple automatic control logic has been developed by Turkel et al. (1981). The control laws are extended to rudder and aileron controls in this study. The automatic control laws are expressed as simple expansions in a Taylor series:

Elevator Deflection:

$$\delta_E = \delta_{EN} + \frac{\partial \delta_E}{\partial \dot{Z}} (\dot{Z} - \dot{Z}_R) + \frac{\partial \delta_E}{\partial \theta} (\theta - \theta_N) + \text{higher order terms} \tag{4.6}$$

Rudder Deflection:

$$\delta_R = \delta_{RN} + \frac{\partial \delta_R}{\partial \dot{Y}} (\dot{Y} - \dot{Y}_R) + \frac{\partial \delta_R}{\partial \psi} (\psi - \psi_N) + \text{higher order terms} \tag{4.7}$$

Aileron Deflection:

$$\delta_A = \delta_{AN} + \frac{\partial \delta_A}{\partial \dot{Y}} (\dot{Y} - \dot{Y}_R) + \frac{\partial \delta_A}{\partial \phi} (\phi - \phi_N) + \text{higher order terms} \tag{4.8}$$

Rate of Change of Thrust Setting:

$$\delta_T = \delta_{TN} + \frac{\partial \delta_T}{\partial \dot{X}} [(\dot{X} + t_c \ddot{X}) - \dot{X}_N] + \text{higher order terms} \tag{4.9}$$

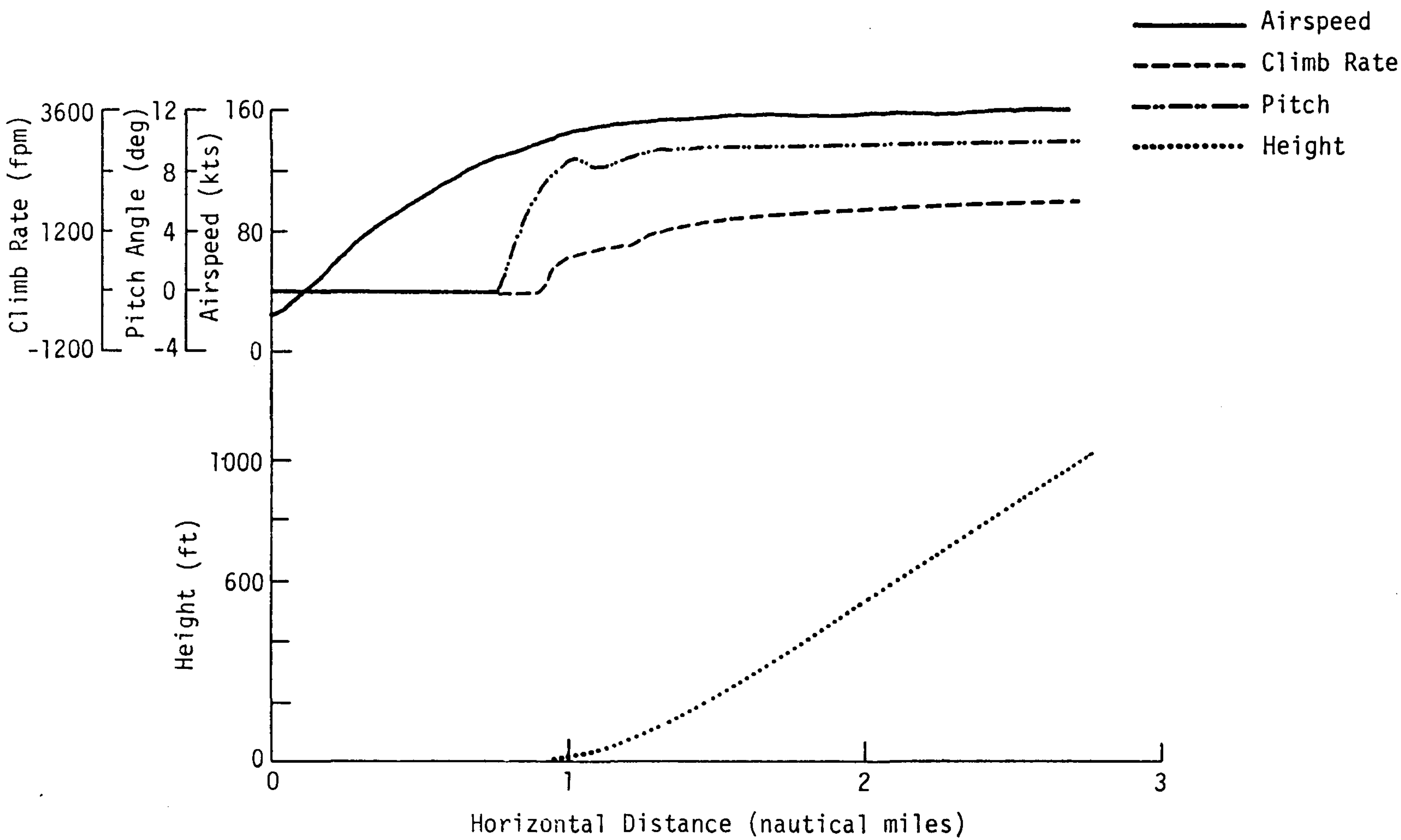

Figure 4.8. Trimmed flight trajectory of a B727-200 type aircraft in takeoff.

$$\frac{d\dot{F}_T}{dt} = \frac{\delta_T - \dot{F}_T}{t_c} \tag{4.10}$$

$$\frac{dF_T}{dt} = \dot{F}_T \tag{4.11}$$

where t_c is turbomachinery lag time; δ_{EN}, δ_{RN}, δ_{AN}, and δ_{TN} are the trim values (zeros in trimmed flight) for elevator, rudder, aileron, and thrust setting, respectively. The differential equations, Equations 4.10 and 4.11, are also solved by the fourth-order Runge-Kutta numerical scheme mentioned earlier. $\dot{Z}_R$ and $\dot{Y}_R$ are the reference sinking speed for controlling elevator deflection and the reference sideslip speed for controlling rudder and aileron deflections, respectively. These reference speeds are adjusted along the flight path, based on the aircraft's position relative to the intended touchdown (or liftoff) point and its ground speed. However, $\dot{X}_N$ is the trimmed airspeed of the aircraft and is used as a reference speed to control the rate of change of thrust setting. Elevator, rudder, and aileron control logics also use θ_N, ψ_N, and ϕ_N, the trim conditions of an aircraft, as reference pitch, yaw, and roll angles. The other higher order terms are neglected in this study. Finally, $\partial\delta_E/\partial\dot{Z}$, $\partial\delta_E/\partial\theta$, $\partial\theta_R/\partial\dot{Y}$, $\partial\delta_R/\partial\psi$, $\partial\delta_A/\partial\dot{Y}$, $\partial\delta_A/\partial\phi$, and $\partial\delta_T/\partial\dot{X}$ are called gain factors for elevator, rudder, aileron, and thrust controls, respectively. The gain factors were determined by trial and error, as follows.

Recalling the intended flight paths plotted in Figure 3.3, page 26, an aircraft encounters strong wind shear effects along paths $\overline{AB}$, $\overline{YZ}$, and $\overline{CD}$ and less wind shear effects along paths $\overline{GH}$ and $\overline{KL}$. Gain factors for the control laws used in this study are adjusted to allow the aircraft to fly safely along path $\overline{GH}$, which has the intended touchdown point at the effective center of the microburst (see Figure 3.3).

Figure 4.9 shows the longitudinal and lateral trajectory projections of a B727-200 type aircraft approaching through the wind field along path $\overline{GH}$. The point with zero horizontal distance is the intended touchdown point, the threshold of the runway. The trajectory projections of stick-fixed case are plotted as dashed lines which show that the airplane crashes 3000 feet short and 400 feet off the centerline of the runway. The projections of the trajectory with the automatic control mode in operation are also shown in Figure 3.3, page 26 (solid lines). The gain factors for which the automatic control algorithm effectively controls the B727-200 type aircraft through the wind field along path $\overline{GH}$ were used throughout the remainder of the study. Similarly, gain factors for the STOL and EJ type aircraft were obtained.

Similar gain factors were obtained to assure a successful takeoff through the wind field along path $\overline{GH}$. Table 4.2 lists the gain factors so determined for the different types of airplanes used for landing and/or takeoff computer simulations in this study.

To test the control laws determined above, aircraft response to a step gust[†] in the longitudinal and in the lateral wind speed are calculated. Figure 4.10 shows the trajectory, pitch angle, elevator deflections, and thrust ratio of the aircraft when a B727-200 type aircraft encounters a 20-knot step in longitudinal wind speed. Figure 4.11 shows the response of the same airplane to a 12-knot lateral step. The

---

[†]Step gust is simulated by a sudden wind speed increase which is then maintained for the duration of the landing.

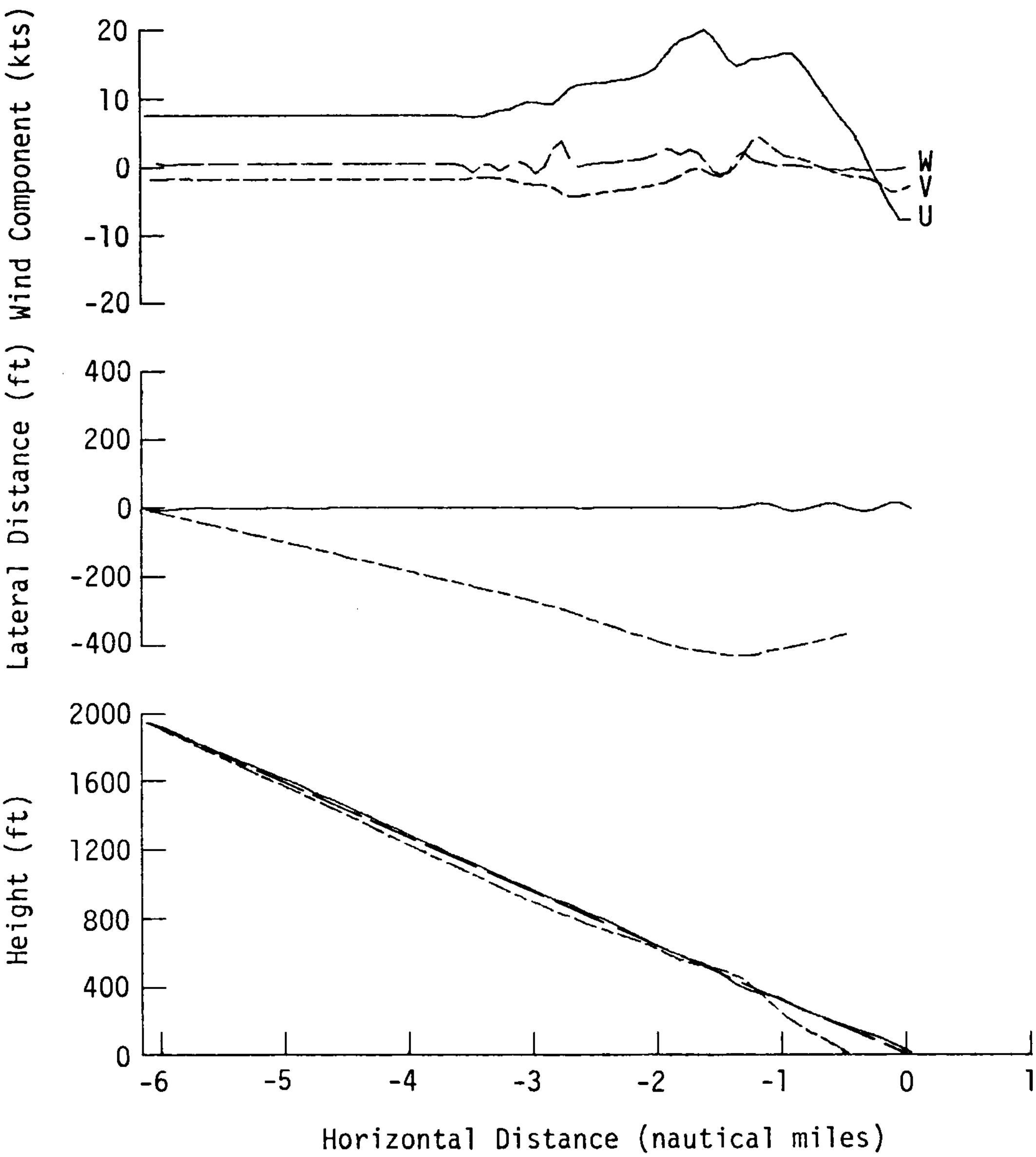

Figure 4.9. Trajectories of B727-200 type aircraft through wind field along path $\overline{GH}$ with (solid) and without (dashed) the control laws.

TABLE 4.2. Gain Factors of Control Laws for Different Airplane Types.

Gain Factor	Landing Cases PA	Landing Cases STOL	Landing Cases EJ	Takeoff Case PA
$\partial\delta_E/\partial\dot{Z}$ (rad/ft·s^{-1})	-0.003	-0.01	-0.003	-0.003
$\partial\delta_E/\partial\theta$	0.1	0.2	0.1	0.1
$\partial\delta_R/\partial\dot{Y}$ (rad/ft·s^{-1})	-0.03	-0.017	-0.002	-0.03
$\partial\delta_R/\partial\psi$	-0.1	-0.05	-0.006	-0.1
$\partial\delta_A/\partial\dot{Y}$ (rad/ft·s^{-1})	-0.00003	-0.00003	-0.00003	-0.00003
$\partial\delta_A/\partial\phi$	-0.06	-0.08	-0.08	-0.06
$\partial\delta_T/\partial\dot{X}$ (lbf/ft·s^{-1})	-68.5	-17.1	-23.6	-30.8

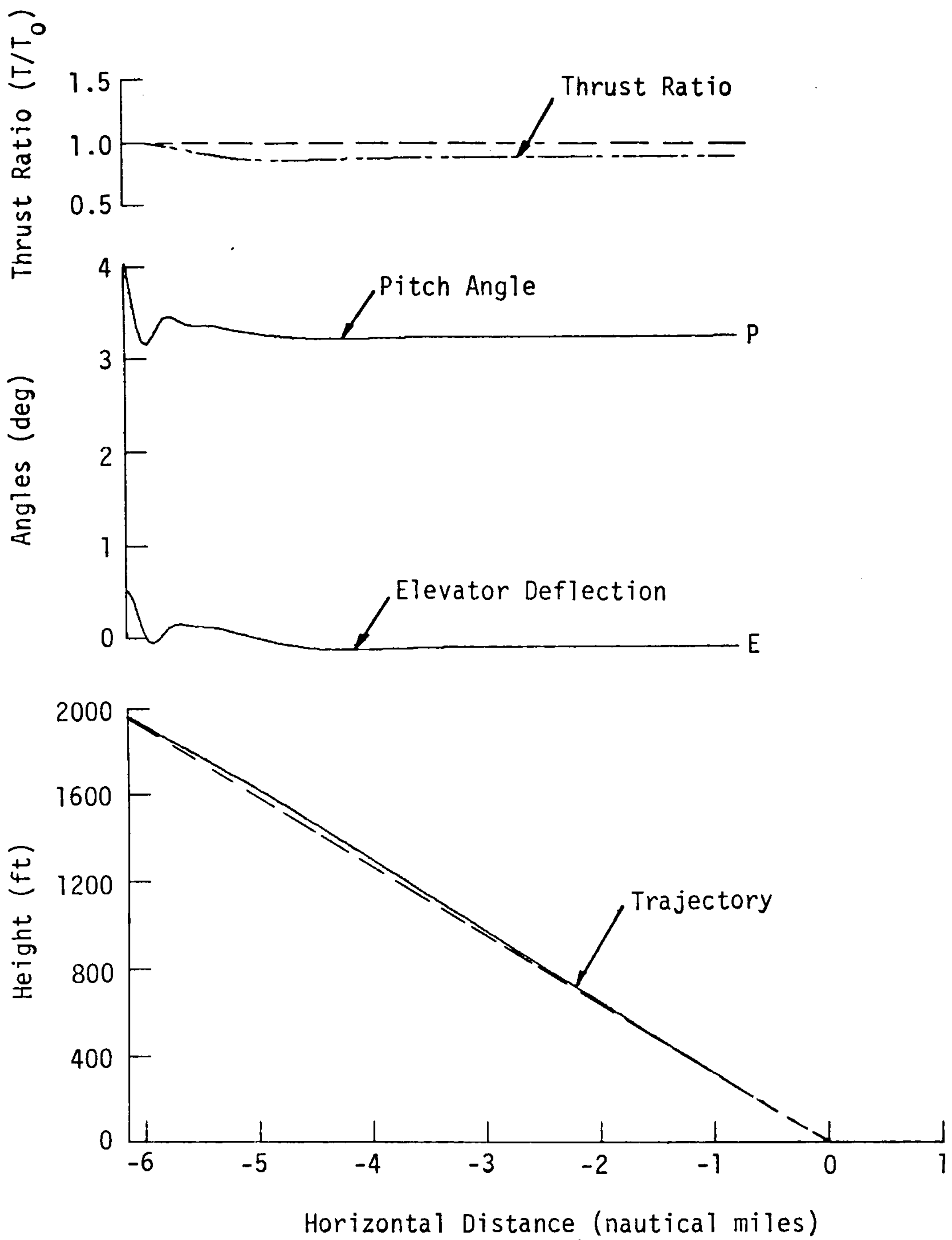

Figure 4.10. Dynamic responses of B727-200 type aircraft to a longitudinal step gust (20 kts).

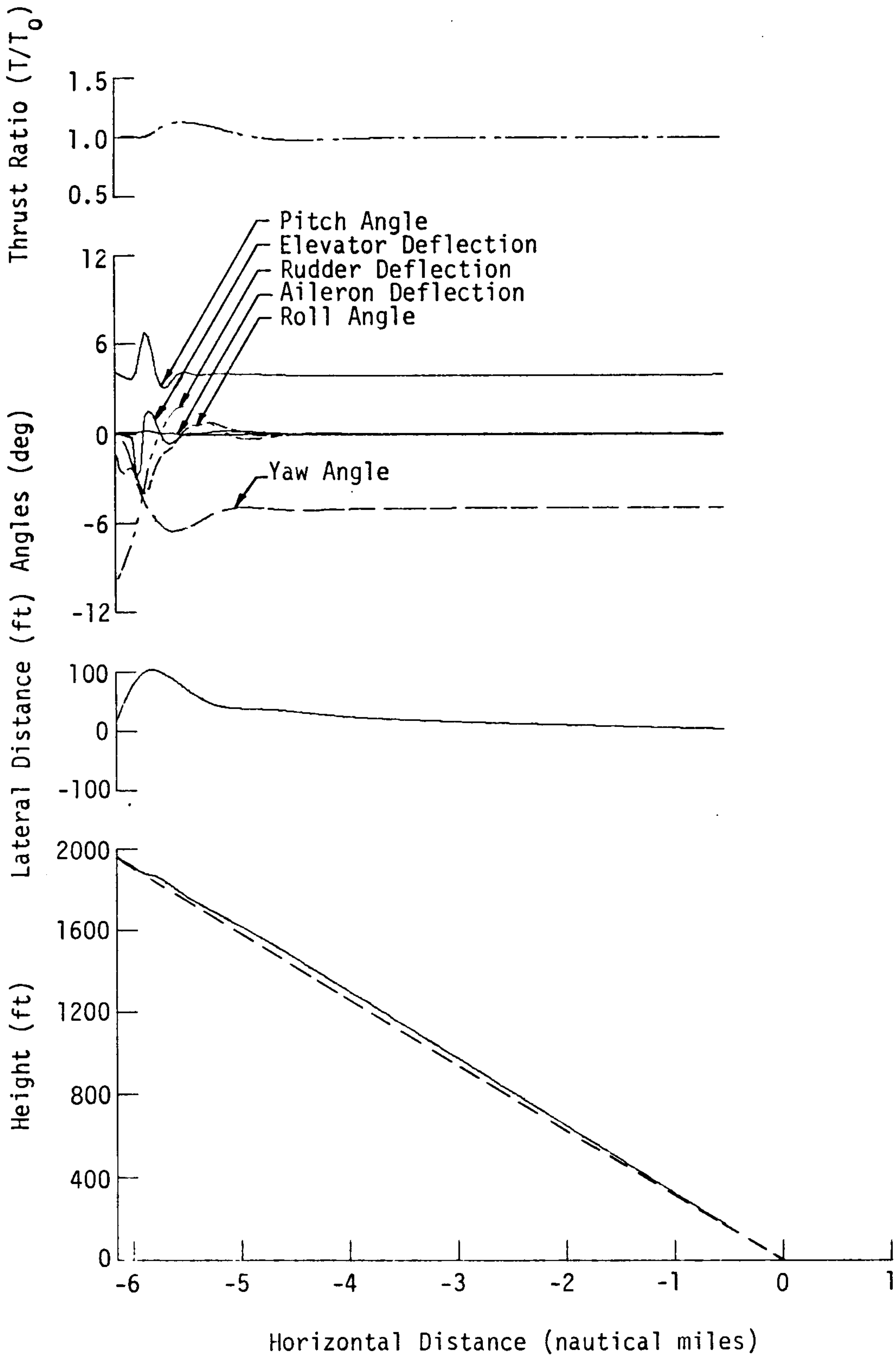

Figure 4.11. Dynamic responses of a B727-200 type airplane to a lateral step gust (12 kts).

trajectory, the deflections of elevator, rudder, and aileron, and the pitch, yaw, and roll angles are shown. As predicted, the lateral disturbances induce changes in longitudinal attitude.

Finally, selective go-around commands, consisting of full thrust and 15° pitch angle commands, are used during landing flights. The approach criterion callo for an aircraft to attempt a go-around if it is outside a 0.7° localizer/glide slope cone centered on the ILS beam. This go-around criterion is somewhat less precise than that used in practice. In practice, a pilot typically initiates go-around if he is one "dot" (approximately 0.2°) outside the localizer/glide slope. The go-around command used in this study is only applied if the aircraft is above 100 feet altitude.

5. EVALUATION OF NUMERICAL SOLUTION

Although numerous studies of the wind shear influences on aircraft performance have been conducted, very few, if any, studies with three-dimensional spatial and time-dependent wind shear models have been presented. Therefore, the numerical solutions in this study are compared with the results of NASA/Ames B727-200 simulator flights (Bray, 1984) and the recorded data of NASA B-57B airplane flights (Camp et al., 1984).

Figure 4.12 shows the results from the present numerical model applied to the takeoff of a B727-200 type aircraft and the outputs from the NASA/Ames B727-200 manned flight simulator flying through almost the same wind conditions. Figure 4.12a shows the aircraft's trajectory; airspeed, the encountered wind components, angle of attack, pitch angle,

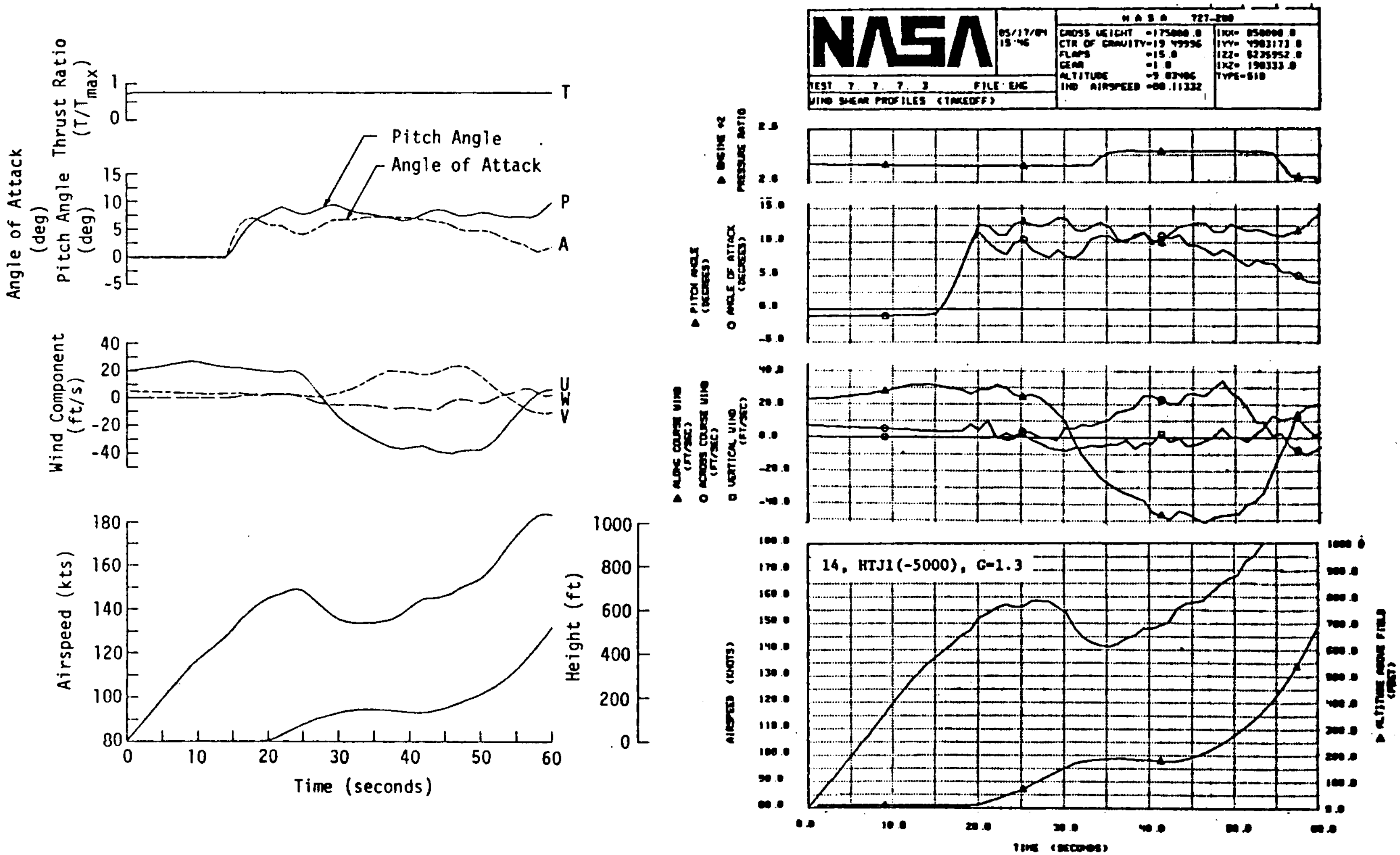

a. Present computed results

b. NASA/Ames simulator outputs

Figure 4.12. Comparison of the present computed results and the manned simulator outputs for a takeoff simulation of a B727-200 type aircraft.

and thrust ratio (relative to the maximum thrust, T_{max}) along the computed trajectory. The aircraft takes off rather well to an altitude of 150 feet with a peak airspeed of about 150 knots. Then, the aircraft encounters a rapidly decreasing headwind, which is followed by an increasing tailwind, and loses its airspeed by 15 knots. During this period, the aircraft almost makes a level flight when its pitch angle decreases about two degrees and its angle of attack increases approximately two degrees. However, the aircraft survives the peak of the encountered tailwind and then climbs out normally with an increasing airspeed. The pitch angle of the aircraft is converging to the intended values, 10 degrees. The same information from the NASA/Ames B727-200 manned flight simulator is plotted in Figure 4.12b except that the pressure ratio of engine #2 substitutes for the thrust ratio, which is unavailable in Bray (1984).

The comparison of Figures 4.12a and 4.12b shows good agreement in aircraft trajectory and its airspeed, pitch angle, and angle of attack. Because the simulator flights receive direct pilot commands, the computer results are much smoother than those of the manned simulator.

Figures 4.13a and 4.13b show the same comparison for the case of a B727-200 type aircraft landing. In this case, the thrust ratio is calculated relative to the thrust time condition, T_o. Although the aircraft encounters slightly different wind conditions between computer simulation and NASA/Ames manned simulator, the variation tendency of its aerodynamic performance along the trajectory is still compatible.

In addition to the comparison with the NASA/Ames manned flight simulator made above, the computed dynamics of a B-57B airplane have

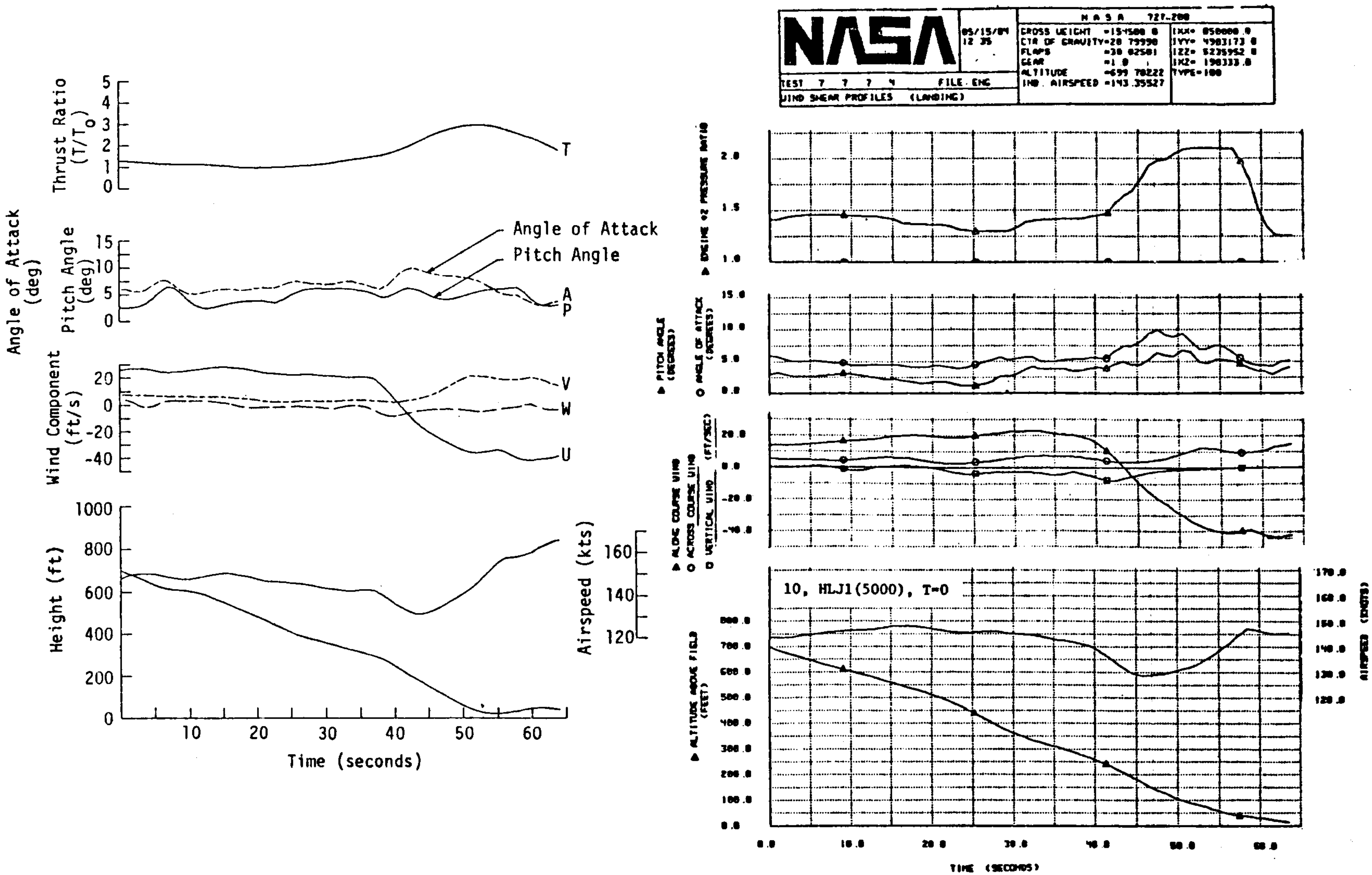

a. Present computed results

b. NASA/Ames simulator outputs

Figure 4.13. Comparison of the present computed results and the manned simulator outputs for a landing simulation of a B727-200 type aircraft

been compared with the recorded data of B-57B during a turbulence data gathering flight. The NASA B-57B aircraft is instrumented with an inertial navigation system to record all inertial aircraft motions and with instruments to measure the wind speeds relative to the aircraft. Thus, atmospheric turbulence can be determined from the flight data. In addition, the control surface deflections which are the commands of pilots are measured and recorded. Ringnes and Frost (1984) used the same computer program and control algorithm to study the dynamic performance of the B-57B flying through a turbulence wind field. The numerical output of the six-degrees-of-freedom computation showed good agreement with B-57B recorded flight data. Therefore, it is concluded that the numerical computer model with the simple automatic control laws provides realistic aircraft dynamics in variable and turbulent wind fields.

CHAPTER V

RESULTS AND DISCUSSION

Using the computational model explained in Chapter IV and the JAWS wind shear data, the dynamic performance of an aircraft flying through a microburst was computed. The results are presented in this chapter. Initially, the aircraft's dynamic response to wind shear is investigated by inspecting the deviation of the trajectory from the intended flight path; the aircraft attitude response and the sink rate during landing or the climb rate during takeoff. Several of the flight trajectories are discussed relative to the ILS CAT II decision height window as a reference. The influence of the wind gradient terms identified in Chapter II is quantified by measuring the departure distance at the intended decision height window. Also, the influence of the terms is quantified by calculating the standard deviation of the dynamic response of the aircraft for approach along 12 flight paths through the microburst center at various separation distance. A comparison of the wind shear effects on different generic types of aircraft is then presented. Finally, the influence of time-dependent wind shear on aircraft response is shown and the model discussed.

1. AIRCRAFT PERFORMANCE IN WIND SHEAR

Several computer simulated flights of a B727-200 type aircraft flying through the JAWS August 5, 1982, 1847 MDT, microburst are presented. According to the dynamic performance, the severity classification of wind shear effects is also defined.

Figure 5.1 illustrates the nomenclature used in defining the orientation of the runway to the wind field for the approach studies. To investigate the influence of the microburst position relative to the intended touchdown point on the runway, the center of the microburst is mathematically shifted along the path with respect to the threshold of the runway. The runway is positioned relative to the center of the microburst such that an aircraft following the glide slope passes through the center of the microburst at a given height designated as z_0. The intended touchdown point, TD (in Figure 5.1), is the threshold of the runway corresponding to the specific flight path. The distance of the threshold from the microburst center is calculated as z_0/tan (glide slope angle). A value of $z_0 = 0$ corresponds to the threshold of the runway coinciding with the microburst center. The orientation of the runway, θ, is measured relative to the positive x direction. The (x_0, y_0) coordinates designate the position in the horizontal plane at which z_0 is measured. Values of x_0 and y_0 are measured relative to an origin located at the northwest corner of the data set. For the August 5 case, the origin is at (-4.38 miles, -11.22 miles), (-7.05 km, -18.05 km), as measured from CP-2 (see Figure 3.2, page 24).

Recall the go-around command described in Chapter IV. At go-around decision, full thrust is applied and a 15° pitch angle is commanded. Go-around is attempted if at any time the aircraft is outside a 0.7° localizer/glide slope. If the aircraft cannot achieve go-around with a 15° pitch angle command for the wind case under study, the case is re-run with a 20° pitch angle command. If a go-around fails in both cases, the wind shear is considered severe. If a go-around is possible at a

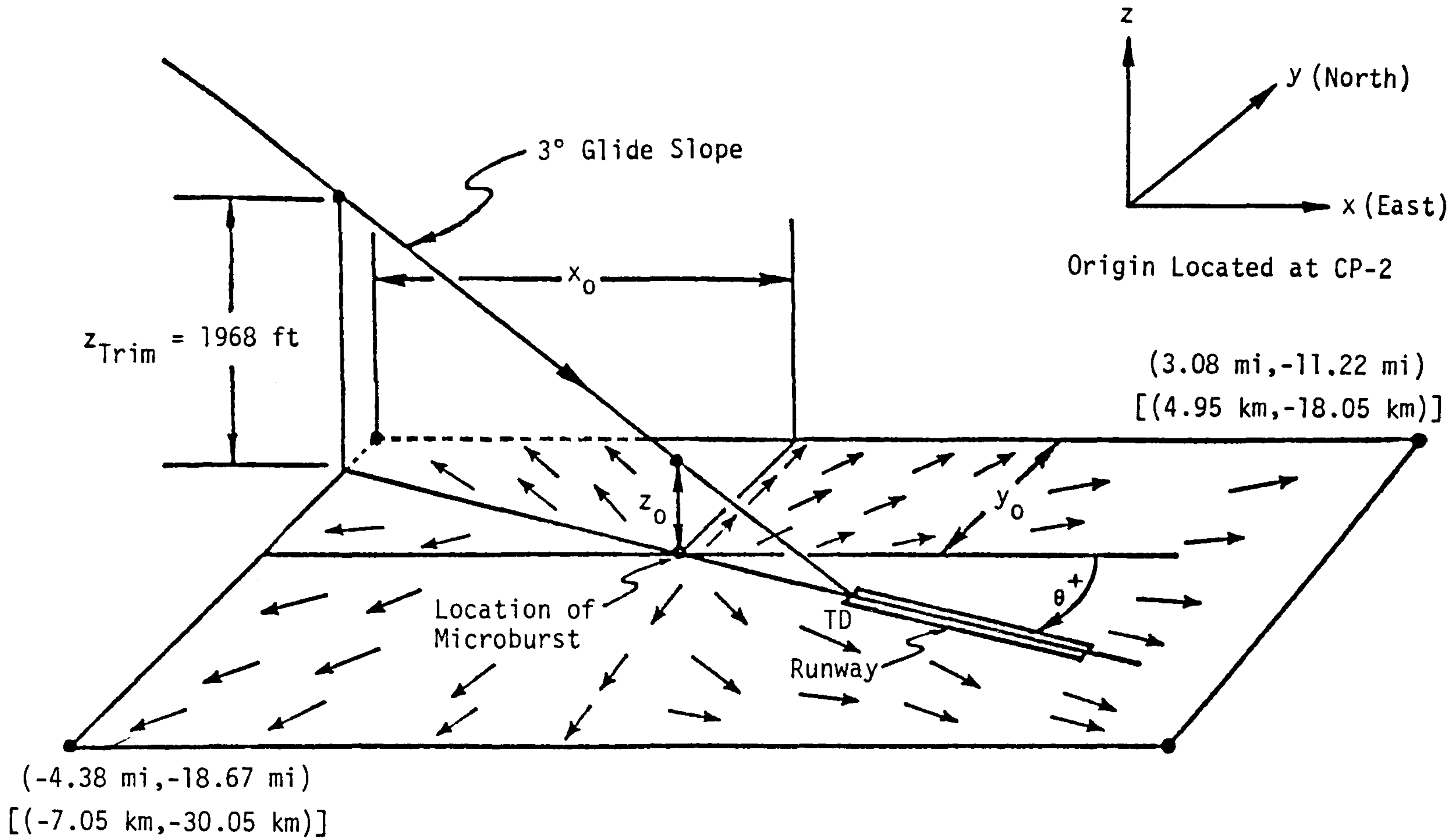

Figure 5.1. Approach path definition and orientation (relative to the full-volume of August 5, 1982, microburst).

pitch angle of 15°, the wind shear is considered moderate. Finally, the wind shear along a given path is considered light if the aircraft does not pass outside the localizer/glide slope during an approach.

Approach Flights

Flights of a B727-200 type aircraft attempting an approach along a 3° glide slope directly along the intended flight paths were computed. The aircraft was trimmed at the 1968-foot (600 m) level. If the airplane remains exactly on the ILS beam, it passes through the center of the microburst located at the position x_0 and y_0 at a height of z_0.

Figure 5.2 shows the computed approach of the aircraft along path $\overline{AB}$ (see Figure 3.3, page 26). In this case, the runway is located such that if the aircraft remains on the glide slope, it passes through the center of the microburst at roughly 300 feet above the ground. The airplane tracks the glide slope reasonably well to an altitude of 300 feet (i.e., at the center of the microburst) but then loses airspeed and sinks rapidly. On losing the ILS, the aircraft is commanded to full thrust and to a pitch angle of 20°; however, because of the severe sinking rate and loss of airspeed (increasing tailwind) so near the ground, it is unable to recover. Figure 5.3 shows a similar situation for an approach along flight path $\overline{CD}$. For this case, the runway is located such that the approach glide slope passes the center of the microburst at a height of 400 feet. The aircraft is observed to drop below the localizer beam at roughly 500 feet altitude prior to encountering the center of the microburst. The aircraft initiates a go-around procedure but encounters a rapidly increasing tailwind and sinking air mass. The airplane, however, survives the increase in tailwind and

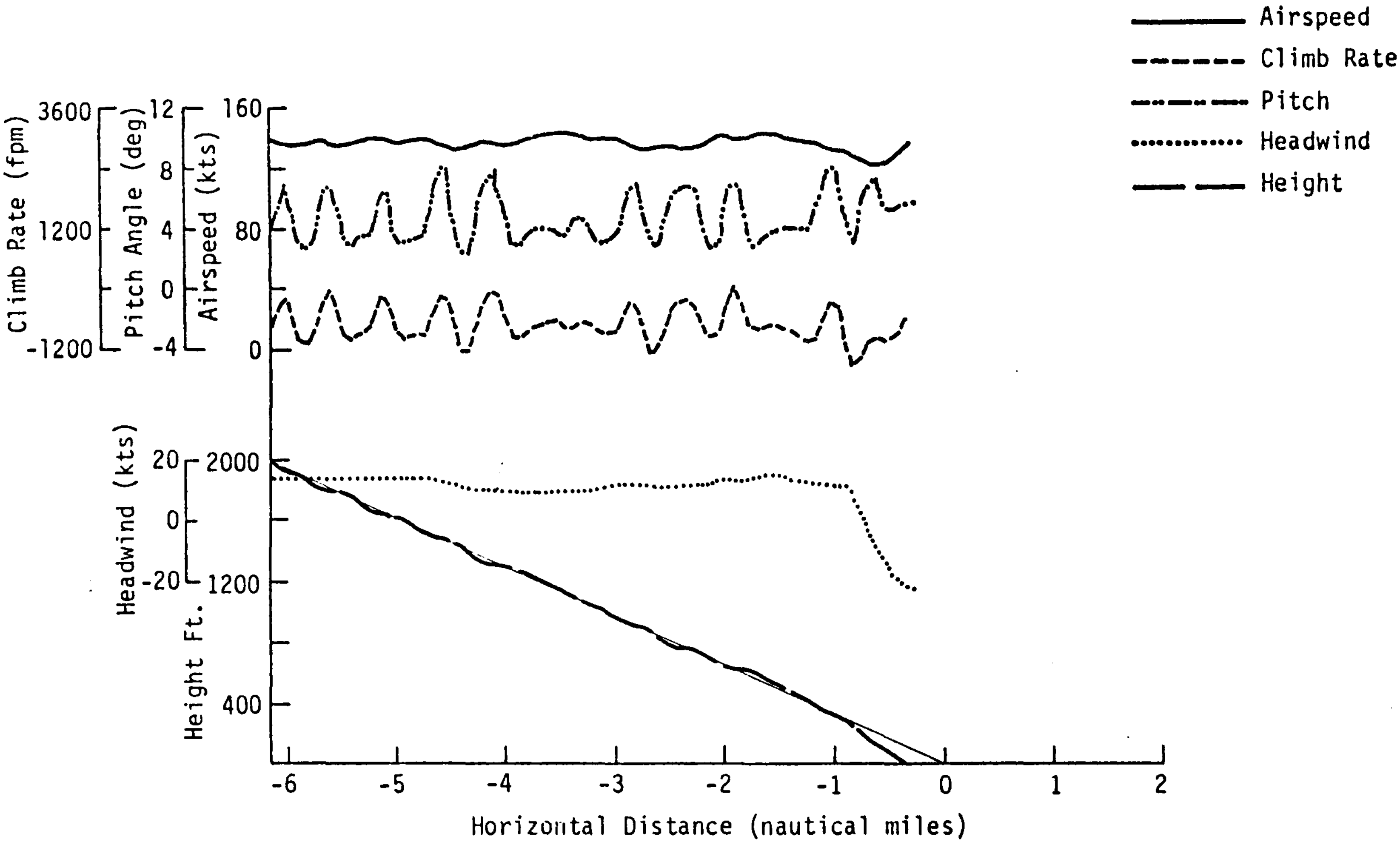

Figure 5.2. Approach along path $\overline{AB}$ (z_o = 300 ft).

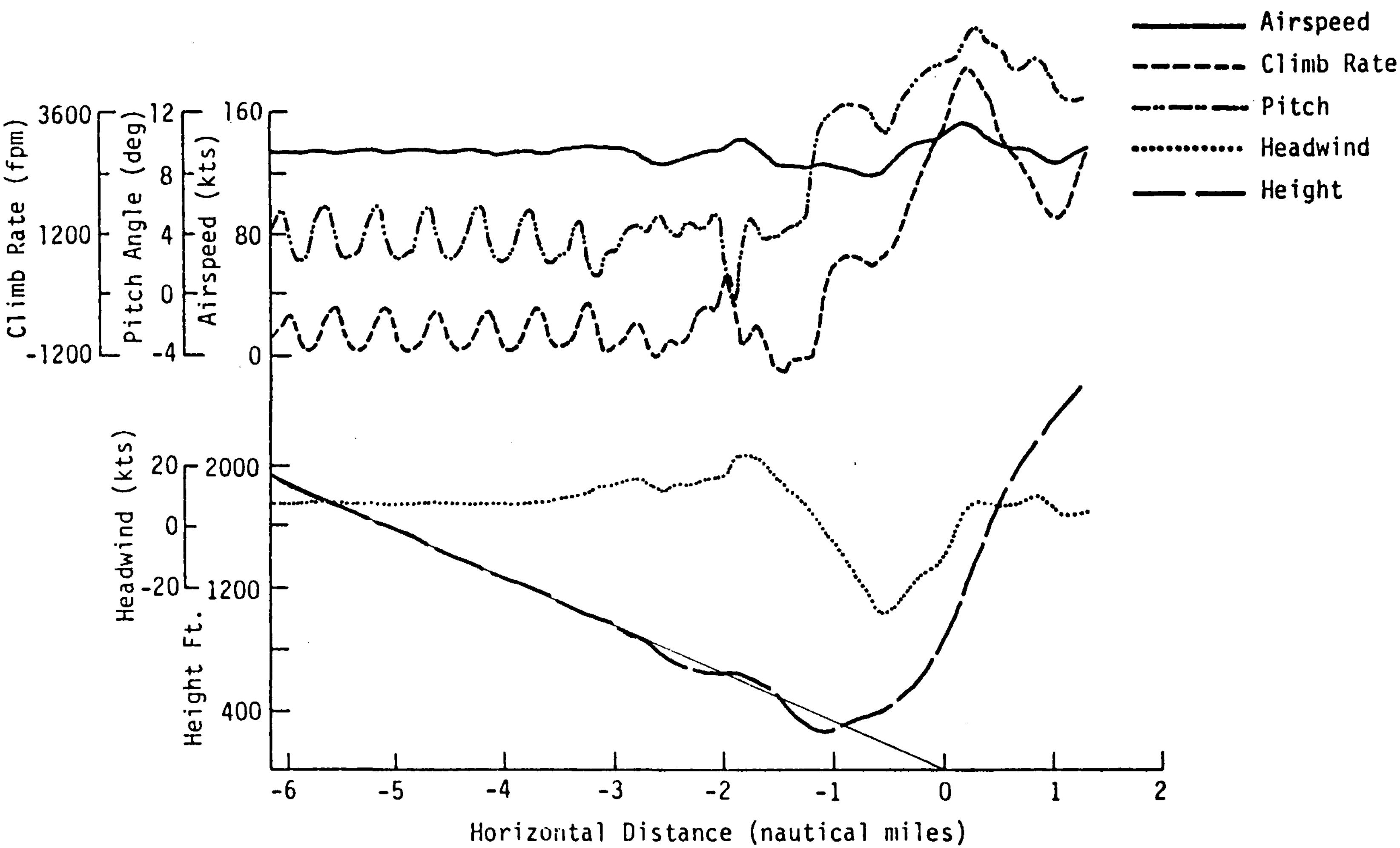

Figure 5.3. Approach along path $\overline{CD}$ (z_o = 400 ft).

climbs out. The significant changes in airspeed and pitch angle of the aircraft are due to the complex wind shear encountered. The pitch angle of the aircraft is converging to the 15° angle commanded at go-around. Many studies, such as those depicted by Figures 5.2 and 5.3 were carried out to classify various profiles through all the full-volume data sets as severe, moderate, and light. Four paths from the 5AU1847 measurement are listed in Table 5.1 as typical wind fields suggested for possible simulator training scenarios.

Takeoff Flights

The location of the center of the microburst is selected relative to an aircraft's liftoff point, in a manner similar to that for the approach (see Figure 5.4). The value of z_0 for takeoff is defined as

TABLE 5.1. Recommended Flight Paths for Approach Landing Simulations.

	x_0	y_0	z_0		
Flight Path	ft × 10^3 [m]	ft × 10^3 [m]	feet [m]	θ (deg)	Classification
$\overline{AB}$	17.2 [5250]	19.2 [5850]	300 [90]	52.7	Severe
$\overline{YZ}$	17.2 [5250]	19.2 [5850]	492 [150]	37.0	Severe
$\overline{CD}$	16.2 [4950]	20.4 [6230]	400 [120]	19.9	Moderate
$\overline{GH}$	13.3 [4050]	25.1 [7650]	0 [0]	52.7	Light

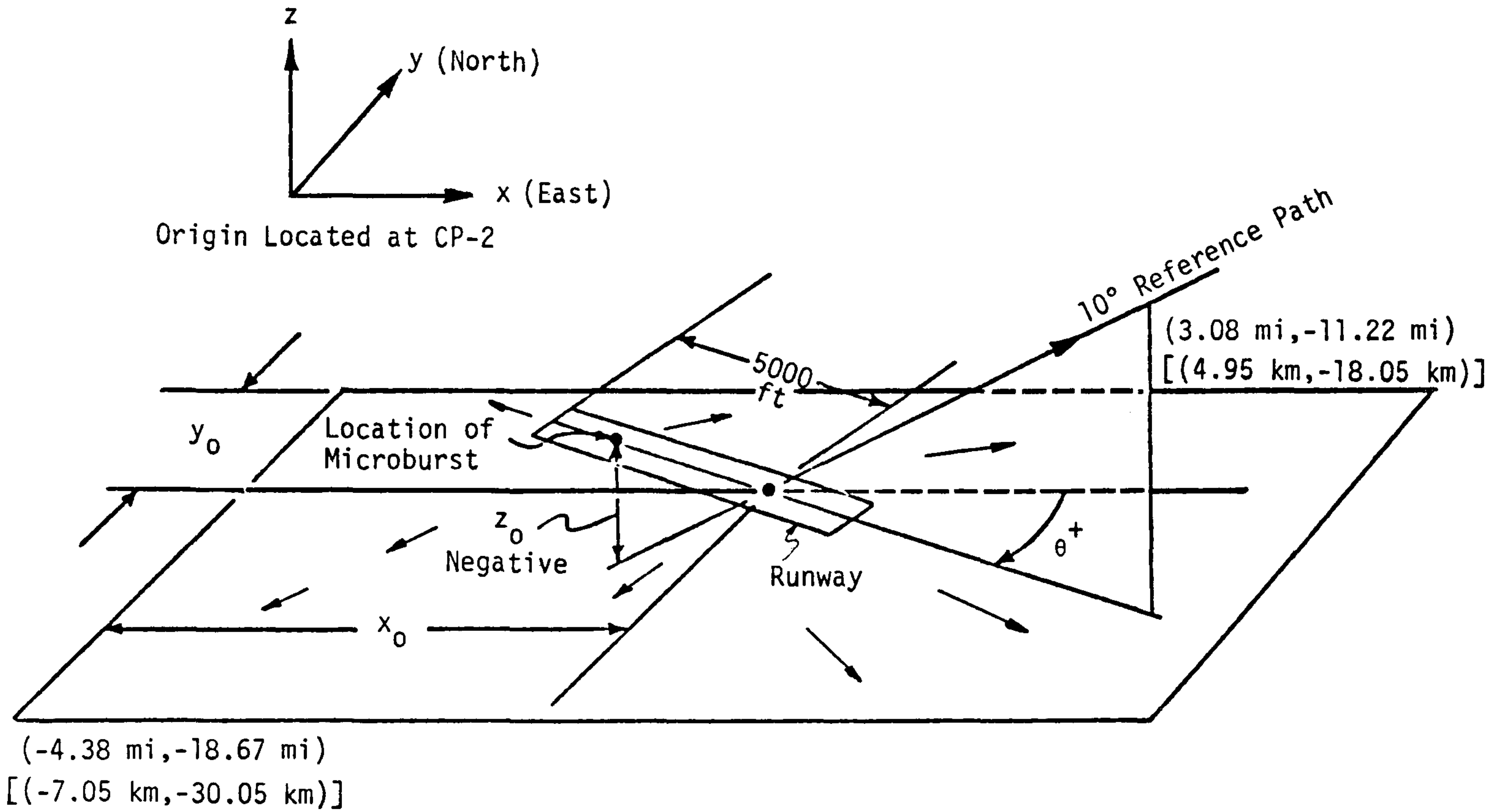

Figure 5.4. Takeoff path definition and orientation (relative to the full-volume of August 5, 1982, microburst).

the height at which the aircraft would pass through the center of the microburst when accelerating along the runway for 5000 feet and then climbing out along a 10° reference path as shown in Figure 5.4. A negative z_0 indicates the aircraft is passing through the center of the microburst (roughly $|z_0|/(\tan 10°)$ from the intended liftoff point) while still on the runway. Note on the approach, the aircraft is trimmed on a 3° glide slope and controlled to maintain that path to the extent possible. For takeoff, however, the 5000-foot ground run with a 10° liftoff path is selected arbitrarily as a reference path to define the position of the microburst to the runway. In actual fact, the B727 type aircraft used in this study would climb out on an approximate 6.4° path if there was zero wind.

For every flight path investigated, the aircraft was able to take off without impacting the ground. However, there were many situations where liftoff was barely achieved and would not have succeeded if obstacles similar to those typically found around an airport were accounted for in the computer simulation. Figure 5.5 is a typical example of takeoff in wind field $\overline{AB}$ (5AU1847 measurement). The dynamic responses of the aircraft flying along path $\overline{AB}$ are plotted in the heavy lines; those of the aircraft flying with zero wind condition are designated in the light lines. The arrows designate the liftoff points of these two cases, respectively. In this case, the center of the microburst is located where the aircraft would pass over a point 66 feet above the ground, approximately 375 feet horizontally from the departure end of the runway, if the aircraft were to climb out along a 10° reference path. In the actual case, the aircraft would more nearly climb out

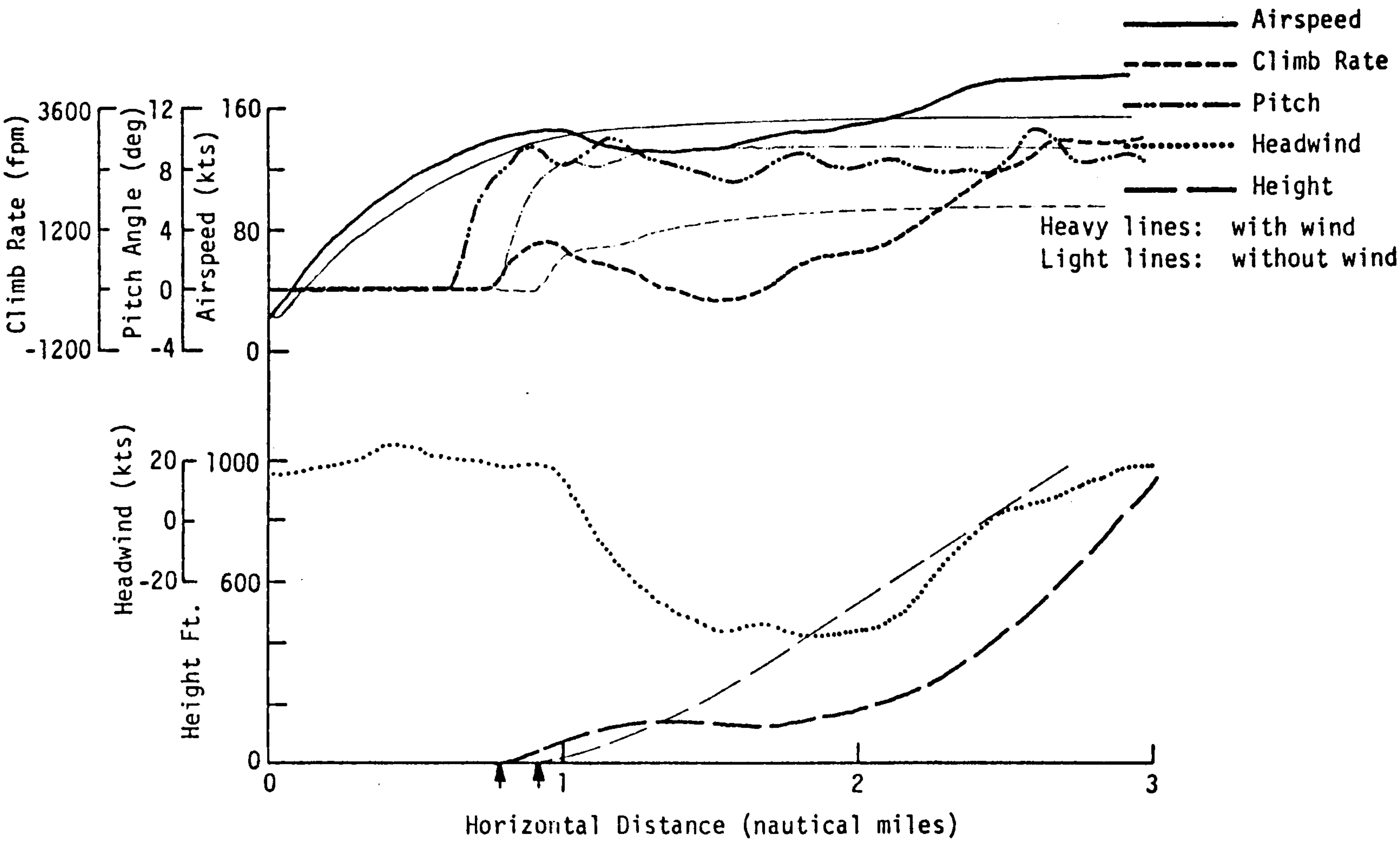

Figure 5.5. Takeoff along path $\overline{AB}$ (z_o = 66 ft).

along a 6.4° path, thus, passing through the microburst at a height of 42 feet. Figure 5.5 shows that the aircraft lifts off and climbs to roughly 150 feet, where it begins to encounter a rapidly increasing tailwind. The aircraft has an insufficient performance margin to maintain altitude and actually sinks to roughly 100 feet above the runway. Although the aircraft is accelerating relative to the ground, it is losing airspeed because the tailwind is increasing at a greater rate. In this case, the aircraft taking off in the wind field $\overline{AB}$ has severe decrease in airspeed and a negative climb rate during the strong tailwind/headwind encountering. Eventually the resultant tailwind decreases and the airplane encounters an increasing headwind which allows it to recover. A constant climb rate does not occur, however, until roughly a full nautical mile from the point of initial liftoff. This wind shear is classified as severe.

Figure 5.6 shows a similar plot for the aircraft's takeoff performance in a less severe wind field. As indicated in the figure, the airplane encounters the effective center of the microburst at about the liftoff point. The aircraft lifts off slightly earlier than that with zero wind condition because of encountering the light headwind on the runway. After liftoff, the aircraft climbs relatively slowly due to the fact that the headwind is decreasing and then the tailwind is increasing. Finally, the aircraft encounters an increasing headwind and resumes a normal climbout. Comparing the flights along path $\overline{AB}$ (Figure 5.5) and along path $\overline{IJ}$ (Figure 5.6), the latter negotiates its wind shear encountering better than the former. The wind shear is not so severe as that along path $\overline{AB}$ and is classified as moderate.

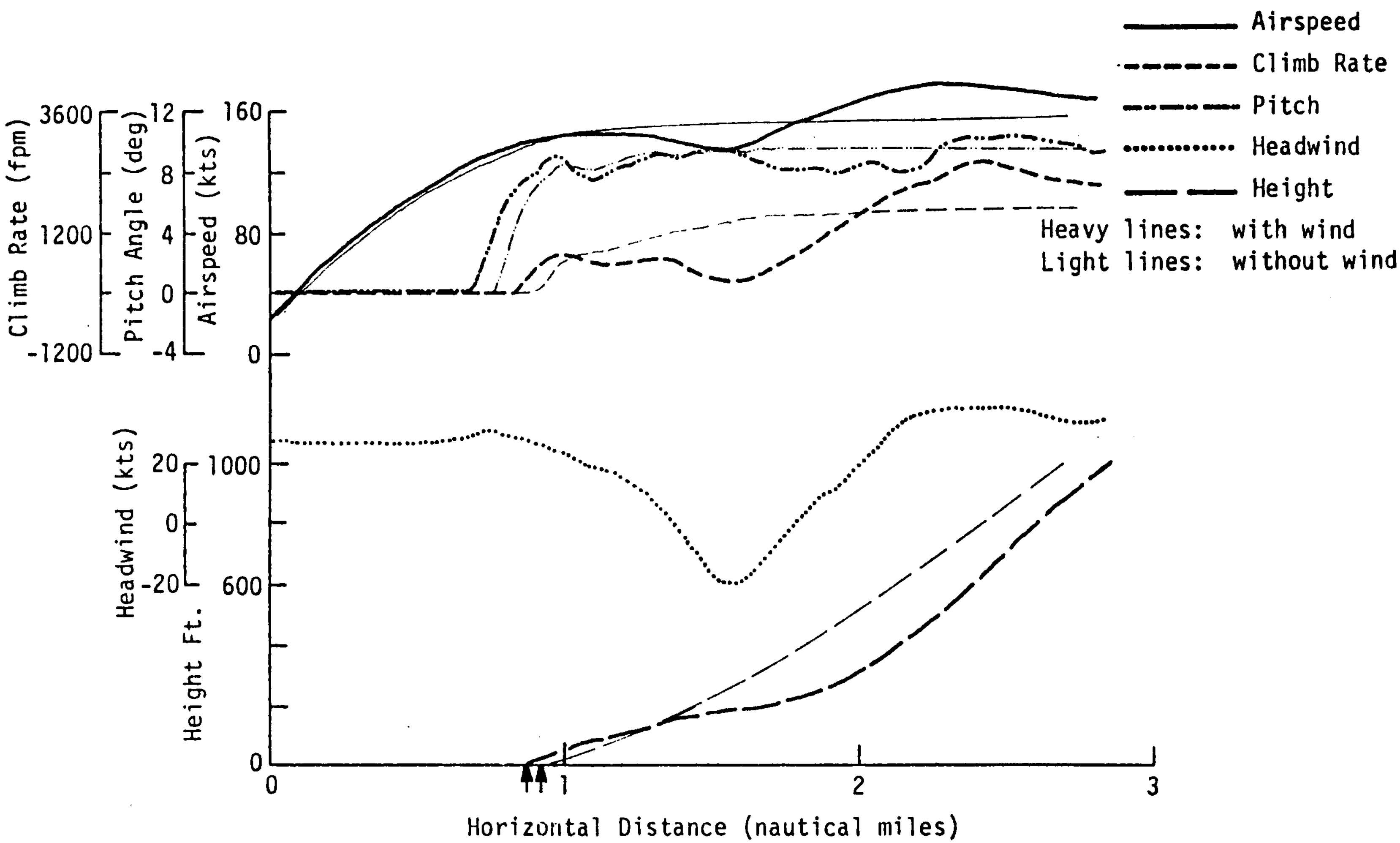

Figure 5.6. Takeoff along path $\overline{IJ}$ (z_0 = - 164 ft).

The location of the microburst relative to the runway is obviously critical to aircraft performance. Figure 5.7 clearly illustrates the effect of the microburst location during takeoff. Three curves are plotted for path $\overline{CD}$ (5AU1847 measurement) where the microburst is encountered at 330 feet, 164 feet, and -33 feet altitudes, respectively, if the aircraft were to climb out along a 10° reference path. Also plotted on the figure is the longitudinal wind speed (headwind +; tailwind -) encountered by the aircraft. In all cases, the aircraft initially takes off with a headwind of slightly more than 20 knots, depending on the relative position of the microburst to the runway, and because of this headwind, the aircraft lifts off relatively quickly. The headwind peaks and then begins to decrease rapidly. In these three paths, a headwind loss of approximately 0.8 knots/100 feet is encountered. The arrows designate the liftoff points for the z_0 = 330 feet, 164 feet, and -33 feet cases, respectively.

When the aircraft encounters the wind shear early in its takeoff roll (z_0 = -33 feet, the dashed line), an extremely long distance is required before flying speed is attained. The aircraft does lift off, however, it climbs out at a slow but steady rate until it exits the microburst. In the case where the aircraft encounters the center of the microburst at approximately 330 feet above the runway after liftoff (along 10° reference path), it climbs out normally to approximately 200 feet altitude and then cannot climb regardless of the fact that takeoff thrust is maintained. The aircraft then begins to sink slightly until it exits the microburst as shown by the upper curves. After exiting the microburst, the aircraft experiences an increasing headwind

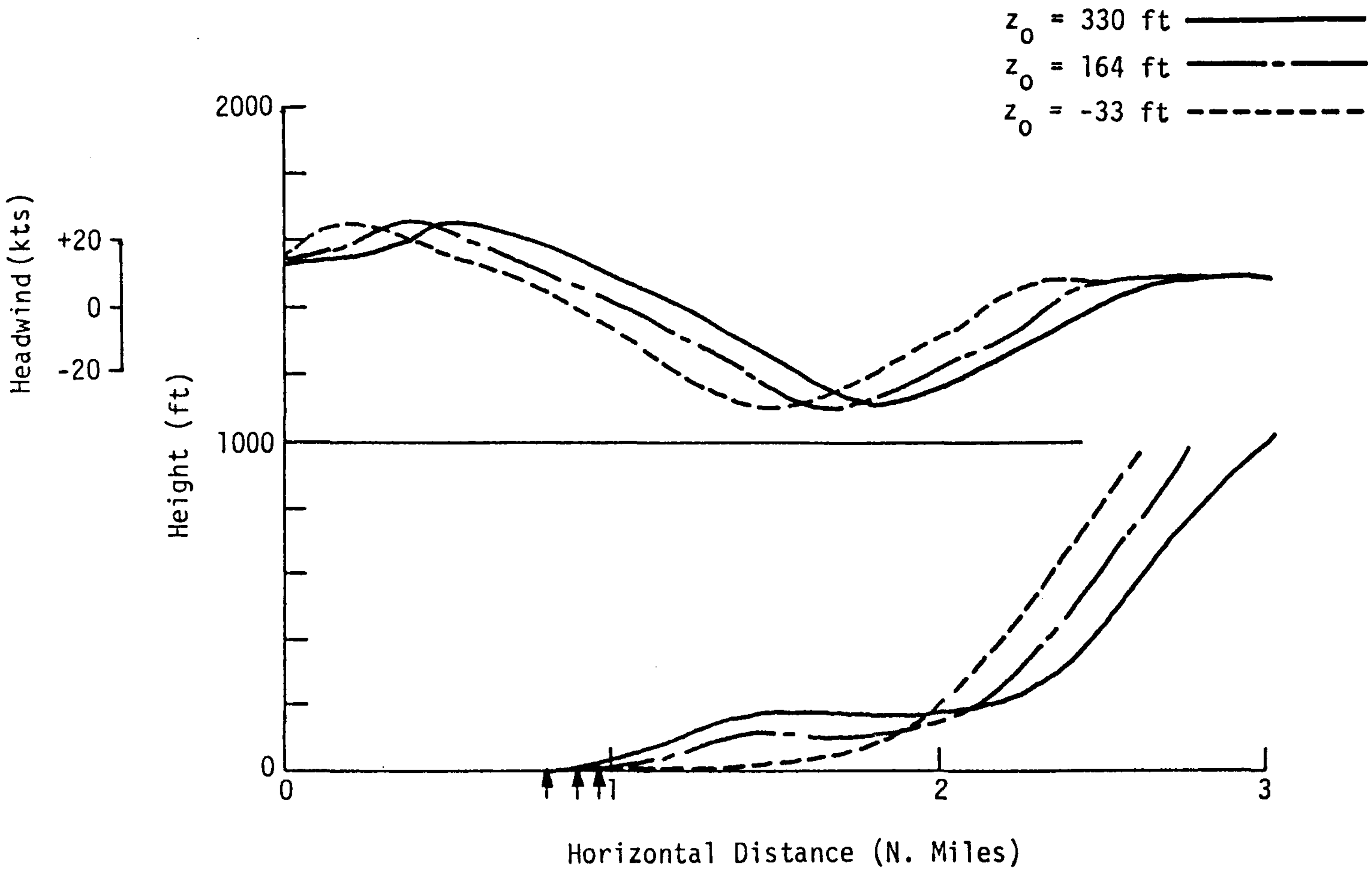

Figure 5.7. Takeoff along path $\overline{CD}$.

and resumes a normal climbout. Therefore, encountering the center of the microburst within ±550 feet of horizontal distance (i.e., z_0 = ±100 feet) relative to the aircraft liftoff point possibly causes great difficulty to the aircraft during its takeoff. Table 5.2 lists paths in the 5AU1847 data set which possibly represent interesting simulator training scenarios.

2. QUANTITATIVE ANALYSES OF WIND SHEAR EFFECT

To quantify the significance of the JAWS wind shear, it is very important to understand how the various wind gradient terms derived in Chapter II affect the aircraft performance and flight characteristics in wind shear encounters. Quantitative and statistical analyses of the effects of the wind speed components and their derivatives on the

TABLE 5.2. Recommended Flight Paths for Takeoff Simulations.

	x_0	y_0	z_0		
Flight Path	ft × 10^3 [m]	ft × 10^3 [m]	feet [m]	θ (deg)	Classification
$\overline{AB}$	17.2 [5250]	19.2 [5850]	66 [20]	52.7	Severe
$\overline{CD}$	16.2 [4950]	20.4 [6230]	-164 [-50]	19.9	Severe
$\overline{IJ}$	19.2 [5850]	14.3 [4350]	-164 [-50]	32.3	Moderate
$\overline{KL}$	17.2 [5250]	24.1 [7350]	492 [150]	30.0	Light

aircraft's flight conditions at ILS CAT II window are carried out in this section.

First, the deviation of the flight path from the decision height window for different position of the microburst to the runway is investigated. A dimensional parameter, N_S, expressed in terms of three variables along the aircraft's trajectory is then defined and calculated for over 40 simulations. Finally, the effects of the wind gradient terms along the aircraft's trajectory are studied by conducting several simulated flights through the microburst cell in a wagon-wheel-spoke pattern of a chosen JAWS data set as indicated in the latter part of this section. The standard deviations (SD) of the various aircraft's aerodynamic parameters and of the wind gradients encountered along the path within the microburst cell are calculated for several approach flights through the center of the cell at a specified height.

Decision Height Window

The current FAA definition of a successful ILS CAT II approach is given in Advisory Circular No. 120-20 (issued June 6, 1966). The criteria is expressed in terms of maximum acceptable airplane flight path deviations at an altitude of 100 feet above the runway as shown in Figure 5.8. The reference glide path goes through the geometric center of the decision height window which has the dimensions, ΔZ = 24 feet and ΔY = 150 feet, in the vertical and lateral directions, respectively. Determination of the ILS CAT II decision height window requirements are reported in Johnson and Hoh (1972). The influence of wind shear on an aircraft during approach can be quantified by comparing the trajectory

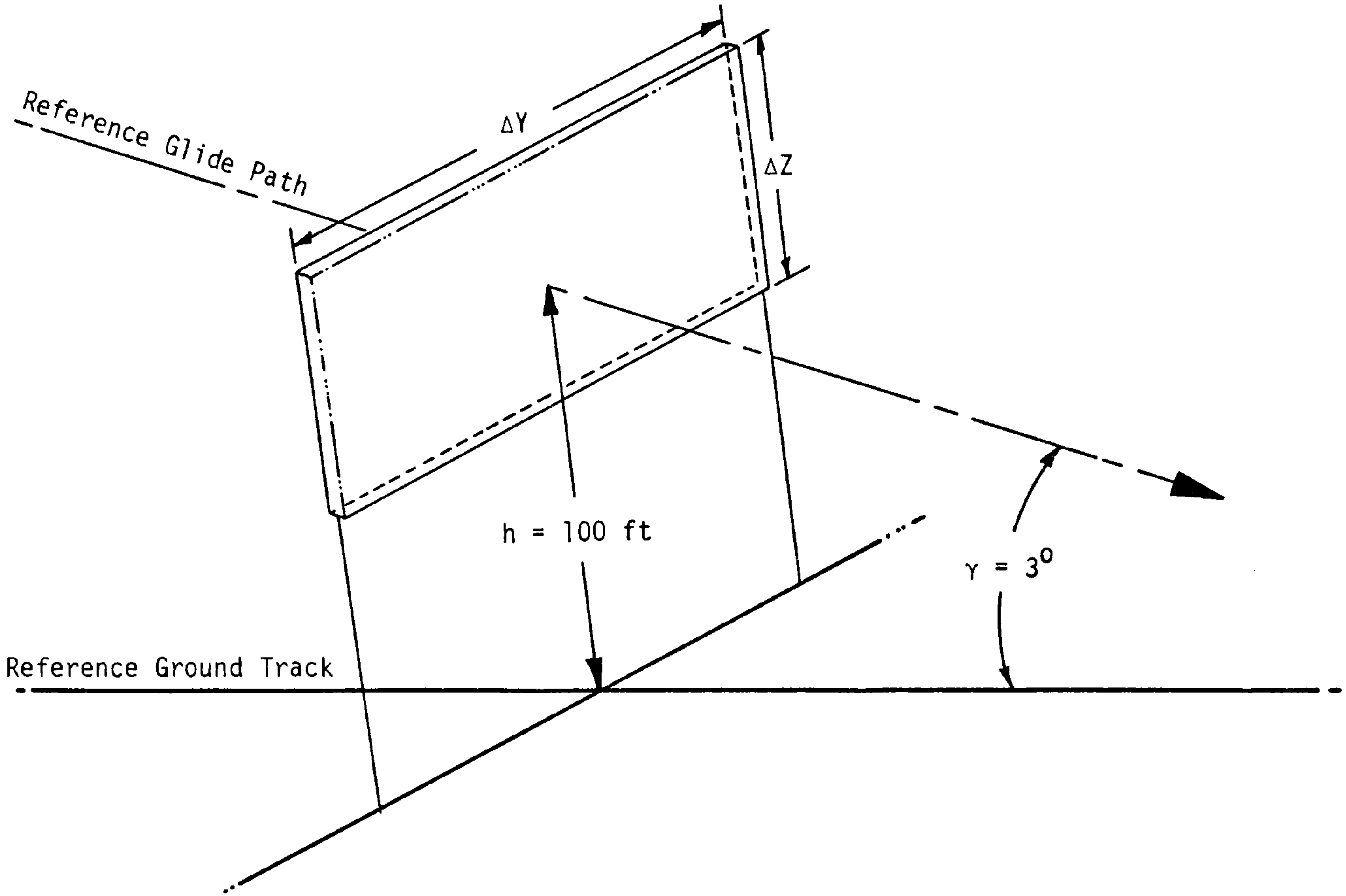

Figure 5.8. Recommended CAT II window, ΔZ = 24 feet, ΔY = 150 feet.

deviations from the reference glide path relative to the longitudinal and lateral decision windows.

The influence of the position of the center of the microburst relative to the glide slope on airplane response is studied by computing several airplane trajectories through the microburst with the center located at different positions from the threshold of the runway. Figure 5.9 illustrates the intended flight paths along $\overline{CD}$ (5AU1847) microburst. A physical concept of these 11 paths is that the center of the microburst is moving along $\overline{CD}$ from right to left relative to the runway. Aircraft are approaching at separation distances of approximately 3000 feet. Thus, each aircraft would encounter the center of the microburst at different heights above the ground. In the figure the center of the microburst is roughly at 17,500 feet. The solid circle marked CM in Figure 5.9 is the effective microburst center for the specific path. The horizontal distance is measured from the entry point of the JAWS data set along path $\overline{CD}$. The circled number shown on each path represents the flight path number. Flight paths 1 through 3 do not pass through the center of the microburst; path 4 encounters it right at the touchdown point, and the other paths traverse the center at various heights. In terms of the nomenclature in Figure 5.1, page 56, the aircraft flies through the microburst center at heights of z_0 (-492 feet, -328 feet, ... 984 feet, 1148 feet). Negative z_0 means that the intended flight path touches down before reaching the microburst center.

The longitudinal decision height window is defined as a rectangular area shown in Figure 5.10. Abscissa ΔU_{100}, and ordinate ΔZ_{100}, represent the airspeed perturbation and vertical deviation of the aircraft at the

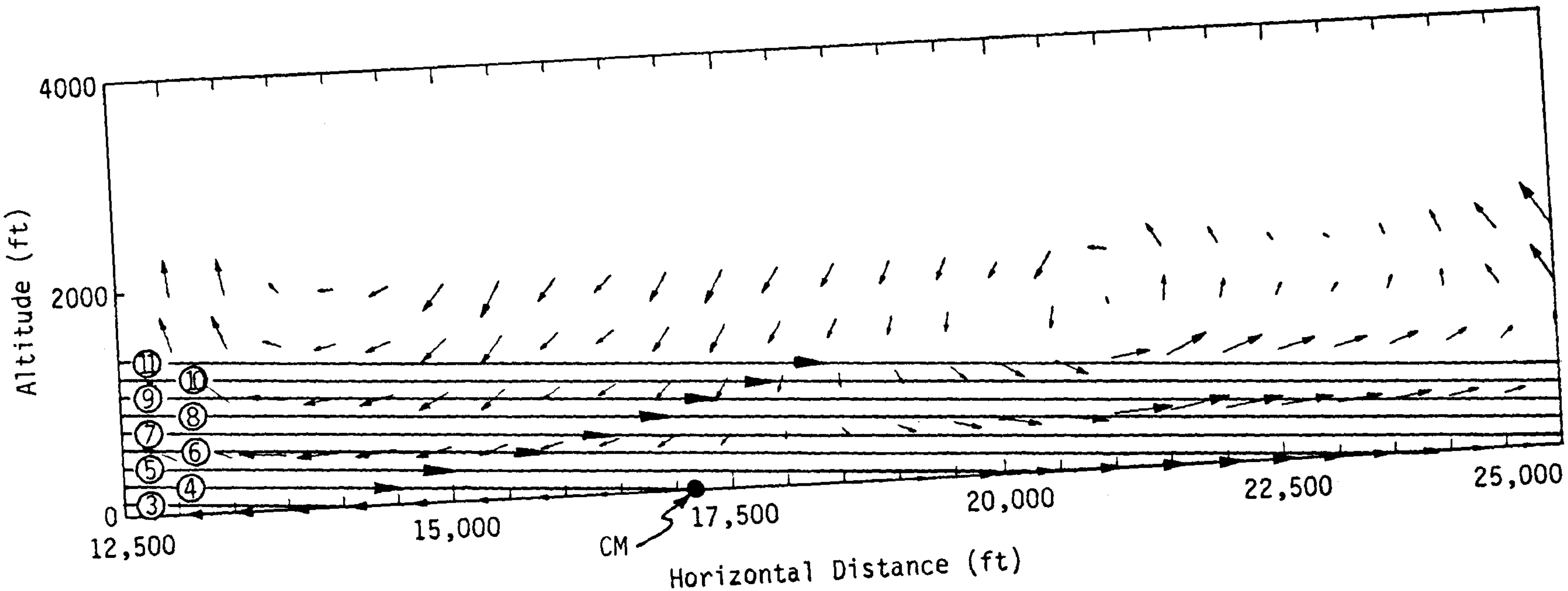

Figure 5.9. Relation of microburst wind field to the 11 intended flight paths along $\overline{CD}$ for which aircraft trajectories are computed. (Circled numbers shown on each path represent the flight path number.)

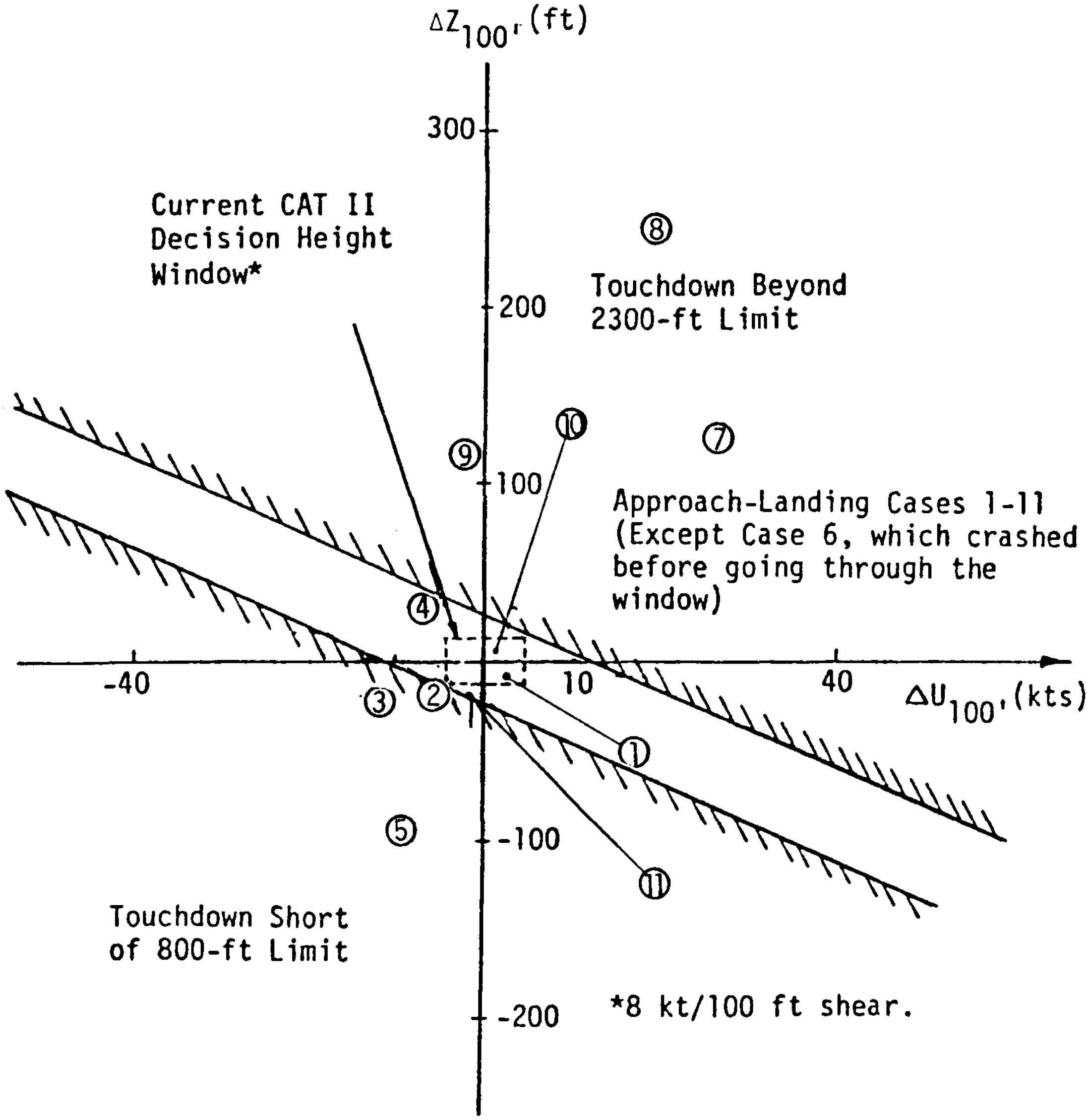

Figure 5.10. Computed flight conditions at longitudinal decision height window, CAT II approach criteria ($\overline{CD}$). (Circled numbers designate aircraft conditions for that flight path number.)

CAT II window from the trim airspeed and glide slope beam, respectively. Based on the aircraft flight conditions at the CAT II window and the wind conditions to be encountered by the aircraft from the decision height to the ground, one can predict the touchdown position of the aircraft on the runway (Johnson and Hoh, 1972). The FAA requires a total dispersion of the main gear touchdown point to be less than 1500 feet about a nominal point. For 8 knots/100 feet wind shear, the parallel lines in Figure 5.10 represent that the aircraft touches down at 2300 feet (headwind shear) and 800 feet (tailwind shear) measured from the threshold of the runway along its centerline. The acceptable touchdown region is confined to the two parallel boundary lines. Similarly, the corresponding lateral decision height window is defined by the abscissa $\Delta Y_{100'}$, lateral deviation, and ordinate $\Delta V_{100'}$, lateral deviation rate (see Figure 5.11).

Figures 5.10 and 5.11 show the distribution of trajectories of a B727 type aircraft at the longitudinal and lateral decision height window, respectively, for the 11 flights along path $\overline{CD}$. All flights go through lateral decision height window safely. However, flight numbers 5 through 9 with z_0 from 164 feet to 820 feet experience serious deviations from the intended glide slope and airspeed at the longitudinal decision height window. Therefore, the trajectories and longitudinal wind components of flights 5 through 11 are shown in Figure 5.12. By inspecting Figures 5.10 through 5.12 one sees that wind shear influences the airplane severely in the longitudinal direction and only slightly in the lateral direction. Inspection of Figure 5.9 shows flights 5 through 9 encounter significant tailwind and rotational velocity of the wind field after they pass the microburst center. However, flights 10 and 11

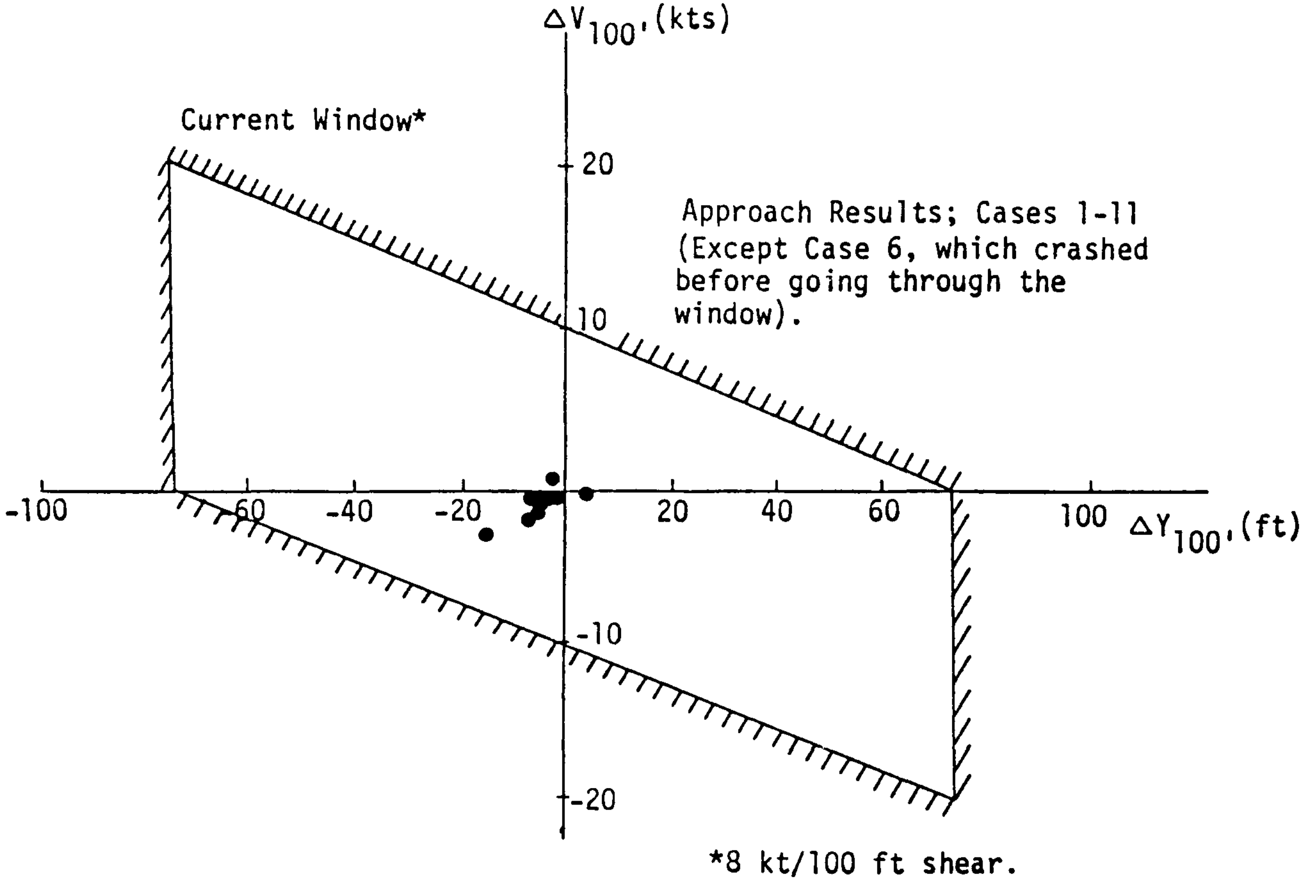

Figure 5.11. Computed flight conditions at lateral decision height window, CAT II approach criteria ($\overline{CD}$).

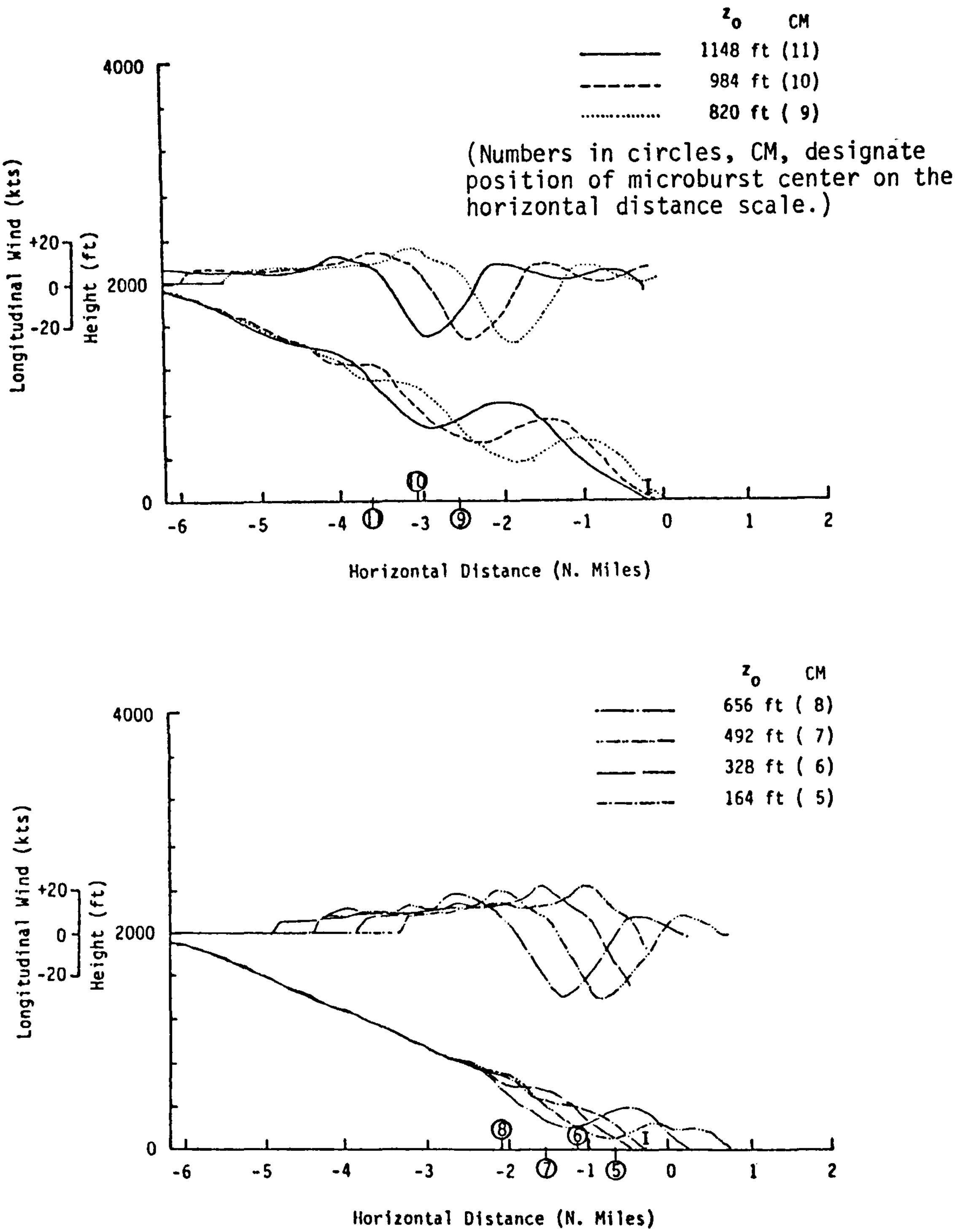

Figure 5.12. Flight path approach trajectories and longitudinal wind speed component along flight path $\overline{CD}$ for seven flights (flight path 5 through 11).

escape most of the microburst effects by flying through it at a higher level (≥984 feet). Figures 5.13 through 5.16 show the same analyses for path $\overline{AB}$. Similar results are obtained.

Parametric Study of Aircraft Performance Relative to CAT II Window

As mentioned in Frost and Bowles (1984), there is clearly a lack of agreement and understanding on the correct form of the wind shear terms in the governing equations of aircraft motion (derived in Chapter II, Section 1) and as to the magnitude of their effect. Five cases, which are distinguished by assessing the magnitudes of the wind gradient terms with various models and the magnitudes of the time derivatives of angle of attack, α, and sideslip angle, β, are defined and studied in this section. Also, a dimensional parameter, N_S, which is first defined by Frost et al. (1983), is adopted to test its degree of correlation with the trajectory deviation of an aircraft at the CAT II decision height window.

The technique of computing the wind gradient terms, the derivatives of angle of attack and sideslip angle, and the relative rate of angular rotation, influences directly the calculation of the aerodynamic coefficients and also straightforward affect the the dynamic response of an aircraft. Fives cases are listed in Table 5.3. Case A, which is used throughout the study and is taken as the reference case, is considered as the most correct and complete system of equations. For case A we interpolate directly the wind gradient terms from JAWS three-dimensional data base, incorporate the rotation effect of the wind field (Equation 2.17) into the calculation of aerodynamic coefficients and compute the $\dot{\alpha}$ and $\dot{\beta}$ with Equation 2.13.

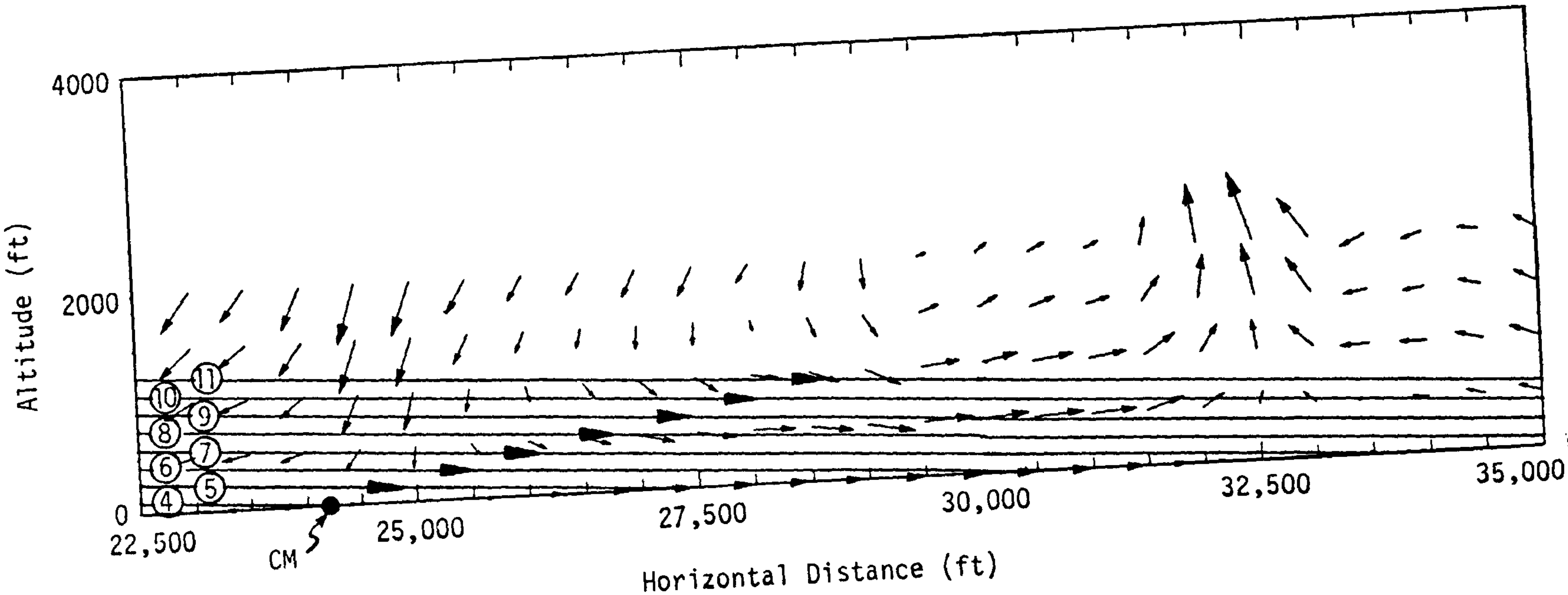

Figure 5.13. Relation of microburst wind field to the 11 intended flight paths along $\overline{AB}$ for which aircraft trajectories are computed. (Circled numbers shown on each path represents the flight path number.)

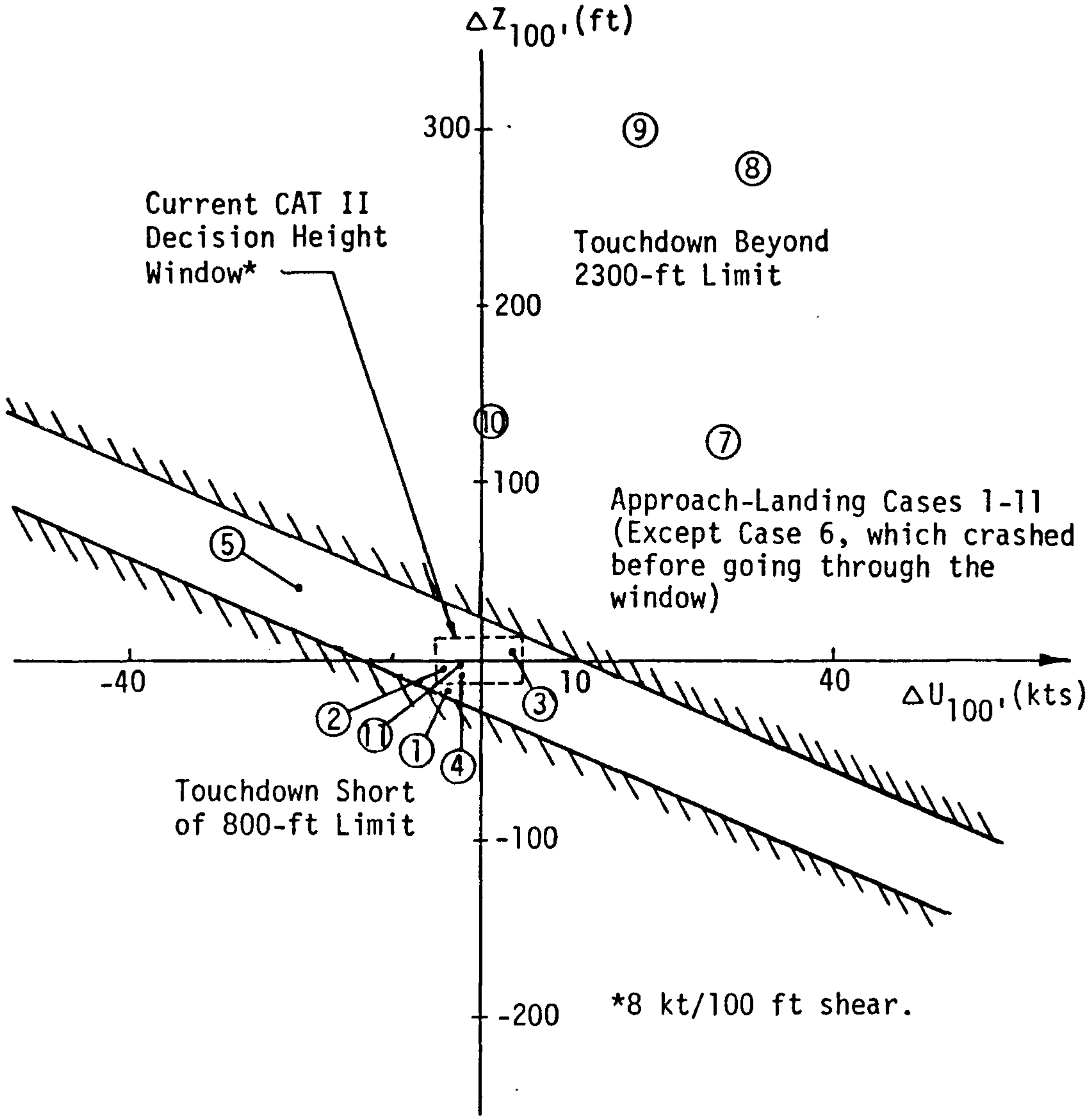

Figure 5.14. Computed flight conditions at longitudinal decision height window, CAT II approach criteria ($\overline{AB}$). (Circled numbers designate aircraft conditions for that flight path number.)

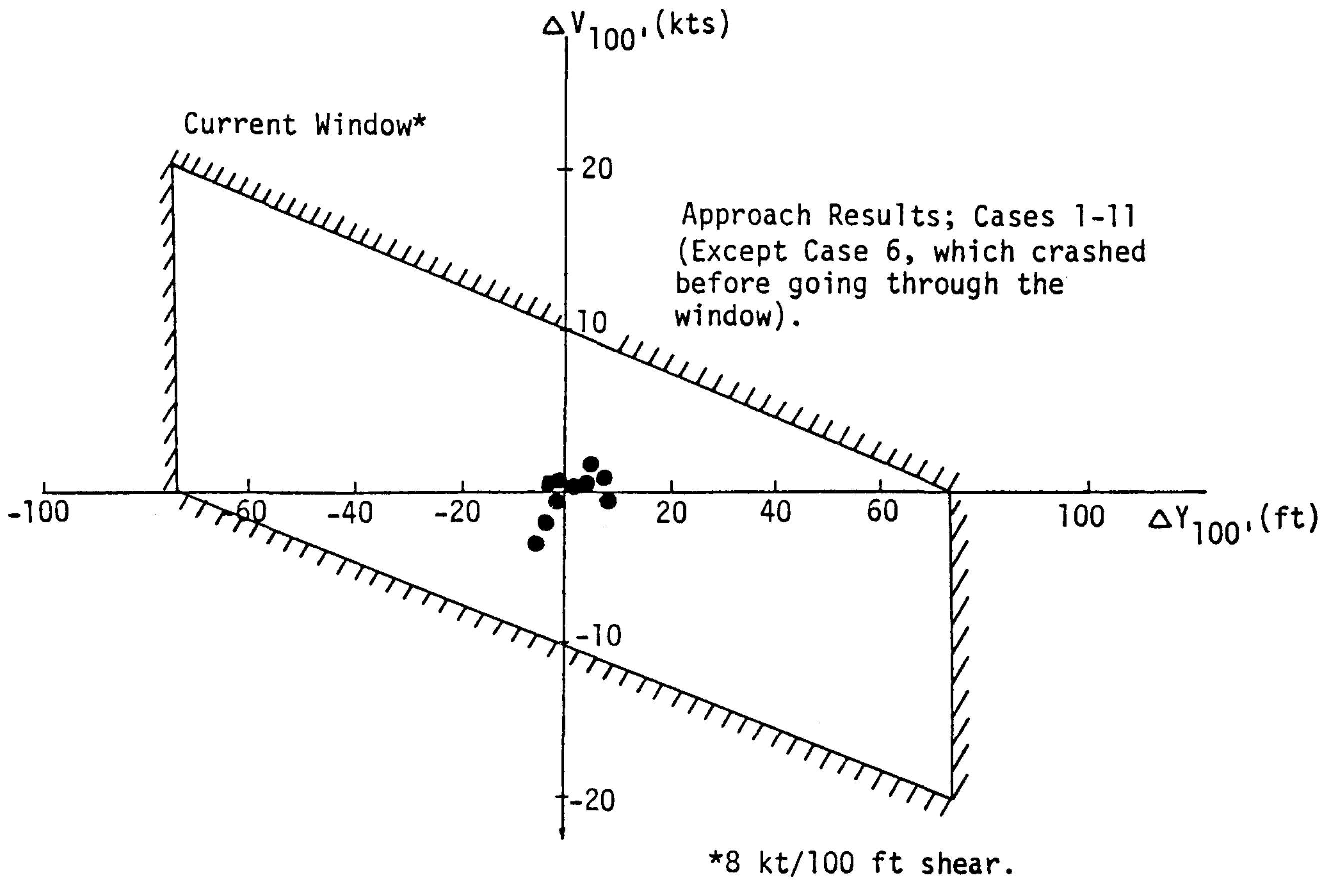

Figure 5.15. Computed flight conditions at lateral decision height window, CAT II approach criteria ($\overline{AB}$).

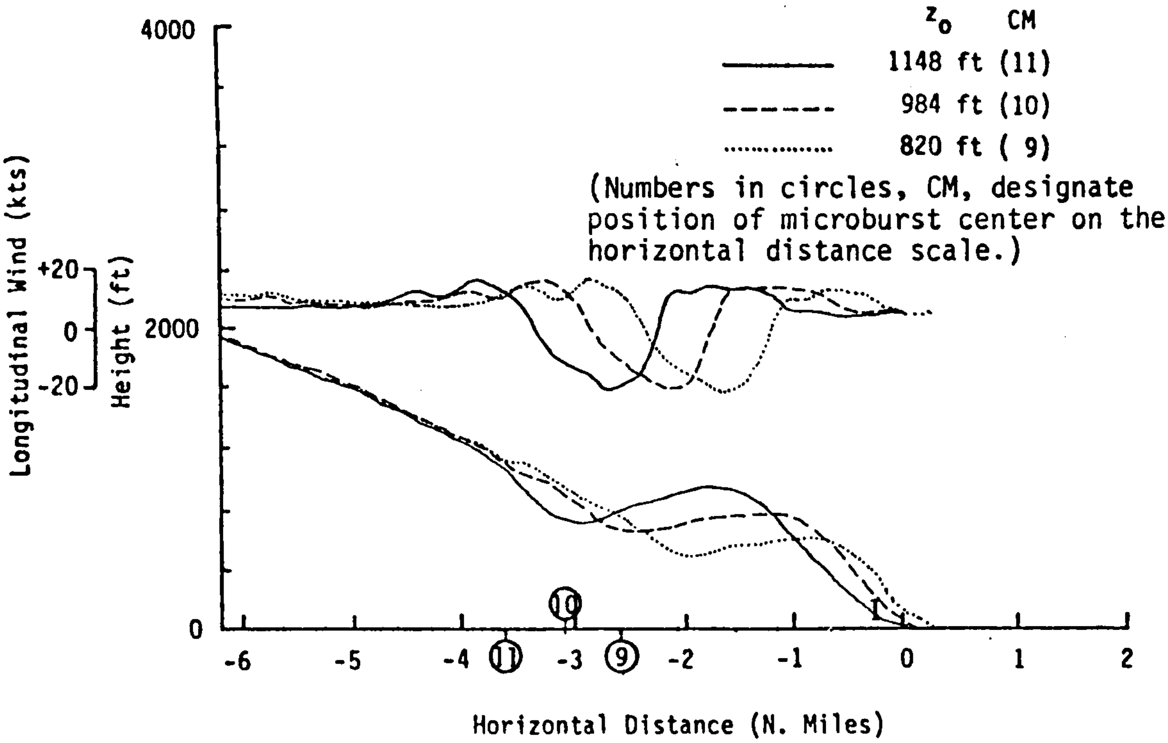

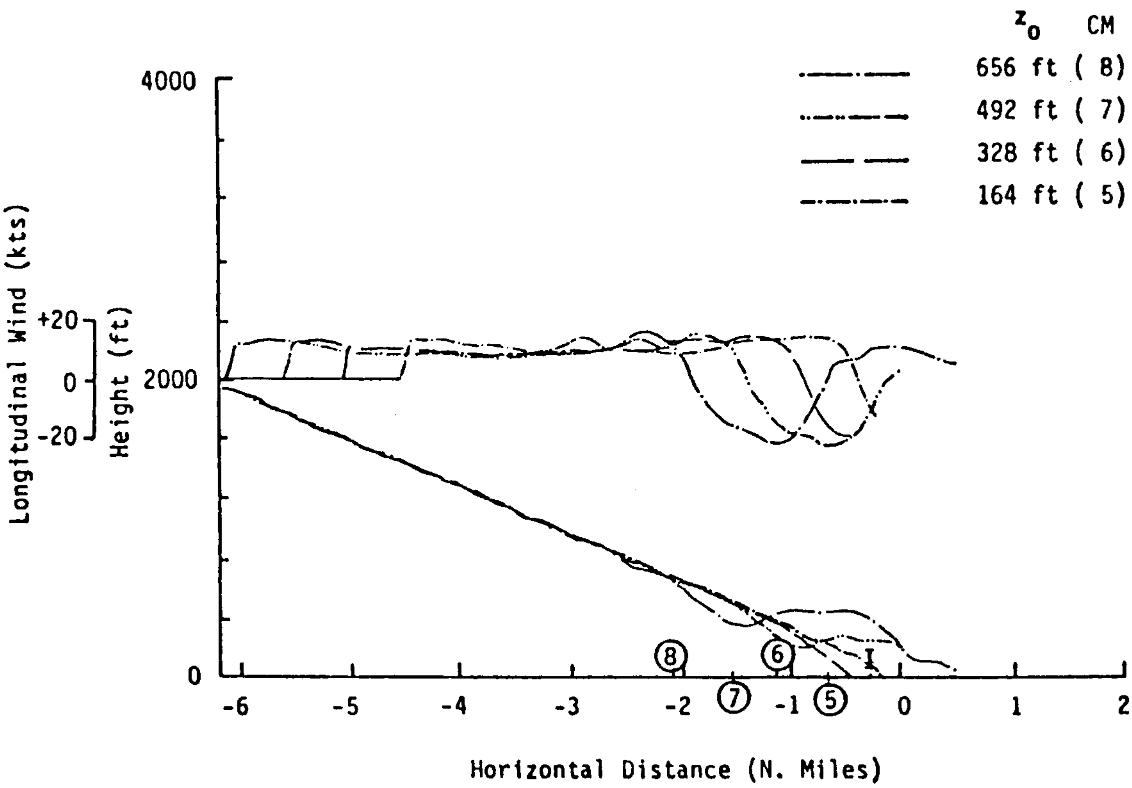

Figure 5.16. Flight path approach trajectories and longitudinal wind speed component along flight path $\overline{AB}$ for seven flights (flight path numbers 5 through 11).

TABLE 5.3. Various Considerations of Wind Shear Effect With Five Case Studies.

Case A (Reference Case):

- Interpolate derivatives
- Compute relative rotations
- Three-dimensional wind fields

Case B:

- Finite difference derivatives
- Compute relative rotations (interpolate spatial derivatives)
- Three-dimensional wind fields

Case C:

- Interpolate derivatives
- Neglect relative rotations
- Three-dimensional wind fields

Case D:

- Interpolate derivatives
- Compute relative rotations
- Two-dimensional wind fields (neglect $\Delta W_{XE}/\Delta Y_E$, $\Delta W_{YE}/\Delta Y_E$, and $\Delta W_{ZE}/\Delta Y_E$

Case E:

- Neglect all derivatives
- Neglect relative rotations
- Three-dimensional wind fields

Case B is basically the same as case A except the total derivatives of the wind components and the derivatives of angle of attack and sideslip angle are calculated by backward-difference technique. That is, the derivative terms, $\dot{W}_X$, $\dot{W}_Y$, $\dot{W}_Z$, $\dot{\alpha}$, and $\dot{\beta}$ in Equations 2.13 and 2.14 are evaluated by dividing the difference in value at the last time step (TS) and at current time step with the time interval Δt:

$$\dot{W}_X = \frac{W_{X_{\text{Current TS}}} - W_{X_{\text{Last TS}}}}{\Delta t}$$

$$\dot{W}_Y = \frac{W_{Y_{\text{Current TS}}} - W_{Y_{\text{Last TS}}}}{\Delta t}$$

$$\dot{W}_Z = \frac{W_{Z_{\text{Current TS}}} - W_{Z_{\text{Last TS}}}}{\Delta t} \qquad (5.1)$$

$$\dot{\alpha} = \frac{\alpha_{\text{Current TS}} - \alpha_{\text{Last TS}}}{\Delta t}$$

$$\dot{\beta} = \frac{\beta_{\text{Current TS}} - \beta_{\text{Last TS}}}{\Delta t}$$

Case C is also similar to case A except the rotation effects of the wind field are ignored. Case D uses the same approach to evaluate all derivatives as case A but the wind field in this case is two-dimensional. The two-dimensional wind field still consists of three wind speed components at each grid point but there is no variation in the winds in the lateral direction (i.e., the value of the wind shear terms $\partial W_{XE}/\partial Y_E$, $\partial W_{YE}/\partial Y_E$, and $\partial W_{ZE}/\partial Y_E$ are zero).

Finally, case E is defined as the case which may occur if the existing simulator equations of motion are not carefully corrected for variable winds. It is expected that many simulators and computer programs do not incorporate the wind gradient terms, which are derived in Chapter II, into the equations of aircraft motion. Because the wind is considered zero or constant, i.e., $\dot{u}$, $\dot{w}$, and $\dot{v}$ in body coordinates are the same as the inertial value and no distinction is made. However, the force equations in body coordinates (Equation 2.2) is correctly expressed as:

$$X - mg \sin \theta = m\dot{u}_E + m(qw_E - rv_E)$$

$$Y + mg \cos \theta \sin \phi = m\dot{v}_E + m(ru_E - pw_E) \qquad (5.2)$$

$$Z + mg \cos \theta \cos \phi = m\dot{w}_E + m(pv_E - qu_E)$$

where u_E, v_E, and w_E are inertial velocity components of the vehicle in the body axes. These cannot be directly used in computing aerodynamic coefficients as is possible for zero wind. Moreover, one cannot compute the derivatives of angle of attack, α, and sideslip angle, β, by using $\dot{u}$, $\dot{v}$, and $\dot{w}$ directly in Equation 2.13. Since this may often happen in existing computational programs, $\dot{\alpha}$ and $\dot{\beta}$ are calculated for case E by:

$$\dot{\alpha} = \frac{u\dot{w}_E - w\dot{u}_E}{u^2 - w^2}$$

$$\dot{\beta} = \frac{\dot{v}_E(u^2 + w^2) - v(u\dot{u}_E + w\dot{w}_E)}{V^2\sqrt{u^2 + w^2}} \qquad (5.3)$$

where $\dot{u}_E$, $\dot{v}_E$, and $\dot{w}_E$ are obtained from Equation 5.3; the wind gradient terms do not enter the calculations of $\dot{\alpha}$ and $\dot{\beta}$. Also, most previous computer codes do not include the rotational velocity of the wind field itself, which contains wind gradient terms. For that reason, in case E Equation 2.17 is simplified as:

$$\begin{Bmatrix} p_{rel} \\ q_{rel} \\ r_{rel} \end{Bmatrix} = \begin{Bmatrix} p \\ q \\ r \end{Bmatrix} \qquad (5.4)$$

Thus, case E does not consider the effect of any wind gradient term, although it includes the influence of the wind speed components of the wind field.

An in-depth investigation of the influence of the wing gradient terms on the aircraft dynamic response is carried out by comparing trajectories computed with a system of equations based on the five cases of different assumptions described above. Over 40 simulations are carried out using the JAWS wind shear data. These simulations are flights along the intended paths $\overline{AB}$, $\overline{CD}$, $\overline{YZ}$, and $\overline{IJ}$ (see Figure 3.3, page 26) and through the effective microburst center of each intended path at different heights. Recall that the flight conditions $\Delta Z_{100'}$, $\Delta U_{100'}$, $\Delta Y_{100'}$, and $\Delta V_{100'}$ of an aircraft at CAT II decision height window are very important in predicting the touchdown position on the runway. Comparing the flight conditions for the CAT II decision height window is an indication of the significance due to the five different case studies. The mean values and the standard deviations of the flight conditions for the reference case relative to trimmed flight with zero wind condition are given in Table 5.4. Also, the mean value and the standard deviations of the difference of the flight conditions at decision height window of cases B through E relative to the reference case are tabulated in Table 5.5.

Case B has significant deviations from the reference case although it saves about 20 percent computer time to obtain all derivatives as

TABLE 5.4. Statistical Analyses of Flight Conditions of Reference Case at CAT II Window.

	Reference Case			
	$\Delta Z_{100'}$ (ft)	$\Delta U_{100'}$ (kt)	$\Delta Y_{100'}$ (ft)	$\Delta V_{100'}$ (kt)
Mean	42.1	3.11	-0.16	-0.38
Standard Deviation	111.77	12.32	4.87	1.33

Equation 5.1. In this case, standard deviations of the calculated vertical deviation, $\Delta Z_{100'}$, and lateral deviation, $\Delta Y_{100'}$, show over 25 and 85 percent errors relative to the reference case, respectively. Ignoring the rotation effect of the wind field, case C, and neglecting the effect of the wind shear terms in lateral direction, case D, also have slight errors on the flight conditions of an aircraft at CAT II window. Finally, case E, which does not contain any wind gradient term, has over 10 percent errors relative to the reference case.

The significant features of wind along the flight path which have the most pronounced influence on flight path deterioration are of interest for a number of reasons (Frost et al., 1983). A dimensional parameter, which is defined as

$$N_S = \frac{W_Z}{Z} \frac{\partial W_X}{\partial X}$$

in terms of the three variables, W_Z, Z, and $\partial W_X/\partial X$, was calculated along the flight path of over 40 simulations to see if these represented the key variables. The simulations use the reference case, case A.

TABLE 5.5. Statistical Analyses of Flight Conditions at CAT II Window for Five Case Studies.

	$\Delta Z_{100'}$ (ft)	$\Delta U_{100'}$ (kt)	$\Delta Y_{100'}$ (ft)	$\Delta V_{100'}$ (kt)
	(Backward Differencing, ω_r) - (Reference Case)			
Mean Value	-3.22	0.338	0.85	0.16
Standard Deviation	29.43	3.67	4.26	1.1
	(Interpolation, No ω_r) - (Reference Case)			
Mean Value	-0.97	0.117	-0.18	-0.231
Standard Deviation	7.79	0.666	3.96	1.75
	(Two-Dimensional Wind, ω_r) - (Reference Case)			
Mean Value	-1.03	0.017	-0.14	0.017
Standard Deviation	10.9	1.12	2.88	0.821
	(No Wind Gradient, No ω_r) - (Reference Case)			
Mean Value	-3.35	0.95	0.14	-0.69
Standard Deviation	11.16	7.37	1.7	2.36

W_Z and $\partial W_X/\partial X$ are the downdraft and the tailwind shear (or headwind shear) encountered by the aircraft; z is the height above the runway. The logic of this parameter, N_S, is that the $\partial W_X/\partial X$, Z, and W_Z appear to be the most significant variables influencing the aircraft in wind shear. $\partial W_X/\partial X$ mainly induced by the tailwind (or headwind) in the longitudinal direction multiplied by $\dot{X}_E$ acts as an effective force and is the largest of the wind gradient terms. The variable Z appears because the hazard increases as the height of encounter decreases. Finally, W_Z is a measure of the rate at which the air mass sinks and hence pulls the aircraft down. Therefore, the magnitude of $|N_S|$ along the aircraft trajectory is a possible indicator of flight deterioration during approach. From the initial position of the aircraft (height of 1968 feet) to the CAT II decision height window, the ratio of the time period in which the aircraft has a value of $|N_S|$ larger than a given value to total time of approach was computed from:

$$\text{TR (Time Ratio)} = \frac{\text{n (Number of time steps which have } N_S \text{ larger than given value)}}{\text{N (Number of total time steps of the specific flight)}}$$

The absolute values of N_S for the over 40 simulations all fall within a range of 0.0 s^{-2} to 0.0015 s^{-2}. The time ratios, which have $|N_S|$ values larger than 0.00005 s^{-2} and 0.0001 s^{-2}, are plotted versus the deviation of the aircraft's trajectory from the glide path at the CAT II window in Figures 5.17 and 5.18, respectively. Two simulations crashed before going through the window are also extrapolated to the CAT II Window. A parabola-like curve which is an eyeball best fit of the data points is shown on the figure. Both figures shows that the

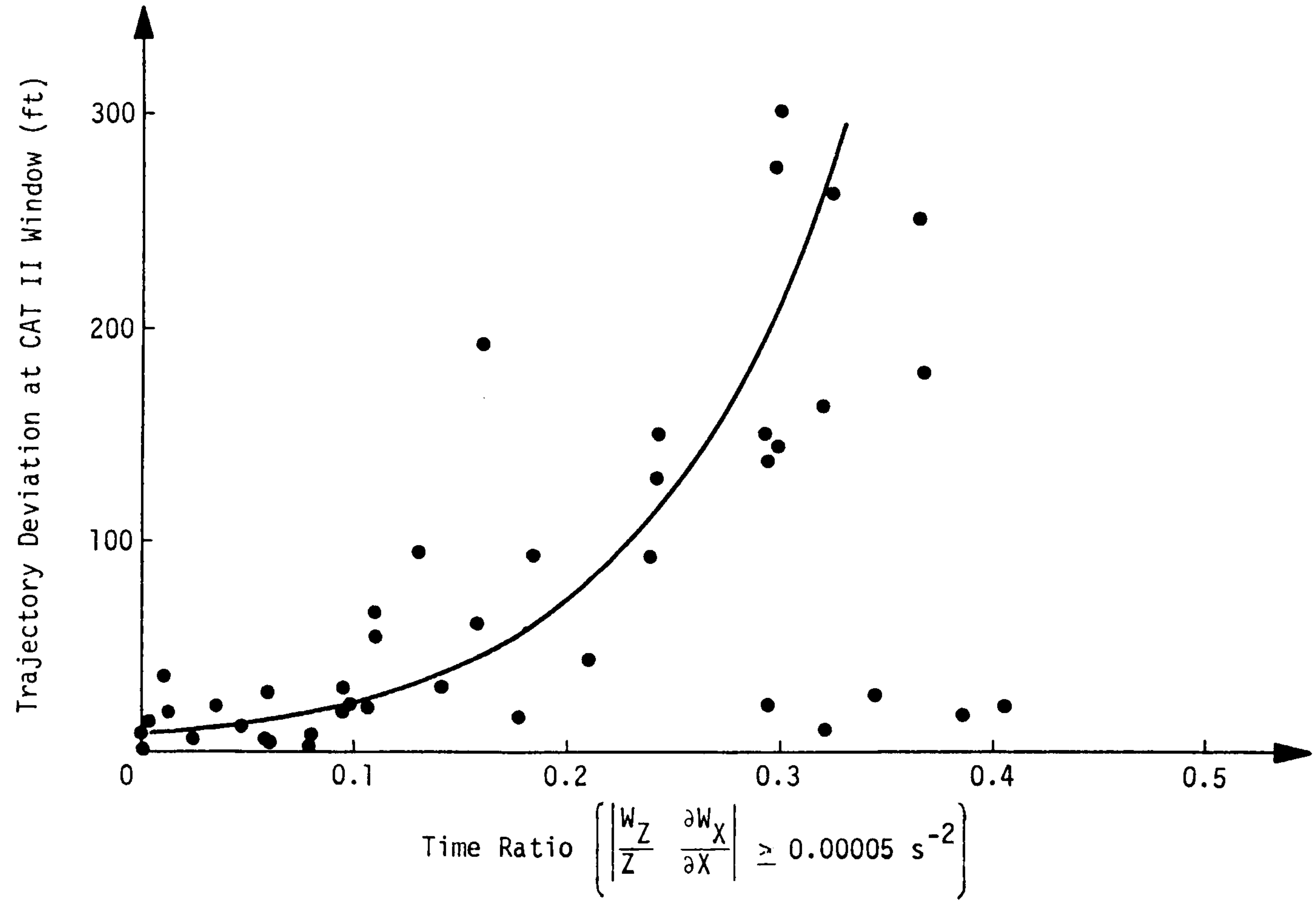

Figure 5.17. Trajectory deviation of a B727-200 type aircraft at CAT II window relative to the time ratio of $|N_S| \geq 0.00005 \ s^{-2}$.

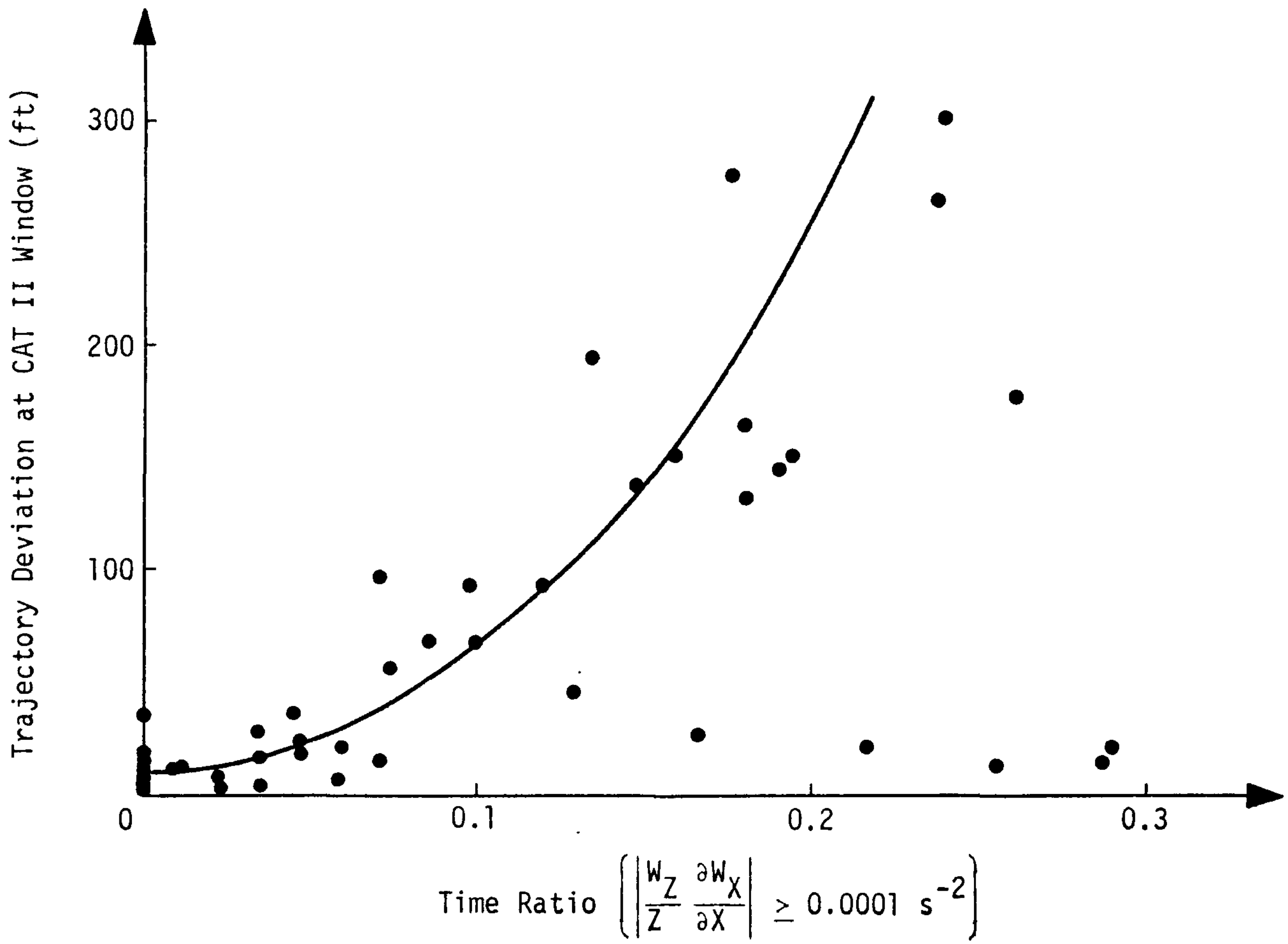

Figure 5.18. Trajectory deviation of a B727-200 type aircraft at CAT II window relative to the time ratio of $|N_S| \geq 0.0001\ s^{-2}$.

trajectory deviation at the CAT II window has a nonlinear variation with the time ratios of the corresponding simulations. Also, the figures show that the higher time ratio an aircraft's simulation has for $|N_S|$ larger than a certain value along its flight path, the larger trajectory deviation it has at the CAT II window.

Figure 5.17 shows that all flight trajectories for which have $|N_S| \geq 0.00005\ s^{-2}$ less than 10 percent of the time of approach deviate only slightly from the glide path at the CAT II window. However, a few flights encountering the wind shear parameter $|N_S| \geq 0.00005\ s^{-2}$ for over 30 percent of the time of approach still go through the window with only slight trajectory deviation. The reason is that all of these specific simulations intend to fly high enough through the center of the microburst ($\geq$984 feet). Therefore, the aircraft has sufficient performance to recover itself from the wind shear effect although it encounters the significant wind shear parameter (N_S) for over 30 percent of the time of its approach. Similar results are achieved in Figure 5.18 for the flights having $|N_S| \geq 0.0001\ s^{-2}$.

Further Analysis of the Effects of Wind Gradient Terms

In Section 2, the effects of the wind gradient terms (derived in Chapter II) in $\dot{\alpha}$ and $\dot{\beta}$ and in the rotation of the wind field itself were investigated in terms of their influence on the flight conditions of an aircraft at the CAT II window. Further analysis of the effect of these terms on the aerodynamic response of an aircraft along its trajectory within a given microburst cell is carried out in this subsection. Using Equations 5.2, 5.3, and 5.4, the simulations do not consider the effect of any wind gradient term associated with the adopted wind shear data set. Quantitatively comparing the aircraft's dynamic performance of the simulations with and without the wind gradient terms, one can quantify the effect of these terms along the aircraft's trajectory.

Figures 5.19 and 5.20 show the dynamic performance of a B727-200 type aircraft flying along path $\overline{AB}$ without and with the effect of the wind gradient terms, respectively. If the aircraft remained on the intended approach path, it would encounter the wind speed components shown in Figure 5.21. The actual wind speed components encountered by the simulations corresponding to Figures 5.19 and 5.20 are very close to those shown in Figure 5.21. The intended flight paths of the two simulations pass through the microburst center at a height of 820 feet. Comparison of the two figures shows that the influence of the wind gradient terms associated with the specific wind field on the aircraft performance is slight.

A typical range gate probed by a Doppler radar is about 492 feet, which is larger than the magnitudes of an airplane. The values are then interpolated to a rectangular grid spacing of approximately 492 x 492 x 820 feet. Winds subsequently interpolated from the JAWS data set for use in the aircraft performance computes simulation thus neglect turbulence fluctuations of scales less than approximately 820 feet. As Frost (1984) and Campbell (1984) point out, high-frequency turbulence should be superimposed on the JAWS data. The local high-frequency atmospheric turbulence can induce random gradients in the wind field which are higher than those contained in quasi-mean wind speeds of the JAWS data. To simply multiply the wind speed components at each grid point by a factor

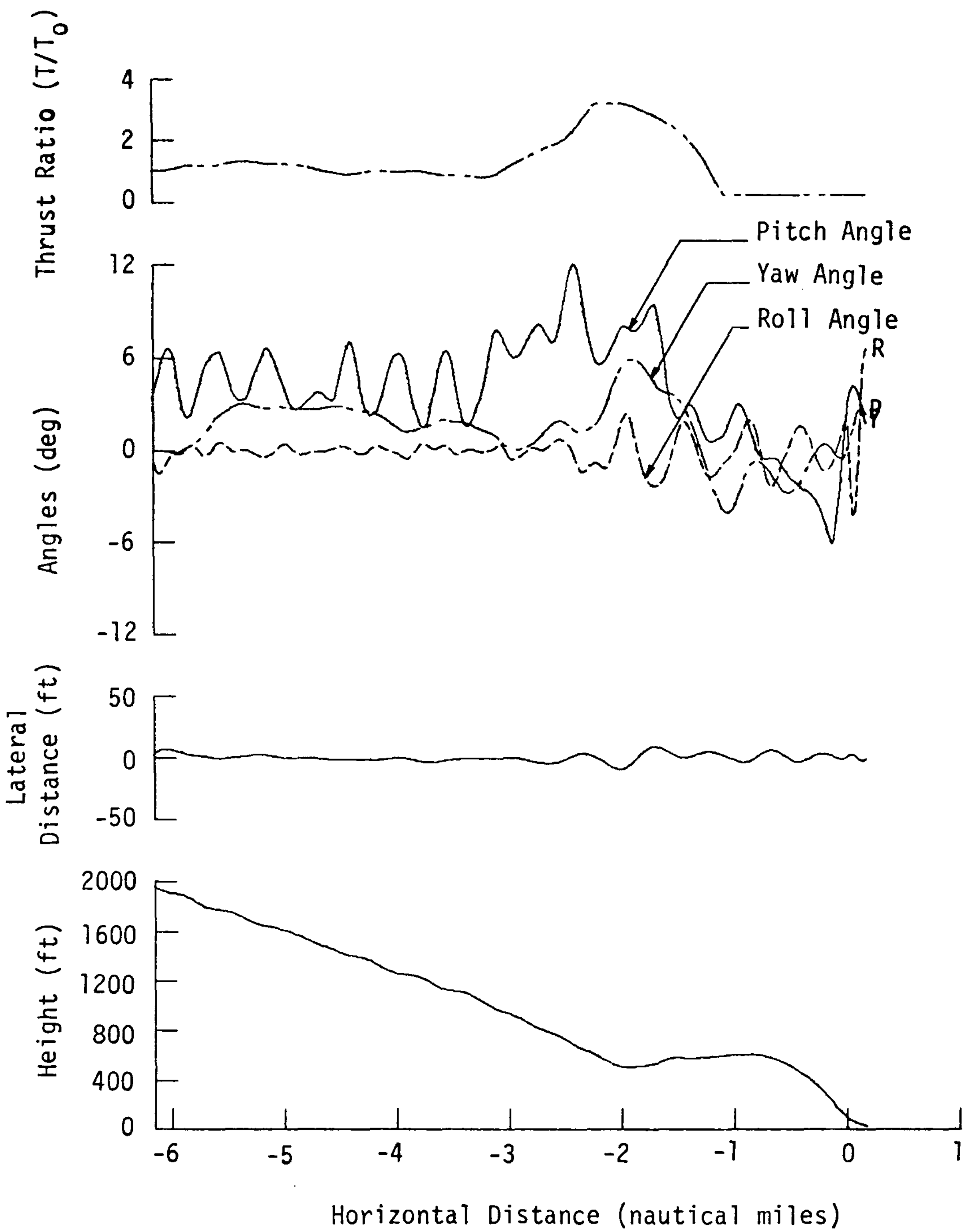

Figure 5.19. Dynamic performance of a B727-200 type aircraft flying along path $\overline{AB}$ without considering the effects of the wind gradient terms (z_0 = 820 ft).

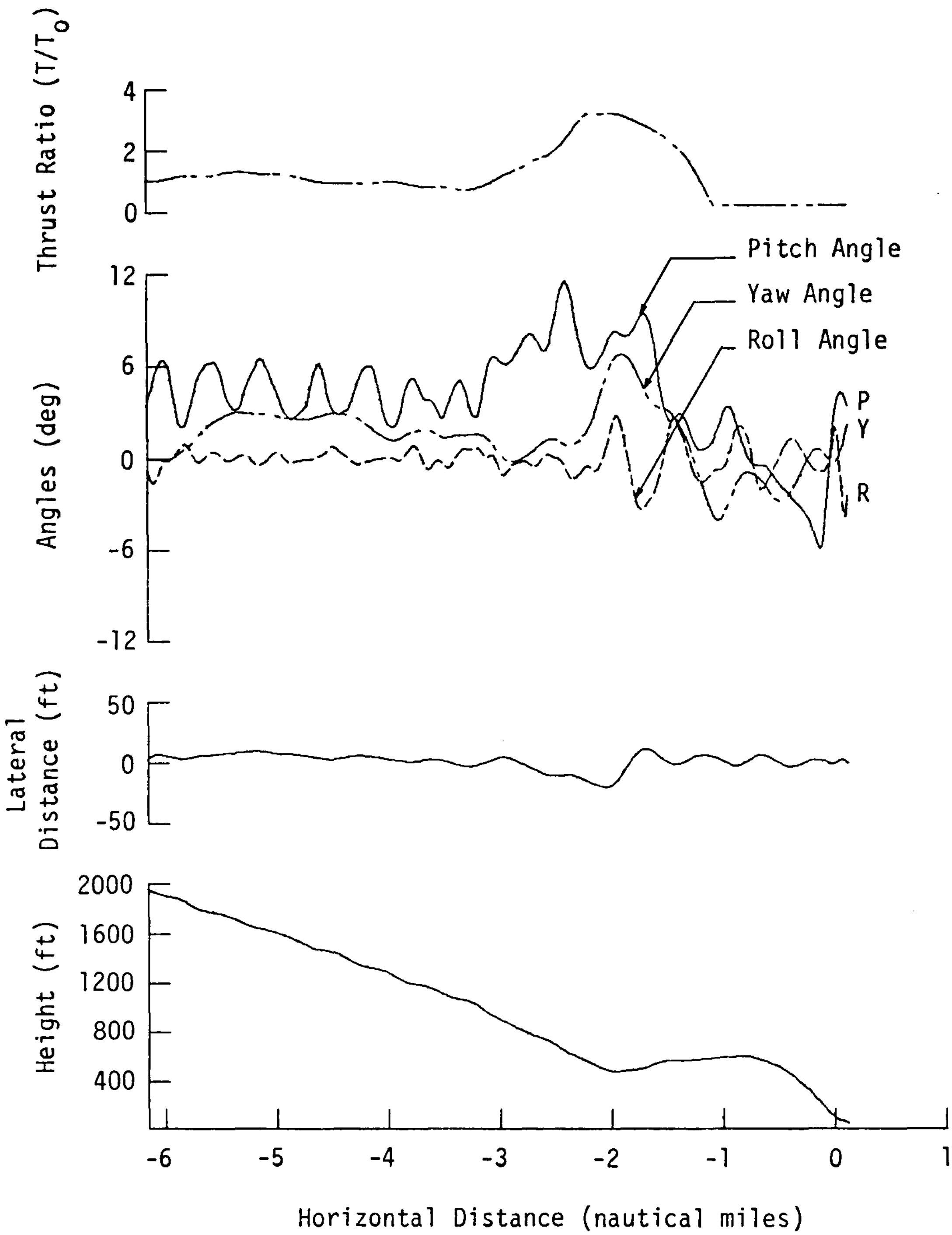

Figure 5.20. Dynamic performance of a B727-200 type aircraft flying along path $\overline{AB}$ with the effects of the wind gradient terms (z_o = 820 ft).

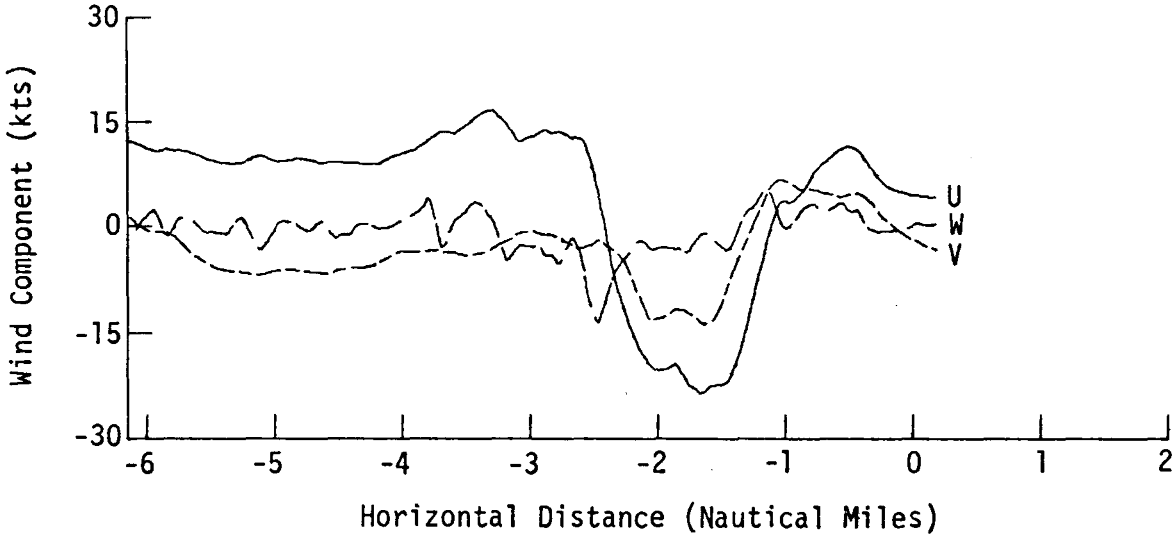

Figure 5.21. Wind speed components encountered by an aircraft flying along path $\overline{AB}$ (z_0 = 820 ft).

of larger than one would induce the higher magnitudes of the wind gradient terms. However, the microburst with the new wind speed components apparently has higher quasi-mean wind speeds than the original one. An effective turbulence model to implement the existing JAWS data set without changing the measured quasi-mean wind speeds is still under development. To provide a simple assessment of this effect, the same flight shown in Figures 5.19 and 5.20 was recalculated multiplying each gradient term by a factor of two. Figure 5.22 shows the results. Comparing the results with those in Figure 5.19, one observes a significant influence of the wind gradients on the aircraft responses. The aircraft trajectory deviates severely from the intended flight path and drastic changes in the vehicle roll, pitch, and yaw angles are induced by the augmented wind gradient terms, especially near the center of the microburst. This observation suggests the importance of the development of a turbulence model to be superimposed on the existing JAWS data.

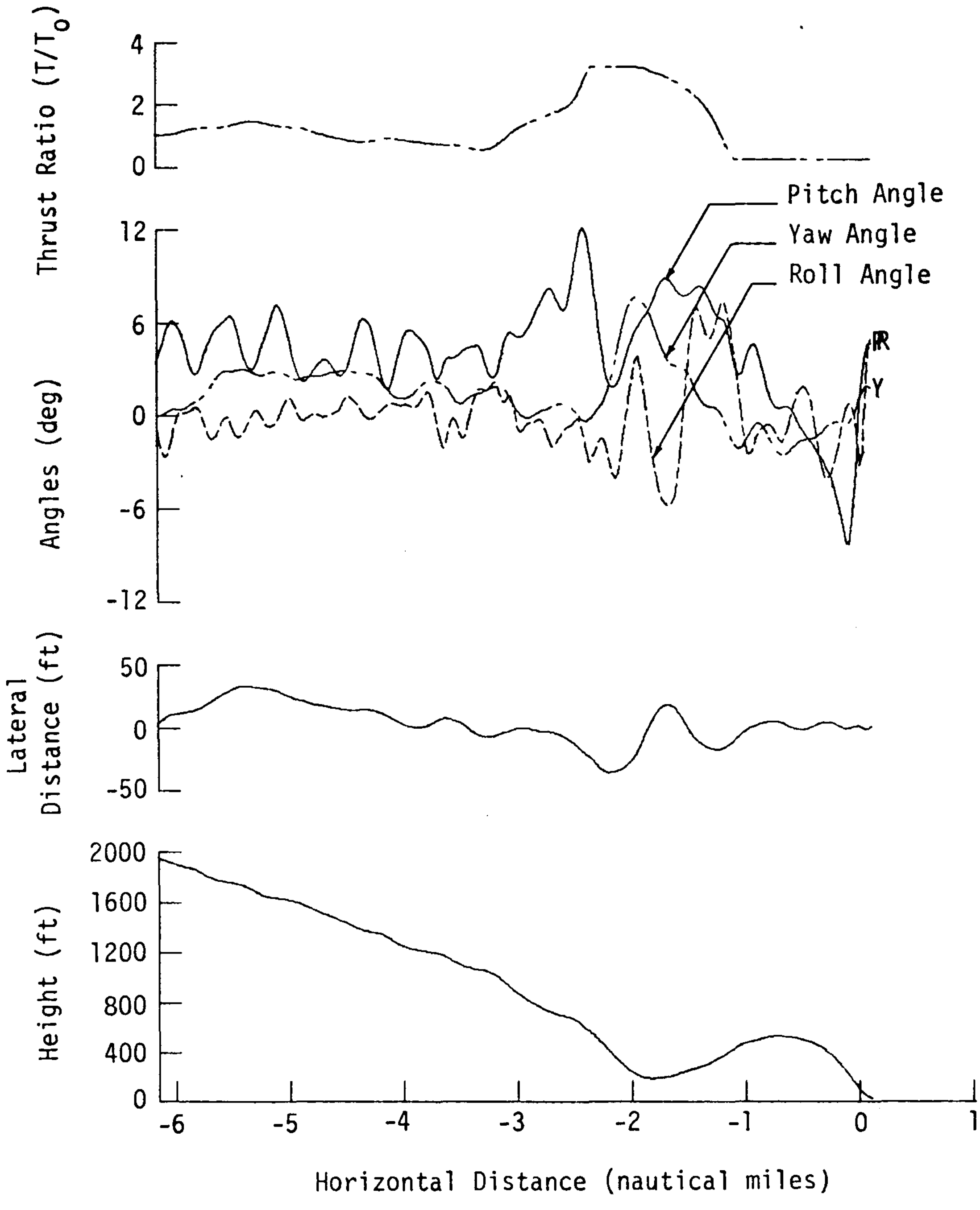

Figure 5.22. Dynamic performance of the B727-200 type aircraft flying along path $\overline{AB}$ with twice the magnitude of JAWS original wind gradient terms (z_0 = 820 ft).

In order to quantify the magnitude of the influence of the wind gradient terms, approaches along several paths emanating radially from the center of a microburst cell (see Figure 5.23) were carried out. All flights enter the microburst cell at 18,000 feet from the center and pass through the center at a height of 984 feet. Each of these flights are simulated without the effects of the wind gradient terms, with their effects and with the effects of twice the magnitude of the wind graident terms.

Standard deviations (SD) of the aircraft responses relative to the trim conditions for each flight path within the microburst cell are shown in Figure 5.24. Figure 5.24 includes the SD's of yaw, pitch, roll, and sideslip angles; angle of attack, thrust ratio, and sinking speed. Also, the standard deviations of the important wind gradient terms, $\partial W_X/\partial X$, $\partial W_X/\partial Z$, $\partial W_Z/\partial X$, and $\partial W_Z/\partial Z$, encountered by the aircraft through the microburst cell are plotted in Figure 5.25.

In general, the wind gradient terms are observed to significantly influence the aircraft responses in: roll and sideslip angles, angle of attack, thrust ratio, and sinking speed. However, the wind gradients only slightly affect the yaw and pitch angles of the aircraft. Figure 5.25c shows that the wind gradient terms have the most serious influence on roll angle. This also shows the importance of the induced rolling moment which is emphasized by Houbolt (1984). Two of the 12 simulations with twice the magnitude of the wind gradient terms crash near the center of microburst because the wind gradients $\partial W_X/\partial X$, $\partial W_X/\partial Z$, and $\partial W_Z/\partial X$ are significantly greater than those of the other flights. For a B727 type aircraft flying through the center of the microburst cell at

(3.08 miles, -11.22 miles)
[(4.95 km, -18.05 km)]

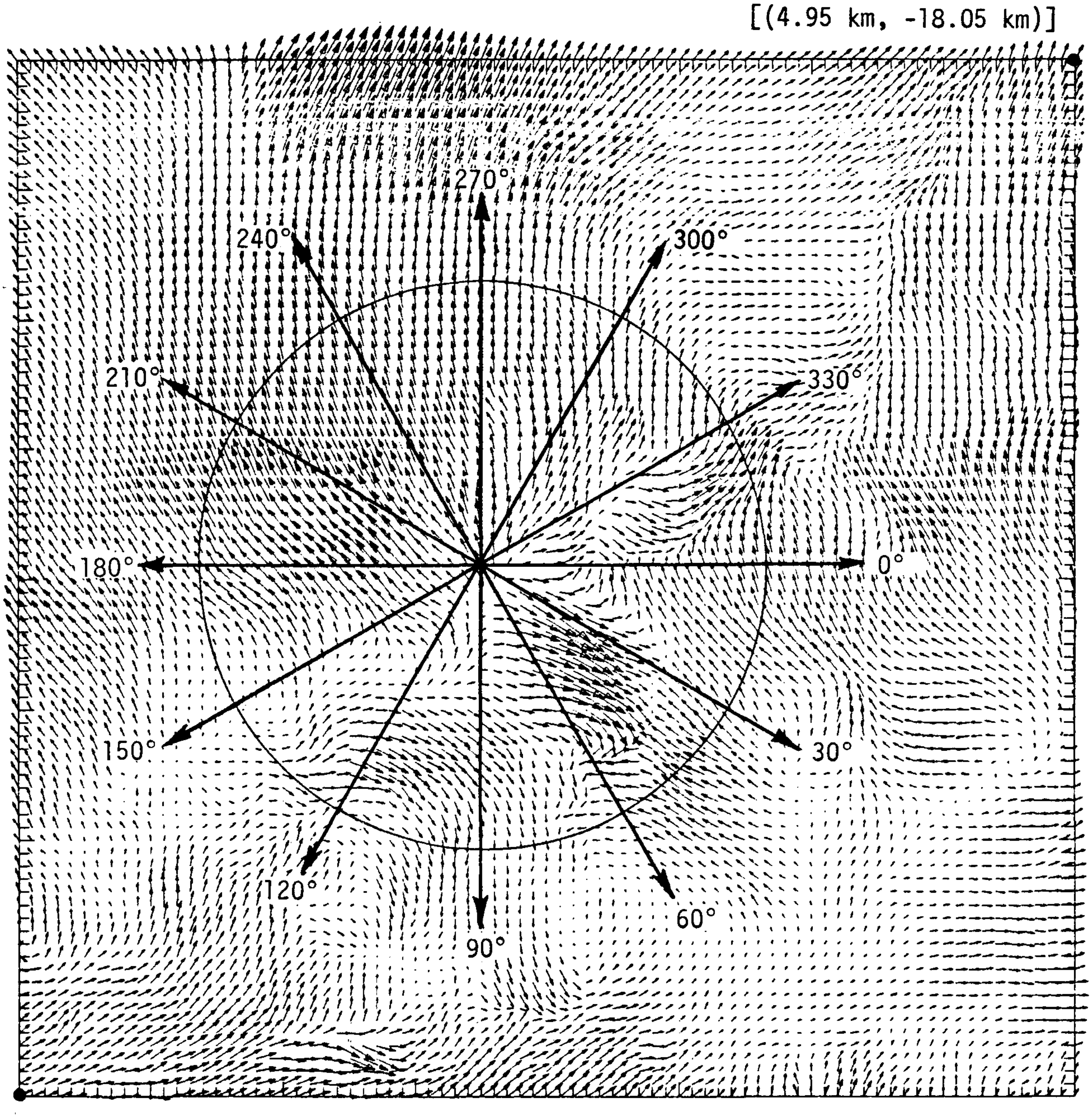

(-4.38 miles, -18.67 miles)
[(-7.05 km, -30.05 km)]

Figure 5.23. Paths chosen for simulation flights through the microburst cell overlaid on horizontal wind speed vectors at the height of 820 ft (second level of August 5, 1982, 1847 MDT microburst).

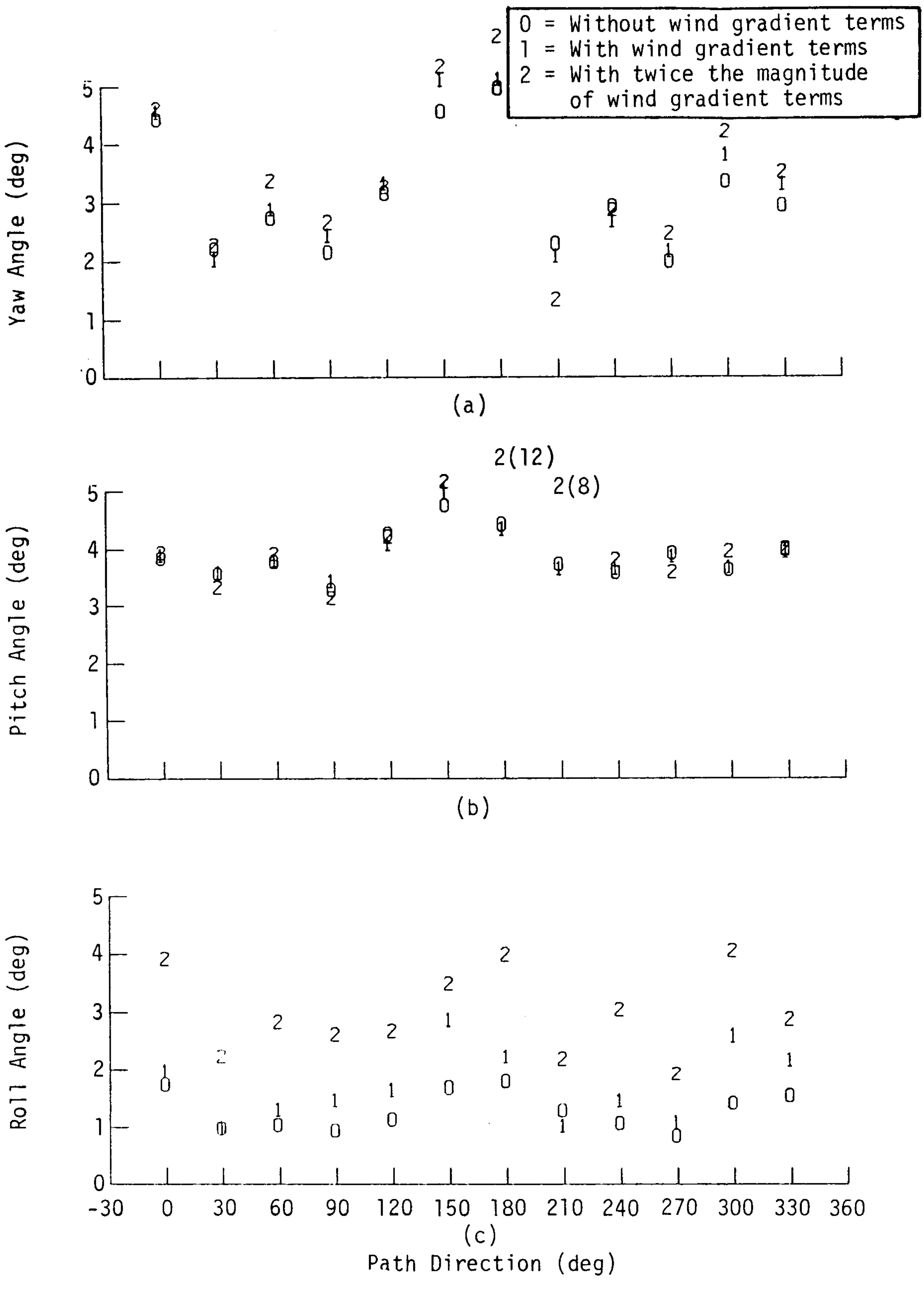

Figure 5.24. Standard deviations from trim conditions of aerodynamic parameters of a B727-200 type airplane for different paths through the microburst cell.

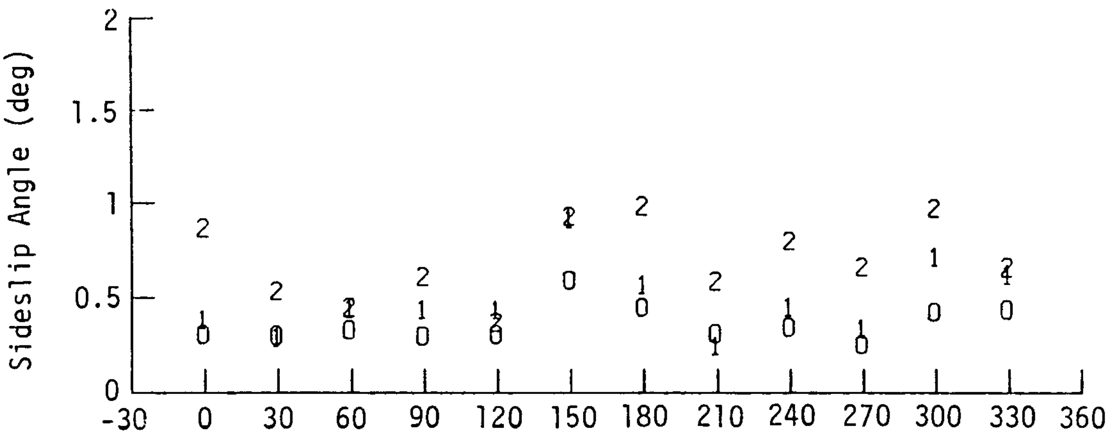

(d)

Path Direction (deg)

2(11 deg)

2(10 deg)

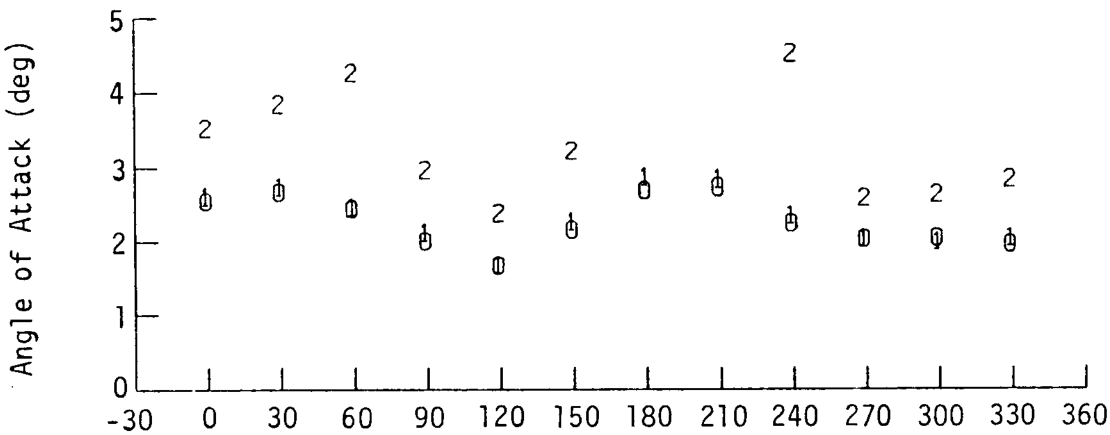

(e)

Path Direction (deg)

Figure 5.24. (continued).

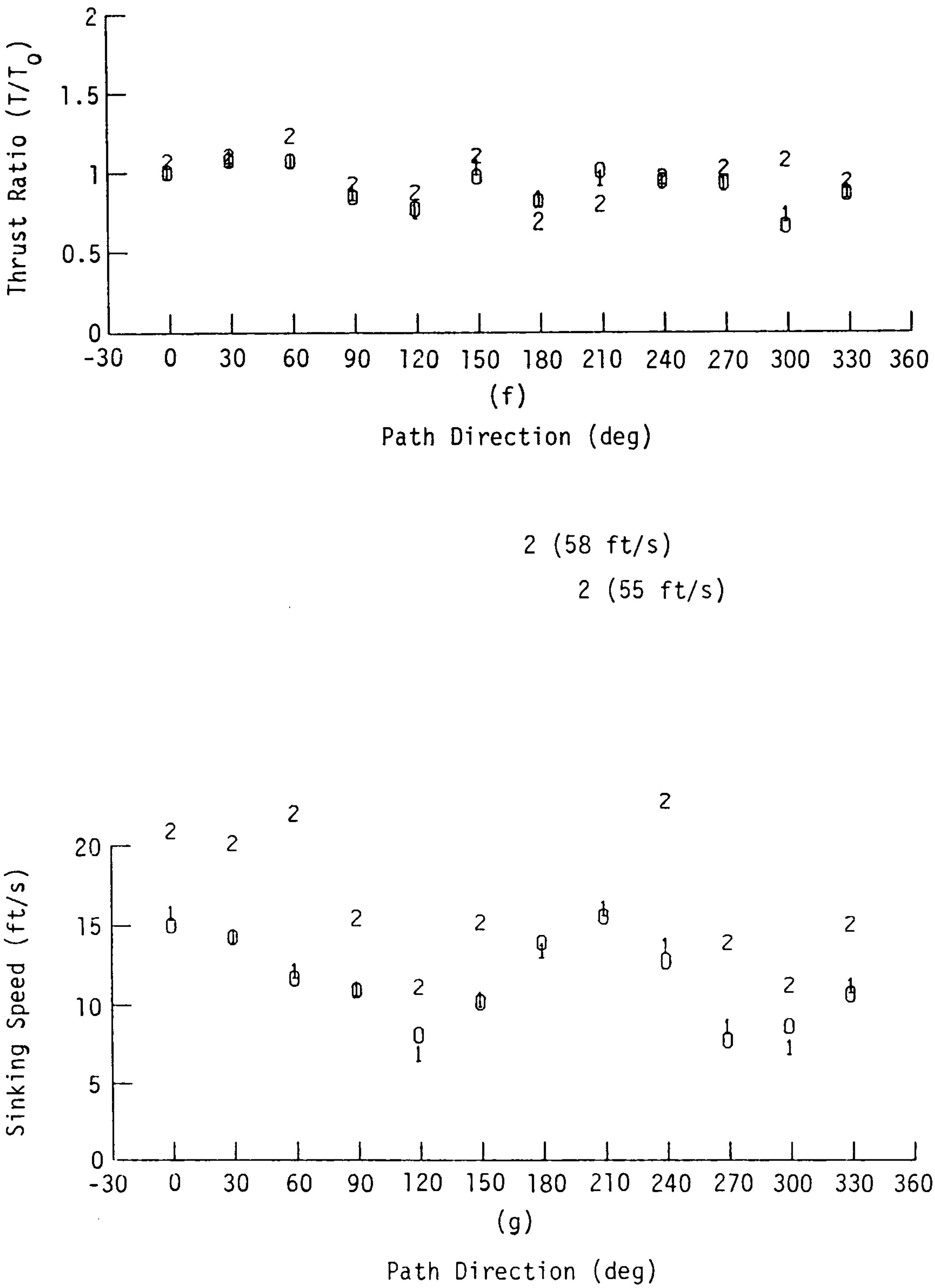

Figure 5.24. (continued).

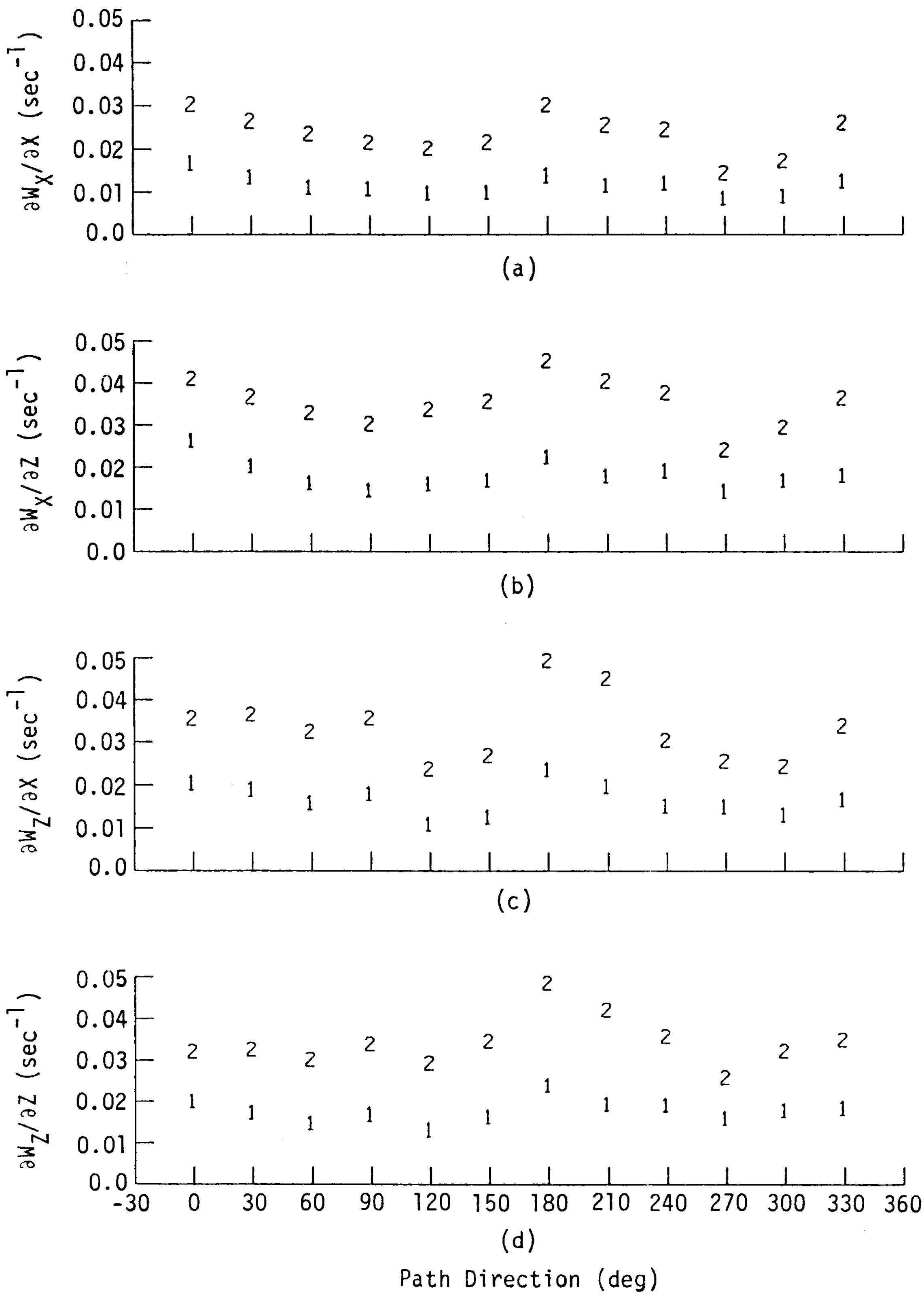

Figure 5.25. Standard deviations from zero wind gradient of four prominant wind gradient terms encountered by a B727-200 airplane flying through the microburst cell.

984 feet, the critical standard deviation of the wind gradient terms is 0.04 s^{-1}. If the airplane flies through the microburst center at a lower height, the critical standard deviation of the wind gradient terms is less than 0.04 s^{-1}. Also, inspection of Figures 5.24 and 5.25 show the changes in aircraft dynamic performance are not linearly proportional to the magnitudes of the wind gradient terms.

3. DIFFERENT TYPES OF AIRCRAFT

The wind shear effects on three different types of aircraft, a three-engine passenger airliner (PA), a twin-engine STOL (STOL), and an executive jet (EJ), are calculated and discussed in this section. The physical parameters of these airplanes are listed in the Appendix. The JAWS August 5, 1847 MDT microburst has been selected as a standard wind field for these different aircraft comparisons.

Figures 5.26 and 5.27 show the trajectories and longitudinal wind components of these different airplanes flying through a microburst center along the intended path $\overline{AB}$ at a height of 820 feet and along the path $\overline{CD}$ at the same height. The maximum deviations of the trajectories along the specific glide slope path $\overline{AB}$ are 350 feet, 200 feet, and 100 feet for the PA, EJ, and STOL type airplanes, respectively. The PA type aircraft deviates from the established path more severely than the others. The STOL type aircraft, the smallest aircraft of the three, maintains the glide slope with little deviation. This is in direct agreement with McCarthy et al. (1979) and Turkel and Frost (1980). They suggest that large commercial transports will experience greater difficulty in flight through wind shear than smaller aircraft due to the

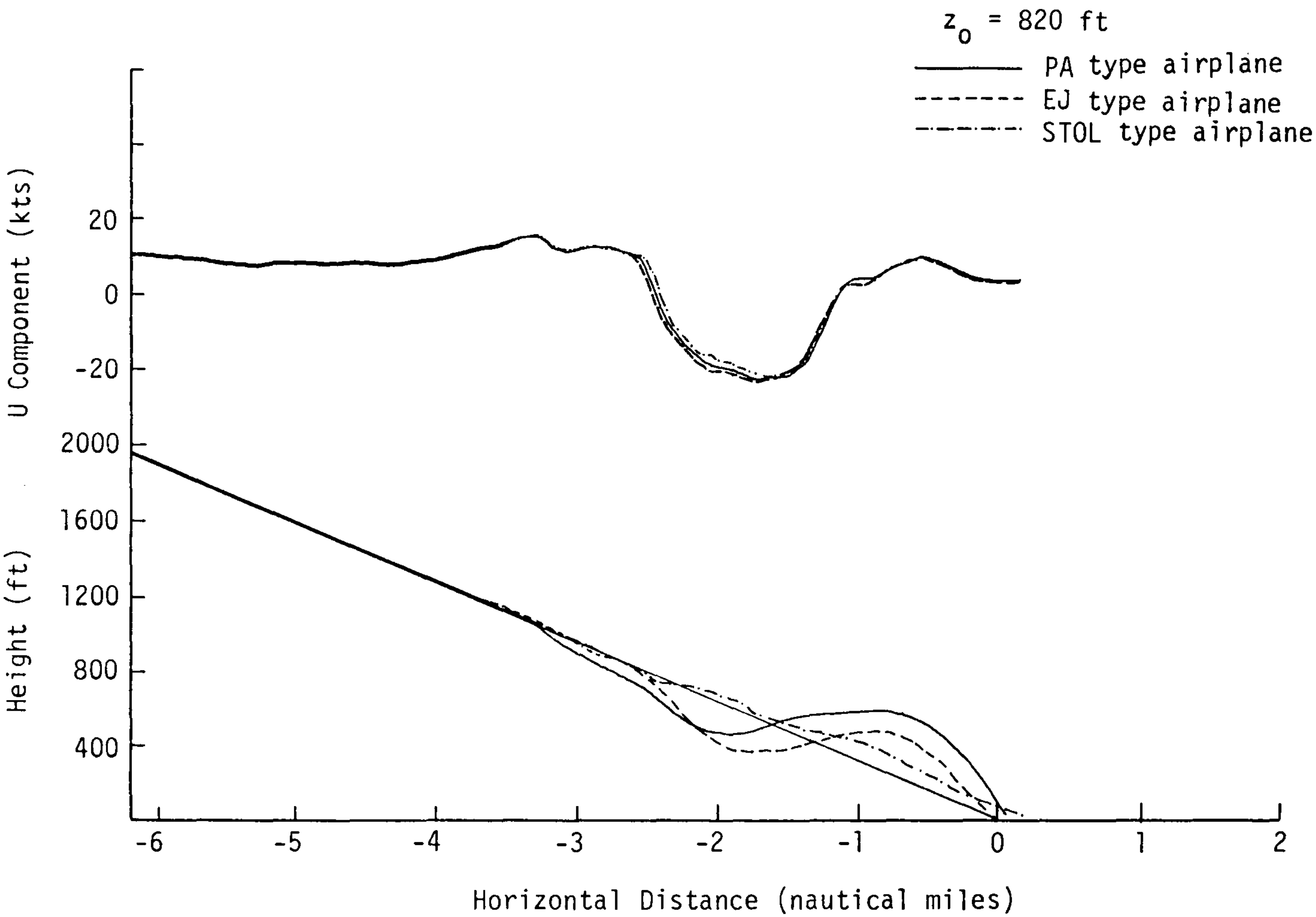

Figure 5.26. Approach flights of the PA, EJ, and STOL type airplanes along path $\overline{AB}$.

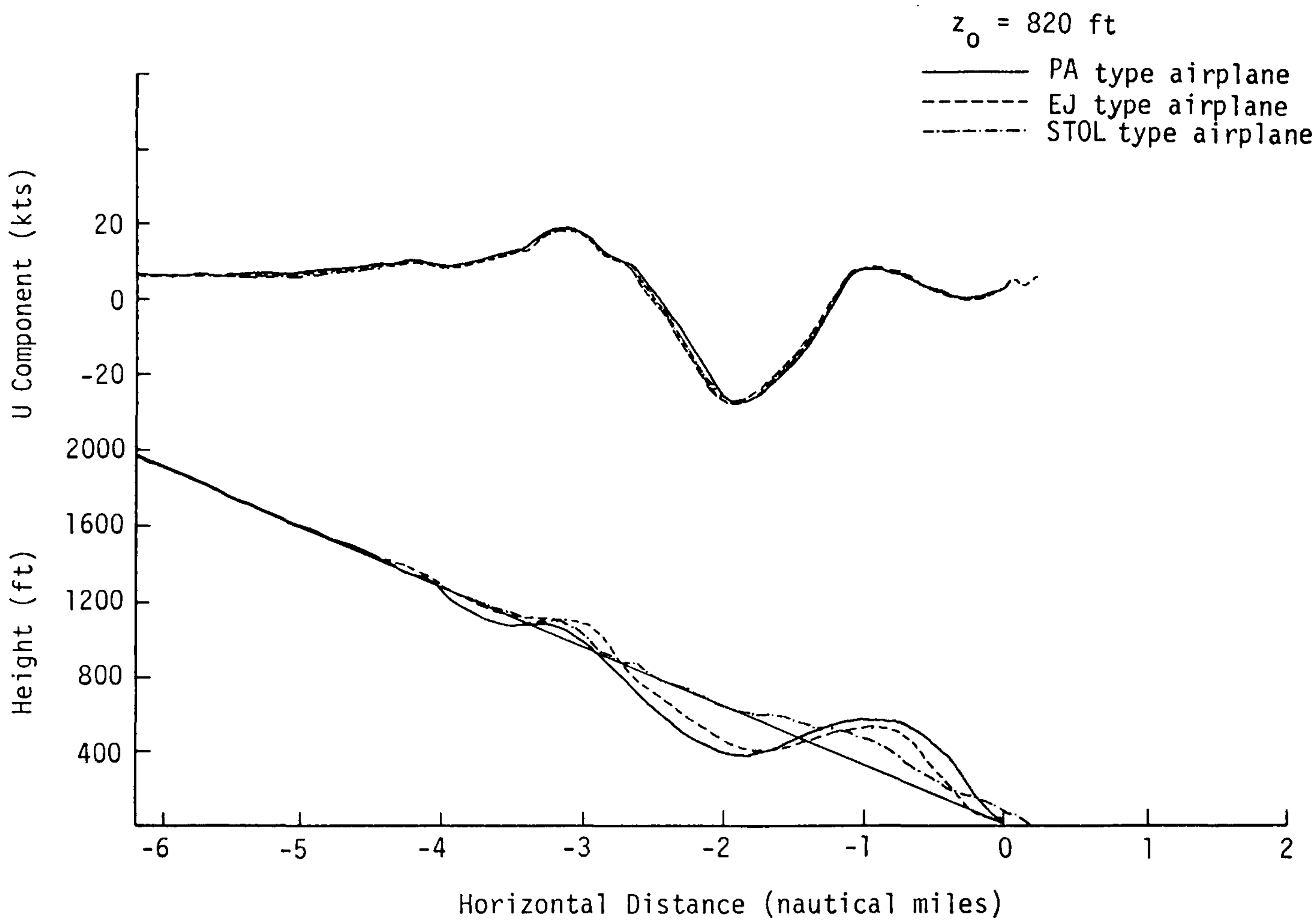

Figure 5.27. Approach flights of the PA, EJ, and STOL type airplanes along path $\overline{CD}$.

effects of higher landing speed and higher lift-to-drag ratio influence on the exponential phugoid damping period, T. T, which is also the time for the oscillation to decay to 1/e of its initial amplitude, is given by $T = (V_0/g)(C_{L_0}/C_{D_0})$ where V_0 is the equilibrium airspeed, g is gravitational acceleration, and C_{L_0} and C_{D_0} are the lift and drag coefficients at zero angle of attack for the particular aircraft.

Table 5.6 shows comparative calculations of the exponential phugoid damping period for the PA, EJ, and STOL type airplanes. Thus, the high approach airspeed and high lift-to-drag ratios of commercial jet aircraft contribute to a large exponential phugoid damping period. This means that the phugoid oscillation of a jet transport does not damp out as quickly as that of a smaller aircraft. Since wind shear tends to drive the oscillation at the phugoid frequency, this adds significance to the results that smaller aircraft have smaller trajectory deviation from the intended flight path than large aircraft upon encountering wind shear.

4. TIME-DEPENDENT MICROBURST

JAWS August 5, 1982, microburst data consists of four serial measurements: 5AU1845, 5AU1847, 5AU1850, and 5AU1852, which are measured at 1845, 1847, 1850, and 1852 Mountain Daylight Time (MDT), respectively. These measurements have been used as time-dependent wind shear data to investigate the influence of storm time variation on the aircraft performance. The technique to interpolate the time-dependent wind shear data has been introduced in Chapter IV, Section 2.

TABLE 5.6. Comparison of Exponential Phugoid Damping Periods (T) of the PA, EJ, and STOL Type Airplanes.

T = time for phugoid oscillation to decay to 1/e of its initial amplitude

$$T = \frac{V_o}{g} \frac{C_{L_o}}{C_{D_o}}$$

where

V_o = approach airspeed

g = gravitational acceleration

C_{L_o} = lift coefficient (zero angle of attack)

C_{D_o} = drag coefficient (zero angle of attack)

	PA	EJ	STOL
V_o (ft/s)	230.0	248.0	118.0
g (ft/s^2)	32.174	32.174	32.174
L/D ratio	9.784	3.691*	3.1
T (sec)	70.0	28.5	11.4

*L/D ratio of EJ type aircraft is adopted from Clark and Kroll (1966).

Figure 5.28 shows the dynamic responses and longitudinal wind components of a B727 type aircraft approaching through each of the four individual time-dependent microburst wind fields. The B727 type aircraft takes about 160 seconds to 180 seconds to make a typical approach flight from a height of 1968 feet. For the same intended flight path, calculations of a B727 type aircraft landing through the time-dependent (TD) microburst are shown in Figure 5.29. The simulation through the TD microburst including 5AU1847, 5AU1850, and 5AU1852 measurements originates at 1847 corresponding to the 5AU1847 data set. The dynamic response and approach trajectory of the B727 type airplane in the TD microburst is essentially a composite of those for four serial measurements. For this specific microburst, there is, however, no significant influence of time variations on the aircraft performance. Measurement of the microburst at shorter time intervals (<2 minutes) would be necessary to study further the influence of time variation on the aircraft responses.

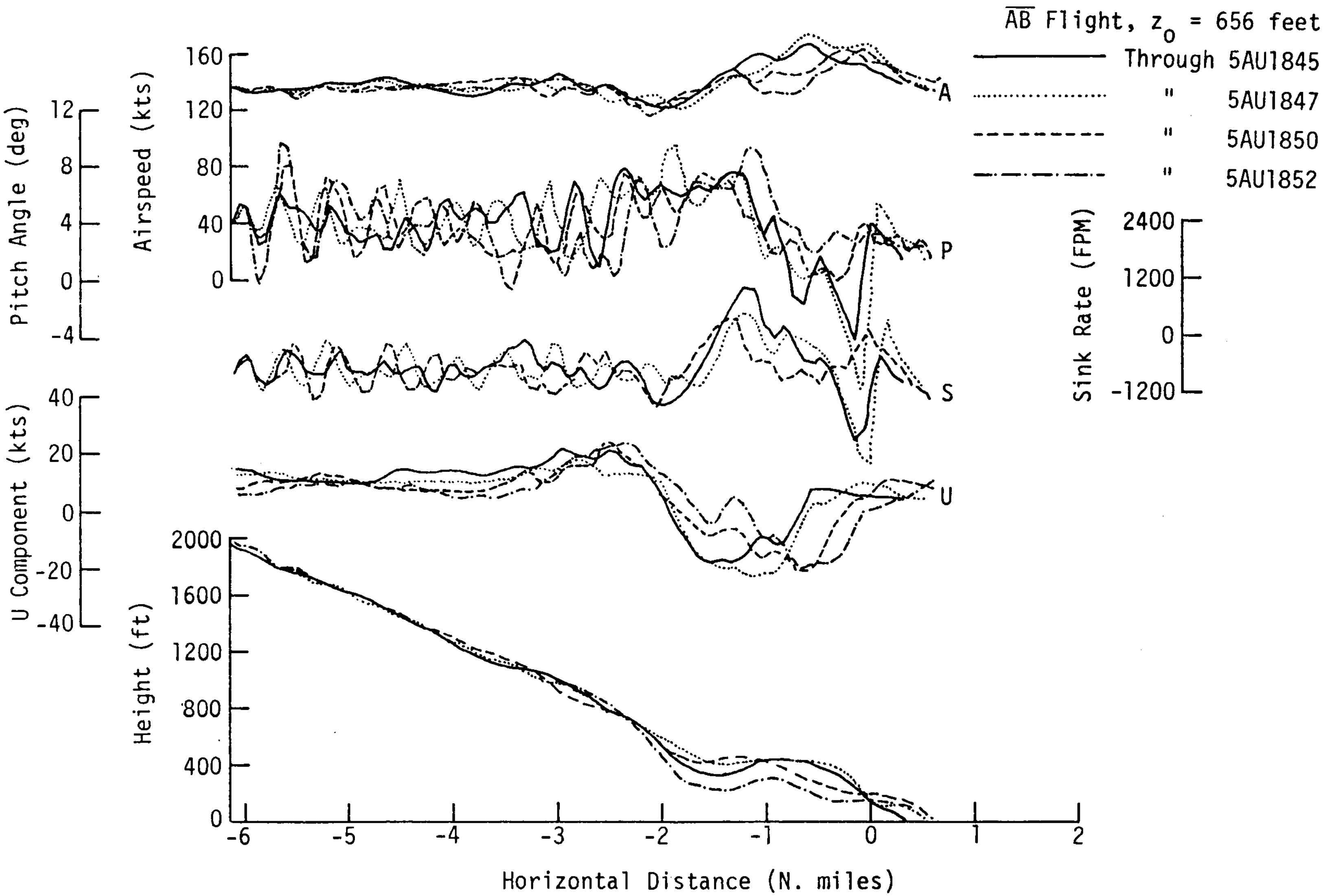

Figure 5.28. Dynamic response and longitudinal wind component of a B727 type aircraft approaching through each of the four wind fields measured at consecutive times.

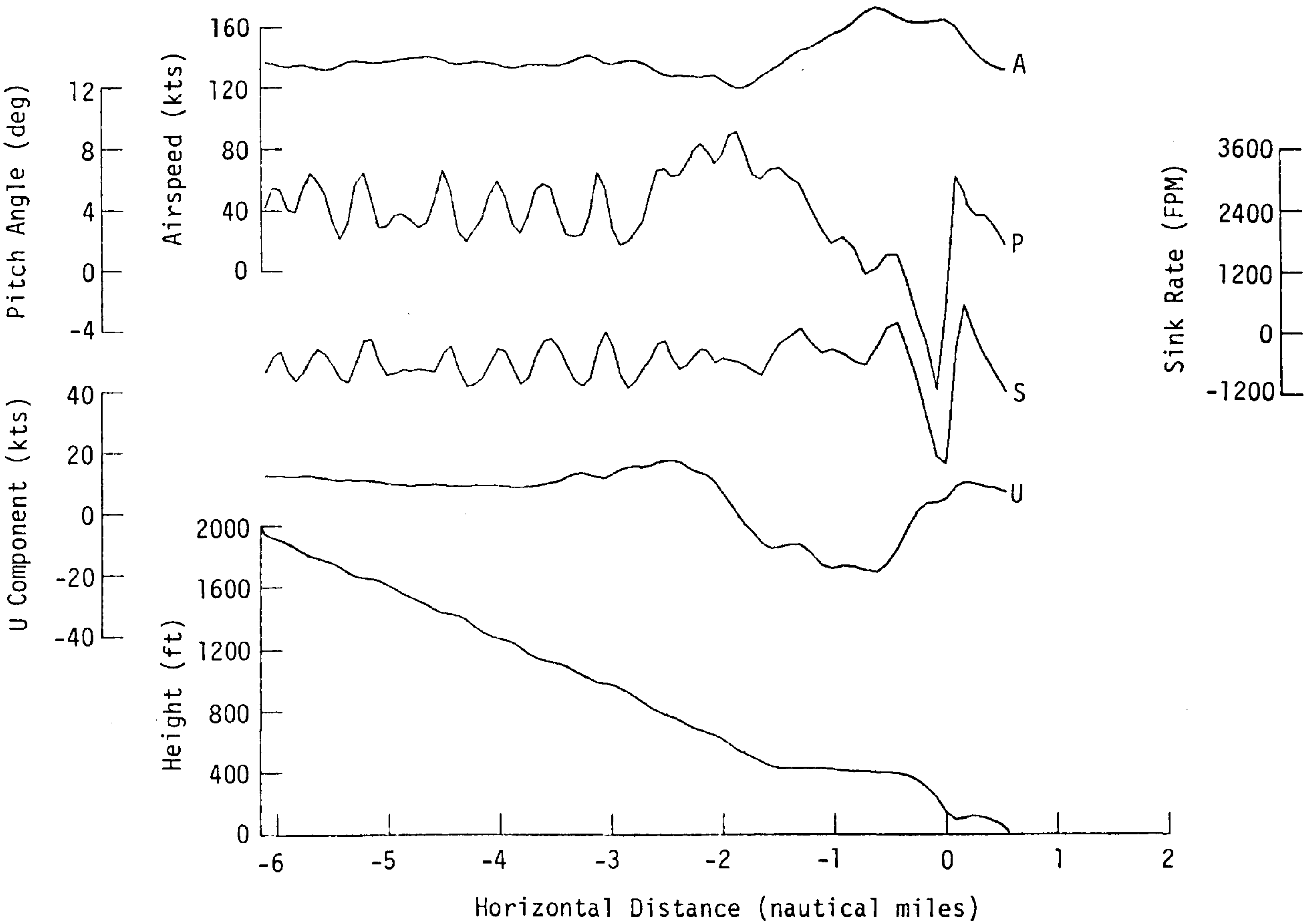

Figure 5.29. Dynamic response and longitudinal wind component of a B727 type aircraft approaching through a microburst interpolated for time ($\overline{AB}$ flight, z_o = 656 ft, originating at 1847 MDT).

CHAPTER VI

CONCLUSIONS

Derivation of the governing equations of aircraft motion in a spatially and temporally varying wind field results in additional terms appearing in the force equations. Moreover, the wind vector and its derivatives implicitly influence the evaluation of the aerodynamic coefficients. Also, the JAWS wind shear data sets provide the first truly four-dimensional wind field of a microburst available for application to flight training and engineering research simulators. The computer simulations, which are developed for the landing and takeoff of a B727-200 type aircraft in this study, are very compatible with those of the NASA/Ames B727 manned simulator.

Computer analyses of aircraft performance during landing and takeoff phases in JAWS three-dimensional wind fields clearly illustrates the hazards in particular regions of the wind field. The classifications of the JAWS data can be used by airline training flight simulator users, as well as research and development simulator engineers, to readily select wind shears of the intensity necessary for their particular project.

Also, the position of a microburst occurrence relative to the runway, as well as the height of an aircraft flying through a microburst center, are very important factors to aviation safety. In the JAWS data used in this study, the critical heights of a B727 type aircraft approaching through the center of microburst with a maximum velocity difference of 45 knots, ranged from 164 feet to 984 feet. In takeoff cases, the critical horizontal distance measured from the liftoff point of a B727 type aircraft to the effective center of the microburst is approximately ±550 feet (a negative sign means that liftoff occurs before encountering the microburst center).

The accuracy and the optimum computational procedure for evaluating the wind speed gradients is investigated. The technique of backward difference saves 20 percent of computation time but it induces over 25 percent difference to the flight conditions at CAT II decision height window. The dimensional parameter, $N_S = (W_Z/Z)(\partial W_X/\partial X)$, shows a good correlation with the trajectory deviation of an aircraft at the CAT II decision height window. The trajectory deviation of a B727 type aircraft has a non-linear variation with the ratio of the time period in which the aircraft experiences a value of $N_S \geq 0.00005\ s^{-2}$ to the total time during its approach.

Wind gradient terms of the JAWS data, in which the maximum absolute value of the wind gradient terms is $0.03\ s^{-1}$, have slight influence on the dynamic response of an aircraft encountering the wind shear data. The magnitudes of the wind gradient terms can be much stronger than this value primarily due to local atmospheric turbulence and/or due to higher maximum wind velocity differences of the microburst. Analysis of an aircraft encountering both the actual measured JAWS wind gradient values and twice the magnitudes of the wind gradient terms shows that the higher the magnitudes of wind gradient terms, the more influence they have on aircraft performance, especially on the sideslip angle, angle of attack, and roll moment. Therefore, adding to the existing JAWS wind shear data a meaningful turbulence model based on further analyses of the JAWS data, particularly the second moment of the radar return signal, is highly recommended. Moreover, it is recommended that existing flight simulator programs be updated to incorporate the additional wind shear terms into the equations of vehicle motion.

A significant conclusion can be drawn with respect to wind shear effects on different types of airplanes. Since the phugoid oscillation of a jet transport does not damp out as quickly as that of a small aircraft, large jet aircraft experience greater difficulty in flight through a wind shear field than smaller aircraft. In order to study the influence on aircraft performance of time variation of wind shear in the JAWS data sets, serial measurements with shorter time intervals should be carried out.

BIBLIOGRAPHY

BIBLIOGRAPHY

AGARD Conference Proceedings No. 140 on Flight in Turbulence (1973). AGARD-CP-140, 378 pp. Technical Editing and Reproduction Ltd., Hartford House, 7-9 Charlotte Street, London, England W1P 1HD.

Aviation Week and Space Technology (1984). February 27 and August 27 issues. McGraw-Hill, Inc., 1221 Avenue of the Americas, New York, New York 10020.

Aviation Week and Space Technology (1983). March 7 and December 5 issues. McGraw-Hill, Inc., 1221 Avenue of the Americas, New York, New York 10020.

Babister, A. W. (1980). Aircraft Dynamic Stability and Response. New York: Pergamon Press.

Bray, R. S. (1984). "Implementation of Wind-Field Models in a 727 Training Simulator," Presentation at NASA Langley Wind Shear/ Turbulence Workshop, Hampton, Virginia, May 30 - June 1.

Camp, D., W. Campbell, W. Frost, H. Murrow, and W. Painter (1984). "NASA's B-57B Gust Gradient Program," Journal of Aircraft, 21(3): 175-182, March.

Campbell, W. C. (1984). "A Spatial Model of Wind Shear and Turbulence for Flight Simulation," NASA TP 2313, May.

Clark, D. C., and J. Kroll (1966). "General Purpose Airborne Simulator-Conceptual Design Report," NASA CR 544, August.

Etkin, B. (1972). Dynamics of Atmospheric Flight. New York: John Wiley and Sons, Inc.

Foy, W. H. (1979). "Airborne Aids for Coping with Low-Level Wind Shear," FAA Report No. FAA-RD-79-117, U.S. Dept. of Transportation, Washington, D.C.

Frost, W. (1984). "Turbulence Models," Presentation at the NASA Langley Wind Shear/Turbulence Workshop, Hampton, Virginia, May 30 - June 1.

Frost, W., H. P. Chang, K. L. Elmore, and J. McCarthy (1985). "Microburst Wind Shear Models from JAWS," Final report under NCAR Subcontract S3011, January.

Frost, W., and R. L. Bowles (1984). "Wind Shear Terms in the Equations of Aircraft Motion," Journal of Aircraft, 21(11):866-872, November.

Frost, W., H. P. Chang, J. McCarthy, and K. L. Elmore (1983). "Aircraft Performance in a JAWS Microburst," Preprints: 21st Conference on Radar Meteorology, September 19-23, Edmonton, Alberta, Canada. Boston: American Meteorological Society, pp. 630-637.

Frost, W., D. W. Camp, and S. T. Wang (1979). "Thunderstorm Wind Shear Modeling for Aircraft Hazard Definition," Paper No. 23, Proceedings: World Meteorological Organization Technical Conference on Aviation Meteorology, November 5-9, Geneva, Switzerland.

Fujita, T. (1982). "The JAWS Project: Operations Summary 1982," University of Chicago.

Goff, C. (1980). "Measuring Weather for Aviation Safety in the 1980's," Proceedings: Fourth Annual Workshop on Meteorology and Environmental Inputs to Aviation Systems, NASA CP 2139, FAA-RD-80-67.

Houbolt, J. (1984). "Turbulence Modeling," Presentation at the NASA Langley Wind Shear/Turbulence Workshop, Hampton, Virginia, May 30 - June 1.

Houbolt, J., R. Steiner, and K. G. Pratt (1964). "Dynamic Response of Airplanes to Atmospheric Turbulence Including Flight Data on Input and Response," NASA TR R-199.

Houghton, E. L., and A. E. Brock (1972). Aerodynamics for Engineering Students. New York: St. Martin's Press.

Johnson, W. A., and R. H. Hoh (1972). "Determination of ILS CAT II Decision Height Window Requirements," NASA CR 2024.

Karamcheti, K. (1966). Principles of Ideal-Fluid Aerodynamics. New York: John Wiley and Sons, Inc.

McCarthy, J. (1983). "What We Have Learned from the Flight of Pan Am Flight 759," UCAR Corporate Meeting Presentation, September 15-16.

McCarthy, J., E. F. Blick, and R. R. Bensch (1979). "Jet Transport Performance in Thunderstorm Wind Shear Conditions," NASA CR 3207, December.

National Research Council (1983). "Low-Altitude Wind Shear and Its Hazard to Aviation," National Academy Press, Washington, D.C.

Peloubet, R. P., and R. L. Haller (1966). "Application of a Power Spectral Gust Design Procedure to Bomber Aircraft," USAF Wright-Patterson Technical Report AFFDL-TR-66-35, June.

Perkins, C. D., and R. E. Hage (1963). Airplane Performance Stability and Control. New York: John Wiley and Sons, Inc.

Reeves, P. M., R. G. Joppa, and V. M. Ganzer (1976). "A Non-Gaussian Model of Continuous Atmospheric Turbulence for Use in Aircraft Design," NASA CR 2639.

Reeves, P. M., G. S. Campbell, V. M. Ganzer, and R. G. Joppa (1974). "Development and Application of a Non-Gaussian Atmospheric Turbulence Model for Use in Flight Simulations," NASA CR 2451, September.

Ringnes, E., and W. Frost (1984). "Analyses of Turbulence Spanwise Effects on Aircraft Performance," Final report for NASA Marshall Space Flight Center under Contract NAS8-35186, December.

Roskam, J. (1973). "Fluid Dynamics of Rigid and Elastic Airplanes, Part 1." Printed by the author: Professor of Aerospace Engineering, The University of Kansas, Lawrence, Kansas.

Turkel, B. S., and W. Frost (1980). "Pilot-Aircraft System Response to Wind Shear," NASA CR 3342, November.

Turkel, B. S., P. A. Kessel, and W. Frost (1981). "Feasibility Study of a Procedure to Detect and Warn of Low-Level Wind Shear," NASA CR 3480, November.

Wang, S. T., and W. Frost (1980). "Atmospheric Turbulence Simulation Techniques with Application to Flight Analysis," NASA CR 3309.

APPENDIX

APPENDIX

CHARACTERISTICS OF AIRCRAFT USED IN NUMERICAL FLIGHT SIMULATIONS

The aircraft characteristics used in this simulation study are for those of a three-engine passenger airliner (PA), an executive jet (EJ), and a twin-engine STOL (STOL) type aircraft. The initial conditions and aircraft physical parameters for a landing simulation are given as follows:

	PA	EJ	STOL
Initial airspeed, V_0 (ft/s)	230	248	118
Intended approach path angle, γ (deg)	3	2.96	3
Aircraft weight, W (lbs)	141,000	37,400	11,000
Moment of inertia, I_X (slug·ft^2)	1.0×10^6	9.38×10^4	1.59×10^4
Moment of inertia, I_Y (slug·ft^2)	4.5×10^6	15.38×10^4	2.35×10^4
Moment of inertia, I_Z (slug·ft^2)	4.8×10^6	23.5×10^4	3.60×10^4
Moment of arm of thrust, L_T(ft)	0	1.98	0
Mean aerodynamic chord, $\bar{C}$ (ft)	15	10.93	6.5
Wing area, S (ft^2)	1560	542.5	420
Wing span, b (ft)	108	53.5	65

The initial conditions of the PA type aircraft in a takeoff simulation are given as follows:

Aircraft weight, W (lbs)	169,000
Moment of inertia, I_X (slug·ft^2)	0.92×10^6
Moment of inertia, I_Y (slug·ft^2)	4.75×10^6
Moment of inertia, I_Z (slug·ft^2)	5.40×10^6
Moment of inertia, I_{ZX} (slug·ft^2)	2.02×10^5

The expressions for the aerodynamic coefficients and stability derivatives of the PA type airplane are adopted from an engineering users manual.

The expressions for the aerodynamic coefficents of the STOL type aircraft are given in Reeves et al. (1974):

$$C_D = C_{D_o} + C_{D\alpha} \cdot \alpha$$

$$C_Y = C_{Y\beta} \cdot \beta + \frac{b}{2V} (C_{Y_r} r + C_{Y_P} P) + C_{Y_{\delta a}} \delta a + C_{Y_{\delta r}} \delta r$$

$$C_L = C_{L_o} + C_{L_\alpha} \alpha + \frac{\bar{C}}{2V} (C_{L_{\dot{\alpha}}} \dot{\alpha} + C_{L_q} q) + C_{L_{\delta e}} \delta e$$

$$C_\ell = C_{\ell_\beta} \cdot \beta + \frac{b}{2V} (C_{\ell_r} r + C_{\ell_P} P) + C_{\ell_{\delta a}} \delta a + C_{\ell_{\delta r}} \delta r$$

$$C_m = C_{m_\alpha} \cdot \alpha + \frac{\bar{C}}{2V} (C_{m_{\dot{\alpha}}} \dot{\alpha} + C_{m_q} q) + C_{m_{\delta e}} \delta e$$

$$C_n = C_{n_\beta} \cdot \beta + \frac{b}{2V} (C_{n_r} r + C_{n_P} P) + C_{n_{\delta a}} \delta a + C_{n_{\delta r}} \delta r$$

For the executive jet type aircraft, the drag coefficients are interpolated from experimental data curves. The other aerodynamic coefficients are expressed as follows:

$$C_Y = C_{Y_\beta} \cdot \beta + C_{Y_{\delta r}} \delta r + C_L \sin \phi$$

$$C_L = C_{L_o} + C_{L_\alpha}\alpha + C_{L_{\delta e}}\delta e + C_{L_{i_T}} i_T$$

$$C_\ell = C_{\ell_\beta}\cdot\beta + \frac{b}{2V}\left(C_{\ell_r} r + C_{\ell_P} P\right) + C_{\ell_{\delta a}}\delta a + C_{\ell_{\delta r}}\delta r$$

$$C_m = C_{m_o} + C_{m_\alpha}\cdot\alpha + \frac{\bar{C}}{2V}\left(C_{m_{\dot\alpha}}\dot\alpha + C_{m_q} q\right) + C_{m_{\delta e}}\delta e$$

$$+ C_{m_{i_T}} i_T + C_{m_{GEAR}} - \left(\frac{THRUST}{\bar{q}s}\right)\frac{L_T}{\bar{C}}$$

$$C_n = C_{n_\beta}\cdot\beta + \frac{b}{2V}\left(C_{n_r} r + C_{n_P} P\right) + C_{n_{\delta a}}\delta a + C_{n_{\delta r}}\delta r$$

Stability derivatives of the STOL and EJ type airplanes are obtained from the engineering users manuals.

VITA

Ho-Pen Chang was born in Taichung, Taiwan, Republic of China, on July 5, 1953. He attended elementary schools in that city. He finished high school education in Taipei. In June 1977 he graduated from the National Cheng Kung University, Tainan, Taiwan, where he received a Bachelor of Science degree in Aeronautical Engineering.

After a two-year tour of duty with the China Army, he was employed as a teaching assistant at the National Cheng Kung University in the fall of 1979. He entered the Graduate School at The University of Tennessee Space Institute in September 1980 as a graduate research assistant for the Atmospheric Science Division. He received a Master of Science degree with a major in Aerospace Engineering in June 1982. During the summer of 1983 he married Shi-Min Sau. He received the Doctor of Philosophy degree in Aerospace Engineering in June 1985.

Mr. Chang is a member of AIAA and ASME. He will be employed by FWG Associates, Inc., Tullahoma, after graduation.